Fundamentals of reservoir surface energy as related to surface properties, wettability, capillary action, and oil recovery from fractured reservoirs by spontaneous imbibition

DE-FC26-03NT15408

Quarterly Report
04/01/2005 – 06/30/2005

Norman R. Morrow, Principal Investigator
Herbert Fischer
Yu Li
Geoffrey Mason
Douglas Ruth
Siddhartha Seth
Peigui Yin
Shaochang Wo

August 2005

Submitted by:
Chemical & Petroleum Engineering
University of Wyoming
Dept. 3295, 1000 E. University Ave
Laramie, WY 82071

Disclaimer

ABSTRACT

The objective of this project is to increase oil recovery from fractured reservoirs through improved fundamental understanding of the process of spontaneous imbibition by which oil is displaced from the rock matrix into the fractures. Spontaneous imbibition is fundamentally dependent on the reservoir surface free energy but this has never been investigated for rocks. In this project, the surface free energy of rocks will be determined by using liquids that can be solidified within the rock pore space at selected saturations. Thin sections of the rock then provide a two-dimensional view of the rock minerals and the occupant phases. Saturations and oil/rock, water/rock, and oil/water surface areas will be determined by advanced petrographic analysis and the surface free energy which drives spontaneous imbibition will be determined as a function of increase in wetting phase saturation. The inherent loss in surface free energy resulting from capillary instabilities at the microscopic (pore level) scale will be distinguished from the decrease in surface free energy that drives spontaneous imbibition.

A mathematical network/numerical model will be developed and tested against experimental results of recovery versus time over broad variation of key factors such as rock properties, fluid phase viscosities, sample size, shape and boundary conditions. Two fundamentally important, but not previously considered, parameters of spontaneous imbibition, the capillary pressure acting to oppose production of oil at the outflow face and the pressure in the nonwetting phase at the no-flow boundary versus time, will also be measured and modeled. Simulation and network models will also be tested against special case solutions provided by analytic models.

In the second stage of the project, application of the fundamental concepts developed in the first stage of the project will be demonstrated. The fundamental ideas, measurements, and analytic/numerical modeling will be applied to mixed-wet rocks. Imbibition measurements will include novel sensitive pressure measurements designed to elucidate the basic mechanisms that determine induction time and drive the very slow rate of spontaneous imbibition commonly observed for mixed-wet rocks. In further demonstration of concepts, three approaches to improved oil recovery from fractured reservoirs will be tested; use of surfactants to promote imbibition in oil wet rocks by wettability alteration: manipulation of injection brine composition: reduction of the capillary back pressure which opposes production of oil at the fracture face.

TABLE OF CONTENTS

INTRODUCTION

Objectives

The long-range objective of this project is to improve oil recovery from fractured reservoirs through improved fundamental understanding of the process of spontaneous imbibition by which oil is displaced from the rock matrix into the fractures. Spontaneous imbibition is fundamentally dependent on the surface energy. An initial objective is to determine the surface energy and relate the dissipation of surface energy to the mechanism of spontaneous imbibition. A parallel objective is to model the mechanism of spontaneous imbibition by a combination of network analysis and numerical modeling. Also fundamentally important, but not previously considered, parameters of spontaneous imbibition, the capillary pressure acting to oppose production of oil at the outflow face and the pressure in the nonwetting phase at the no-flow boundary (in effect within oil in the non-invaded zone of the rock matrix) versus time, will also be measured and compared with values predicted by the mathematical model. The next objective is to measure surface energy and related spontaneous imbibition phenomena for mixed-wettability rocks prepared by adsorption from crude oil. The dissipation of surface free energy must then be related to oil production at mixed-wet conditions. The final objective is to apply the results of the project to improved oil recovery from fractured reservoirs in three ways: reduction of the capillary force that opposes oil production at the fracture face; change in wettability towards increased water wetness; identification of conditions where choice of invading brine composition can give improved recovery.

TASKS

Budget period 1, July 1, 2003 through June 30, 2005 – Ideas and Concept development: Fundamentals of Spontaneous Imbibition

Task 1. *Work of displacement and surface free energy.* Obtain complementary sets of capillary pressure drainage and imbibition data and data on changes in rock/brine, rock/oil, and oil/brine interfacial areas with change in saturation for drainage and imbibition for at least two rock types (sandstone and carbonate). Determine free-energy/work-of-displacement efficiency parameters for drainage and imbibition for at least two rock types so that changes in rock/wetting phase/nonwetting phase surface areas can be closely estimated from capillary pressure measurements.

Task 2. *Imbibition in simple laboratory and mathematical network models.* Study imbibition in at least three simple tube networks that can be modeled analytically to establish and/or confirm fundamental aspects of the pore scale mechanism of dynamic spontaneous imbibition with special emphasis on determining how spontaneous imbibition is initiated and the key factors in how the saturation profile develops with time. Incorporate rules developed from laboratory measurements on relatively simple networks into the design of a computational network model. Use the network model to obtain an account of the mechanism by which imbibition is initiated, the saturation profile is developed, and the rate of spontaneous imbibition in terms of the dissipation of surface free energy that accompanies change in saturation.

Task 3. *Novel observations on fluid pressures during imbibition and the mechanism of non-wetting phase production at the imbibition face.* Make novel observations on the imbibition mechanism including details of the mechanism of oil production at the outflow rock face and the change in the nonwetting phase pressure at the no-flow boundary of the core during the course of spontaneous imbibition for at least 16 distinct combinations of rock/ fluid properties.

Task 4. *Network/numerical model and new imbibition data.* Develop a numerical simulator specifically designed for spontaneous imbibition. Incorporate the network model to obtain a network/numerical model that includes matching the measured pressure in the nonwetting phase at the no-flow boundary, and the pressure that opposes production of oil at the open rock face. Imbibition data will be obtained for at least 10 rocks with over six-fold variation in permeability, and at least 6 orders of magnitude variation in viscosity ratio, and at least 10 variations in sample size, shape, and boundary conditions.

Task 5. *Comparison with similarity solutions.* Compare results given by simulation with special case analytic results given by similarity solutions for spontaneous imbibition for at least five distinct cases of rock and fluid properties.

Budget Period 2, July 1, 2005 through June 30, 2008 - Demonstration of concept: Application to mixed wettability rocks and improved oil recovery from fractures reservoirs.

Task 6. *Rock preparation and Work of displacement and surface areas*
Obtain a range of rock types and identify and obtain crude oils that induce stable mixed wettability. Prepare at least 25 rocks with mixed wettability through crude oil/brine/rock interactions.
Determine work of displacement for drainage and imbibition and measure the variation in rock/brine, rock oil, and oil/brine interfacial areas during the course of drainage and imbibition for at least two examples of mixed wettability.

Task 7. *Novel imbibition measurements on mixed-wet rock and network models.* Obtain, for at least six mixed-wet rocks, spontaneous imbibition data that includes measurements of the nonwetting phase pressure at the no-flow boundary, observations on the capillary pressure that resists production at the open rock face.

Task 8. *Application of network/numerical model to mixed wet rocks.* Use network models to relate dissipation of surface energy to rate of spontaneous imbibition and to account for the frequently observed induction time prior to the onset of spontaneous imbibition into mixed wettability rocks.

Task 9. *Increased oil recovery by spontaneous imbibition.* The mechanism of increased recovery from mixed wet rocks by use of surfactants that promote spontaneous imbibition by favorable wettability alteration will be investigated for at least four distinct examples of crude oil/brine/rock/surfactant combinations.
The mechanism of increased recovery by manipulation of brine composition will be investigated for at least four crude oil/brine/rock combinations.

Addition of very low concentration surfactants to the imbibing aqueous phase will be explored as a means of increasing the rate of oil recovery by reducing the capillary forces which resist production of oil at the fracture face. At least twelve combinations of rock and fluid properties including both very strongly wetted and mixed wet rocks will be tested.

PROGRESS BY TASK - BUDGET PERIOD 1

Task 1. *Work of displacement and surface free energy.*

(Siddhartha Seth and Norman Morrow - unpublished manuscript)

Introduction

Capillary pressure curves, when observed in microscopic details, consist of a series of steps that can be classified as reversible (ison) and irreversible (rheons). During an ison the conversion of work to surface energy is 100%, whereas during a rheon the work done is 0 and, for the case of drainage, there is loss of surface energy. Hence the total work done obtained from integrating under the capillary pressure, in the case of drainage, will be more than the change in surface energy of the system and vice versa would be true for imbibtion. During imbibition/drainage only a fraction of the total surface area, as measured by BET, is contacted by the invading non-wetting phase. Multi phase flow and mass transfer are intricately related to the surface area between the three phases. The method proposed in this work utilizes thin section analysis from samples obtained from outcrops to determine fluid saturation and interfacial surface areas between the solid–non wetting, solid–wetting and wetting – non-wetting after solidification of epoxy resin that contain two different colors, one representing water the other oil. Theory of stereology was used to estimate three-dimensional information such as interfacial areas between the two fluid phases from the two dimensional image of the phases obtained from the thin section.

Experimental

All porous media exhibit some residual wetting phase saturation when drained. In the case of case of a pack of uniform sized sphere, similar to on used by Morrow (1970), the capillary pressure curve is universal with a well-defined residual saturation. Corresponding to the residual there is a surface area associated with the wetting phase that is a measure of the inefficiency of conversion of work of displacement to the surface energy created during the drainage process and hence the work of drainage will always exceeds surface free energy. In the case of a glass bead pack the efficiency of displacement was reported to be 79%. For a more complex geometry, like that in a porous media the residual saturation is not a unique value it rather depends on the pore structure of the rock. In general the amount of microporosity tends to dictate the efficiency of conversion. The International Union of Pure Applied Chemistry defined the different types of pores as follows:

Micropores: $r < 2$ nm
Mesopores: $r = 2 – 50$ nm
Macropores: $r > 50$ nm

The micropores retain the wetting at very high capillary pressure and during drainage the fluid in these pores is not accessed by the invading non-wetting phase. The work of displacement

was calculated using the area under the capillary pressure curve that can be obtained form mercury injection, centrifuge, porous plate or any other technique.

$$\text{Work of displacement} = V_b * \phi \int_{100}^{Swi} P_c * dS_w \qquad \text{Eq 1}$$

Where, P_c is the capillary pressure

S_w is the saturation of the wetting phase

V_b is the volume of the bulk phase

φ is the porosity of the sample

Work done under the capillary pressure was used to calculate the area corresponding to it:

$$A_{mercury} = \int_{100}^{Swi} P_c * dS_w \ / (\sigma_{w\text{-}nw} * \rho_{Rock}) \qquad \text{Eq 2}$$

Where, ρ_{Rock} is the density of the rock matrix (2.65 g/cc)

$\sigma_{w\text{-}nw}$ is the interfacial tension between the wetting and the non-wetting phase

The change in surface free energy of the system is a function of the interfacial area created by the invading non-wetting phase. For this paper this value has been calculated using thin section analysis using the equation:

$$\Delta F = \sigma_{w\text{-}nw}(\Delta A_{w\text{-}nw} + \Delta A_{s\text{-}nw} \cos\theta) \qquad \text{Eq 3}$$

Where, ΔF is change in the surface free energy

$\Delta A_{w\text{-}nw}$ is the interfacial area between the wetting and non-wetting phase

$\Delta A_{s\text{-}nw}$ is the interfacial area between the solid and the non-wetting phase

$\cos\theta$ is the contact angle

Capillary pressure measurements were by mercury injection

The method and the data obtained for the work done under the capillary pressure curve sandstone (Phillips 2) sample was discussed in the last quarterly report (01/01/2005 – 03/31/2005).

Results and Discussion

Surface area analysis

The experimental procedure to obtain the thin section and application of the fundamental theorems of stereology to obtain surface areas was explained in the quarterly report (07/01/2004 – 9/30/2004). The results for the surface area analysis for the sandstone sample are presented here. From the capillary pressure curve the range for which the thin section analysis using the 10X magnification was valid was found to be between (S_w = 22 – 100 %). The size of the pixel

using this magnification was 2 microns and hence (as shown in fig.1) the wetting phase (blue) present in the pores smaller than 2 micron was not visible under the microscope.

The interfacial area between the wetting and the non-wetting phase (red – blue) interface is of much interest and many researchers (Jain et al., 2003; Kim et al., 1997; Gladkikh et al., 2003; Bradford and Leij, 1997) have used indirect methods to estimate this area in a variety of porous media. As can be seen from Fig. 2 this area increased from 0 (at S_w = 100%) to about 0.053 % of the BET surface area (0.626 m^2/g) at S_w = 75 % and then decreased to 0 at S_w = 0%. This is because the red-blue interface can form only in the pores, which constitute only a small fraction of the total surface area (TSA) available to the invading non-wetting phase. Alpak et al. (1999) had also suggested that the interfacial area between the liquid – liquid interfaces should pass through at least one maximum for some intermediate saturation. Morrow (1970) reported similar results on a pack of glass beads.

Created surface area, CSA, is the area created by the invading non-wetting phase as it displaces the wetting phase. This area increases with the decrease in the wetting phase saturation and at very low wetting phase saturation is approaches the total surface area (TSA). CSA was calculated as the sum of interfacial area between solid – red and the red – blue phase (fig 3). Most of the area related to fluid displacement is associated with the solid surface.

The TSA is only a small fraction of the BET surface area because much of the surface area is associated with microporosity. Wetting phase is not displaced from these regions. In the case of the PH2 sample the TSA exposed was 0.009m^2/g (average), which, corresponded to only about 1.4 % of the BET surface area. TSA was calculated by adding the interfacial area between the solid – red and the solid – blue phase (fig 4).

Magnification of 10 X the total length of each picture analyzed was used to obtain the surface energy of 0.27 cm (diameter of the core was 4 cm). Hence the scatter in the data may well be related to heterogeneity at the scale at which the analysis was made. The reason for choosing this magnification was that, at lower resolution, the saturations in the regions of kaolinite and dissolved feldspar would not be distinguishable from the rest of the matrix. Higher magnification would require a very large number of pictures and extremely large storage and processing capabilities.

Fig 1 Correcrted capillary pressure curve and the radii of investigation for Sandstone (PH2)

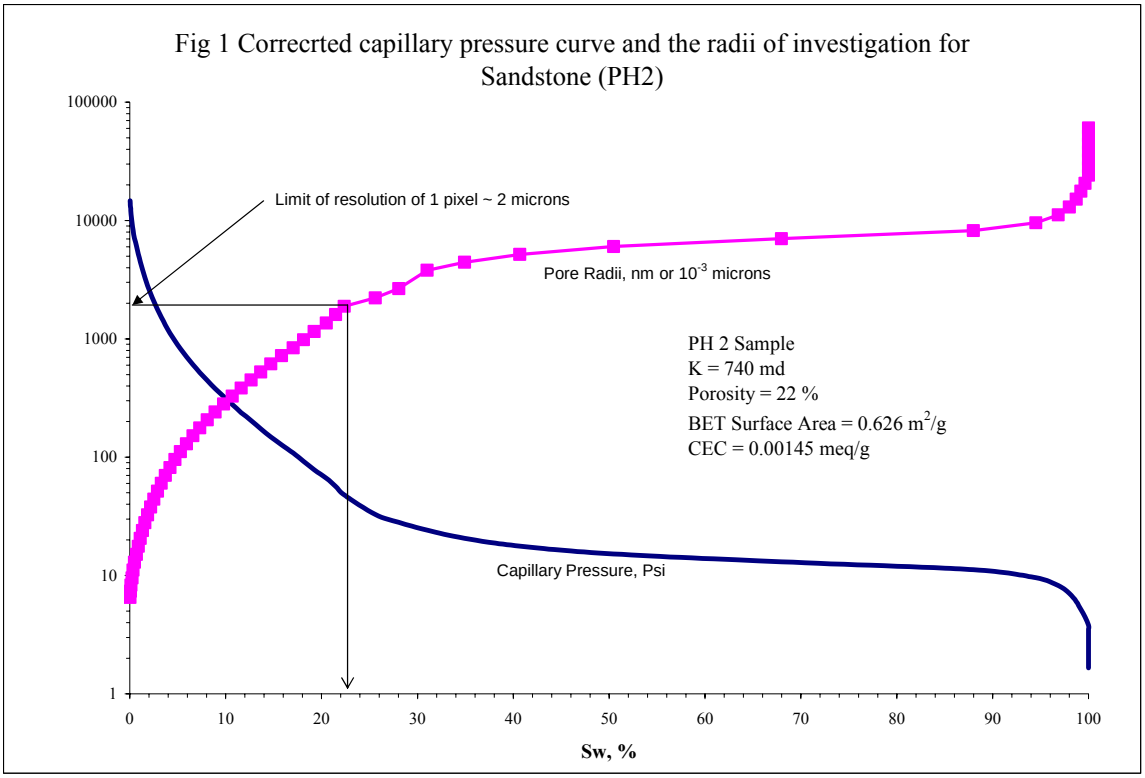

Fig 2 Variation in area between the wetting and non wetting phase as a function of the wetting phase saturation

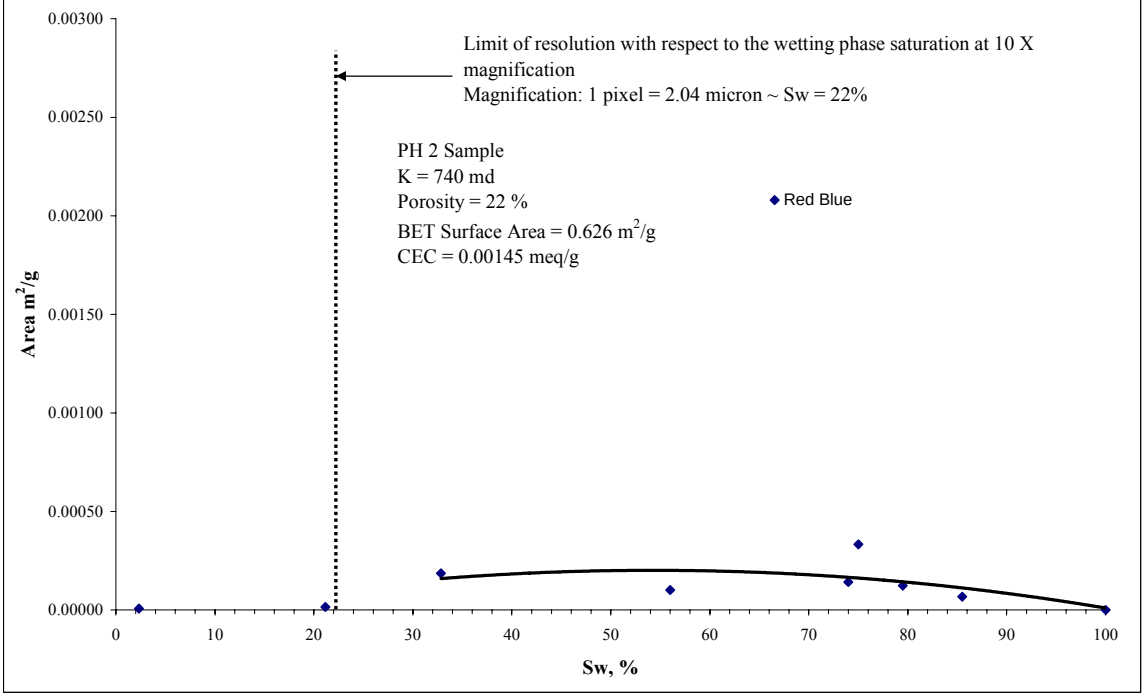

Fig 3 Variation in Created Surface Area (CSA) as a function of the wetting phase saturation

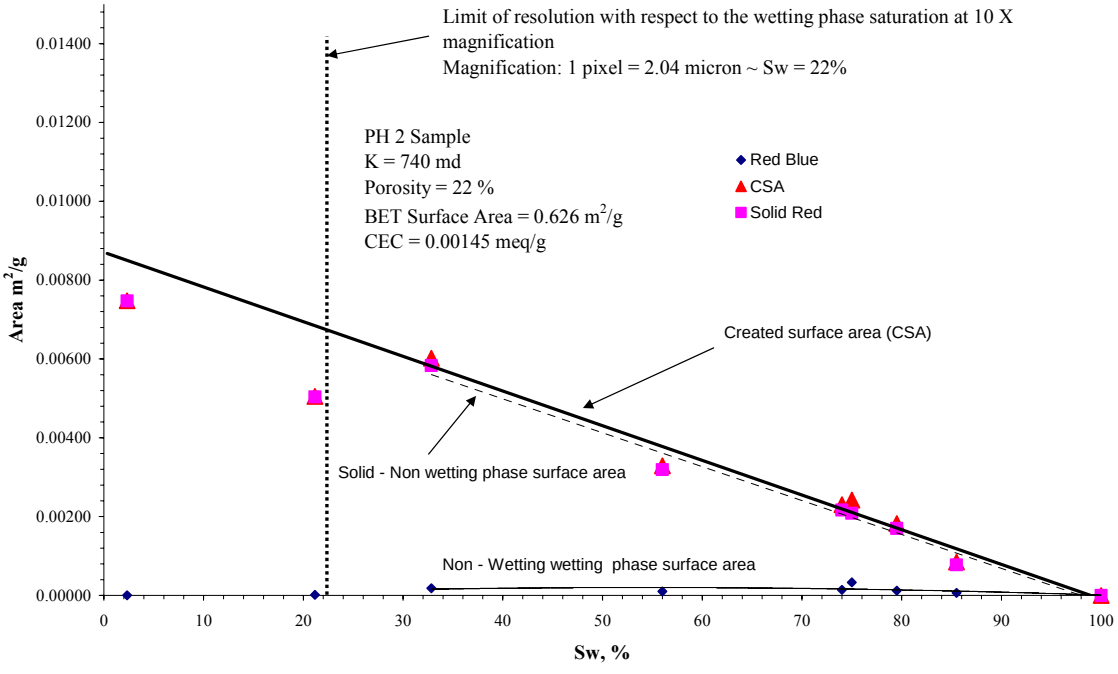

Fig 4 Total Surface Area (TSA) as a function of the wetting phase saturation

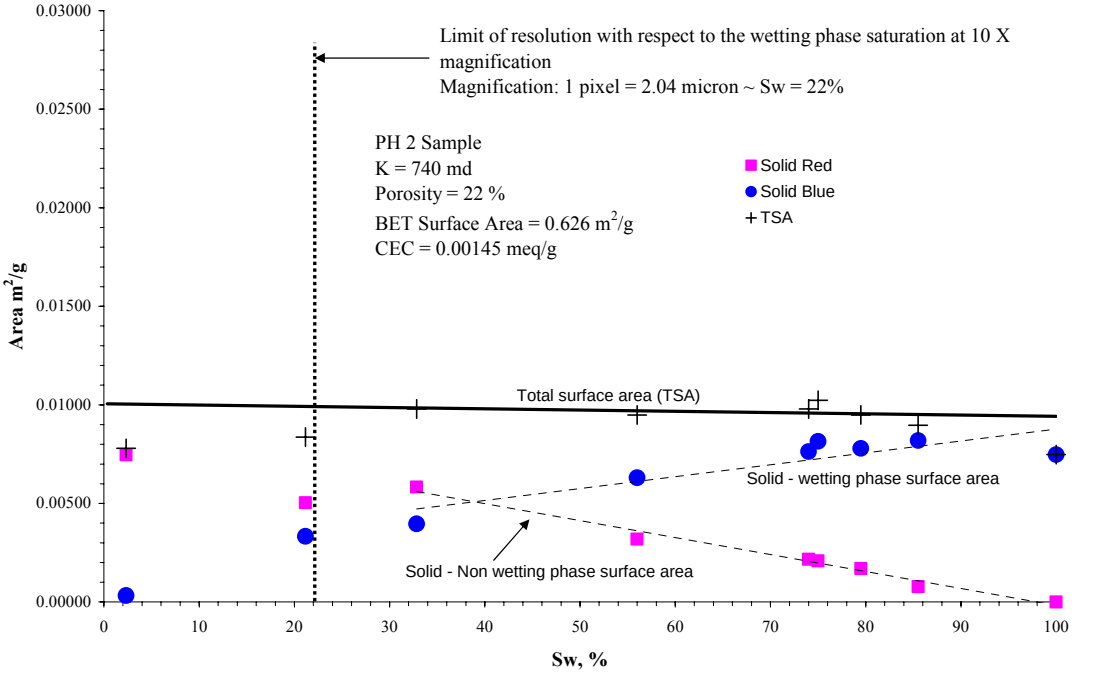

Task 2. *Imbibition in simple laboratory and mathematical network models.*

(Shaochang Wo, Herbert Fischer and Norman Morrow - unpublished manuscript)

Introduction

In spontaneous imbibition, capillary pressure is the dominant force. Poiseuille flow covers practically the whole of the flow regime. Based on the Poiseuille's law, analytical or numerical solutions of spontaneous imbibition in cylindrical capillary tubes and Hub-and-Spoke Units have been derived. Results presented in the previous quarterly reports, reveal the dependency of the advancing position of the wetting phase on the viscosity ratio as well as the ratio of the pore radii occupied by the wetting and non-wetting phases. Those results have led to new understanding of how to model the spontaneous imbibition processes in strongly water-wet cores, in which a relatively constant saturation is often observed in the imbibing water phase at the displacement front. Consequently, simple analytical models have been derived to model imbibition processes under different core boundary conditions. Namely, linear (one end or two ends open), radial (two end closed), and whole core (all faces open) flow patterns. The models have been tested against experimental data. The model provides a satisfactory fit to almost all of the experimental data.

Experimental

Modeling the spontaneous imbibition process in strongly water-wet cores

When cores are strongly water wet, a piston-like frontal movement of the imbibing water is commonly observed for all boundary conditions namely one-end-open (OEO), two-ends-open (TEO), two-ends-closed (TEC), and all-faces-open (AFO). This visual observation indicates that the pore volume ratio between the smaller pores occupied by the invading water and the larger pores occupied by the replaced oil is relatively constant behind the front. This is also consistent with the simulation results in the Hub-and-Spoke Units, where the outgoing or trapped oil is always being pushed into the larger spokes. As illustrated in Figure 2.1, the assumption is that the replaced oil is either being trapped or being pushed count-currently via the networks that are connected by the largest pores. Under this assumption, a relationship between the frontal position and the imbibition time can be derived based on the Poiseuille's law.

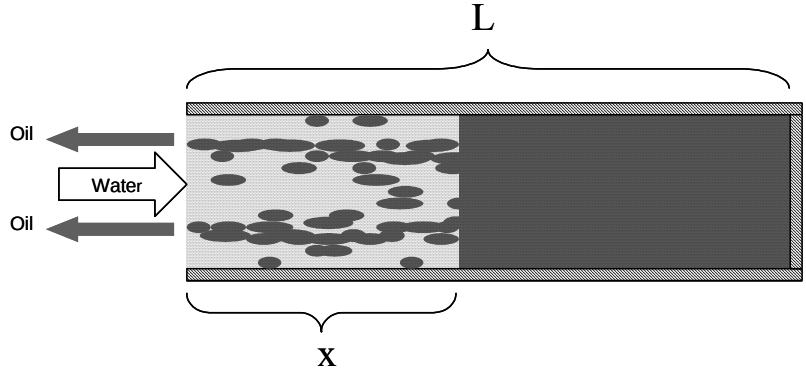

Figure 2.1. The conceptual frontal displacement of the counter-current spontaneous imbibition in strongly water-wet cores.

Similar to the spontaneous imbibition in cylindrical tubes, we model the frontal displacement as the imbibition in a set of U-shaped tubes with the water-oil contact at the bottom of the U tubes. Moreover, the radii of the two legs of the U tubes can be different. Under this configuration, the advance of the front is described as the cumulative effect of the imbibing water in individual tubes, in which the tube legs are in effect lengthened with time but the contact position remains at the bottom of the U tubes. By applying the Poiseuille's law, we obtain a mass balance equation of water flow, Eq. 2-1, at the water-oil contact front, where P_c is the capillary pressure at the contact. r_w and r_o represent the average pore radii occupied by the water and oil phases, respectively. R, ϕ, A, μ_w, μ_o are the oil recovery, core porosity, cross-section area, water and oil viscosities, respectively.

$$q_w dt = R\phi A dx, \qquad \text{where } q_w = \frac{\pi P_c r_w^4}{8x} \frac{1}{\mu_w + \mu_o (r_w^4 / r_o^4)} \tag{2-1}$$

Integration of Eq. 2-1, gives an analytical relationship between the normalized position of the front and the imbibition time, as shown by Eq. 2-2.

$$\left(\frac{x}{L}\right)^2 = \frac{\pi P_c r_w^4}{4R\phi A L^2} \frac{t}{\mu_w + \mu_o (r_w^4 / r_o^4)} \tag{2-2}$$

In the following, we propose a dimensionless model that has the same parameter setting as in Eq. 2-2. Leverett has derived a relationship between permeability, porosity, tortuosity and the radius of a parallel bundle of equal size cylindrical tubes. Intuitively, a dimensionless form of Eq. 2-2 can be rewritten as

$$x_D^2 = E(\eta) t_D \tag{2-3}$$

Here, t_D is a dimensionless time normalized by the same scaling group proposed by Ma *et al* (1997).

$$t_D = \sqrt{\frac{k}{\phi}} \frac{\sigma t}{\sqrt{\mu_o \mu_w} L_C^2} \tag{2-4}$$

The characteristic length, L_C, depends on the respective boundary conditions. Specifically, in linear flow, $L_C = L$ for OEO and $L_C = L/2$ for TEO. In radial flow, $L_C = \frac{d}{2\sqrt{2}}$ for TEC. In spherical flow, $L_C = \frac{d}{2\sqrt{3}}$. In Eq. 2-2, x_D denotes the normalized position of the front, η is the square root of the viscosity ratio, and $E(\eta)$ is a dimensionless function defined by

$$x_D = \frac{x}{L}, \qquad \eta = \sqrt{\frac{\mu_o}{\mu_w}}, \qquad E(\eta) = \frac{a}{\frac{1}{b\eta} + b\eta} \tag{2-5}$$

In addition to the viscosity ratio, $E(\eta)$ is a function of two dimensionless parameters, *a* and *b*. As indicated in Eq. 2-2, they are determined by the factors related to the imbibing flow path of the wetting phase as well as the outflow path of the non-wetting phase. When cores are water wet, the average radius of pores occupied by the wetting phase is smaller than the average radius of pores occupied by the non-wetting phase. Because parameter *b* indicates the squared ratio of average pore radii occupied by the wetting and non-wetting phases, *b* should be between 0 and 1.

By assuming a piston-like frontal displacement, we can estimate the normalized recovery, R_D, as a function of t_D from Eq. 2-3. For linear, radial or spherical flows, the conversion between x_D and R_D is given by Eq. 2-6, 2-7, or 2-8, respectively.

Linear flow: $x_D = R_D$ (2-6)

Radial flow: $x_D = 1 - \sqrt{1 - R_D}$ (2-7)

Spherical flow: $x_D = 1 - (1 - R_D)^{\frac{1}{3}}$ (2-8)

Because of the non-symmetrical flow pattern, it is difficult to derive a simple analytical model for the imbibition process of AFO. However, an AFO imbibition process can be approximated by a combination of radial flow and spherical flow. Equivalent in total volume, the shape of a regular core with a diameter of *d* and a length of *L* is close to a cylinder with hemispherical ends. The rod has a length of *L - 4d/3*. Both the rod and the two half spheres have the same diameter, *d*. Finally, the recovery of AFO can be estimated from the combined recoveries from the rod and from the two half spheres.

$$R_{D\_AFO} = (1 - \frac{2d}{3L})R_{D\_radial} + \frac{2d}{3L} R_{D\_spherical} \tag{2-9}$$

When the same value of *E* is assumed for both radial and spherical flows, the normalized recovery for AFO can further be derived as a function of the dimensionless time of the radial flow, Eq. 2-10.

$$R_{D\_AFO} = (1 - \frac{2d}{3L})(1 - (1 - \sqrt{Et_{D\_radial}})^2) + \frac{2d}{3L}(1 - (1 - \sqrt{\frac{3}{2}Et_{D\_radial}})^3) \tag{2-10}$$

The proposed models of Eq. 2-3 and 2-10 were tested against experimental data. A linear correlation between the advancing front and the imbibition time is evident on the log-log plot for almost all cases but the slope of 0.5 was not always obtained, especially for linear flow. By freeing the power index, we propose an extended imbibition model of Eq. 2-11.

$$x_D^n = E(\eta)t_D \tag{2-11}$$

The extended model of Eq. 2-11 has three dimensionless parameters, *n*, *a*, and *b*. For matched-viscosity cases, i.e. $\eta=1$, Eq. 2-11 reduces to a 2-parameter model in *n* and *E(1)*.

Results and Discussion

The extended imbibition model, Eq. 2-11, has also been tested in comparison against experimental data. The tested data set includes the OEO, TEC, and AFO cases under matched viscosities as well as AFO cases under non-matched viscosities. Apart from data recorded at the initial or final stages of the experiments, a clear linear correlation between the advancing front and the imbibition time emerges on the log-log plot for almost all of tested cases. It supports the assumption applied in the model derivation. When $n=2$, it indicates a linear correlation between x_D and $\sqrt{t_D}$. For tested TEC and AFO cases, we found that the best fit consistently result in *n* values around 2. However, a larger range of *n*, between 1.6 and 2, was observed in modeling the OEO cases. As examples, comparisons between the experimental data and modeled curves are presented in Figure 2.2 and 2.3. The core and fluid properties for these three examples are given in Table 2.1. The table also shows the *n* and *E(1)* values that are used to plot the modeled curves. Note that, the AFO example in Figure 2.3, both the modeled and experimental plots are scaled by the t_D of radial flow.

In summary, the 3-parameter imbibition model, Eq. 2-11, provides a satisfactory fit to most of the experimental data. The model is reduced to a 2-parameter model, i.e. *n* and *E(1)*, for matched-viscosity imbibition. As observed for much of the experimental data, a linear correlation between the advancing front and the square root of the time, i.e. $n=2$, implies that the spontaneous imbibition process is largely dominated by "local phenomena", in which the capillary pressure at the water-oil contact generates many local inlet-outlet flow paths. Further testing of the model will be conducted when new experimental data become available.

Table 2.1. Core and fluid properties of the three imbibition experiments used in the comparison. The matched-viscosity experiments were modeled by two parameters, *n* and *E(1)*.

	OEO	TEC	AFO
L [cm]	6.603	6.428	6.435
d [cm]	3.741	3.736	3.761
L_c	6.603	1.321	1.229
kg [cm^2]	7.723E-10	6.99E-10	5.952E-10
σ [dynes/cm]	33.86	33.86	32.36
μo [cp]	21.87	21.870	59.130
μw [cp]	22.52	22.520	59.300
Φ	0.169	0.173	0.178
n	2	2	2
E(1)	0.014	0.0025	0.0038

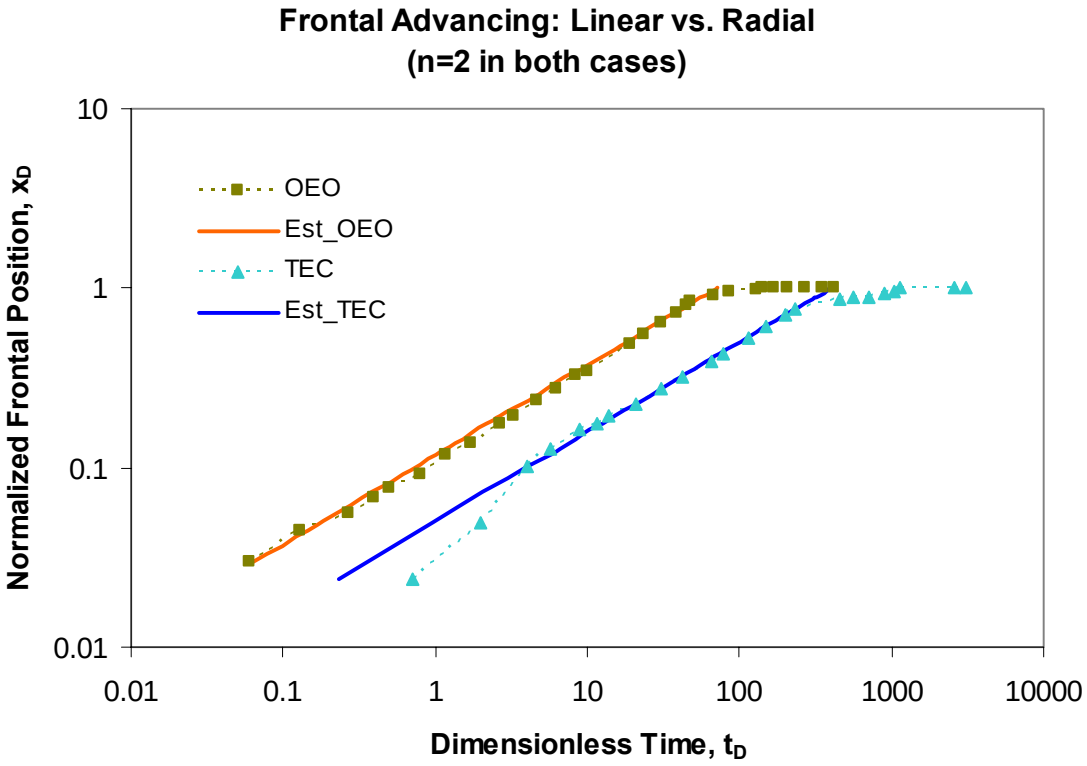

Figure 2.2. Examples of the linear correlation between x_D and $\sqrt{t_D}$, i.e. n=2, where a matched viscosity of 22 cp was used for both OEO and TEC cases.

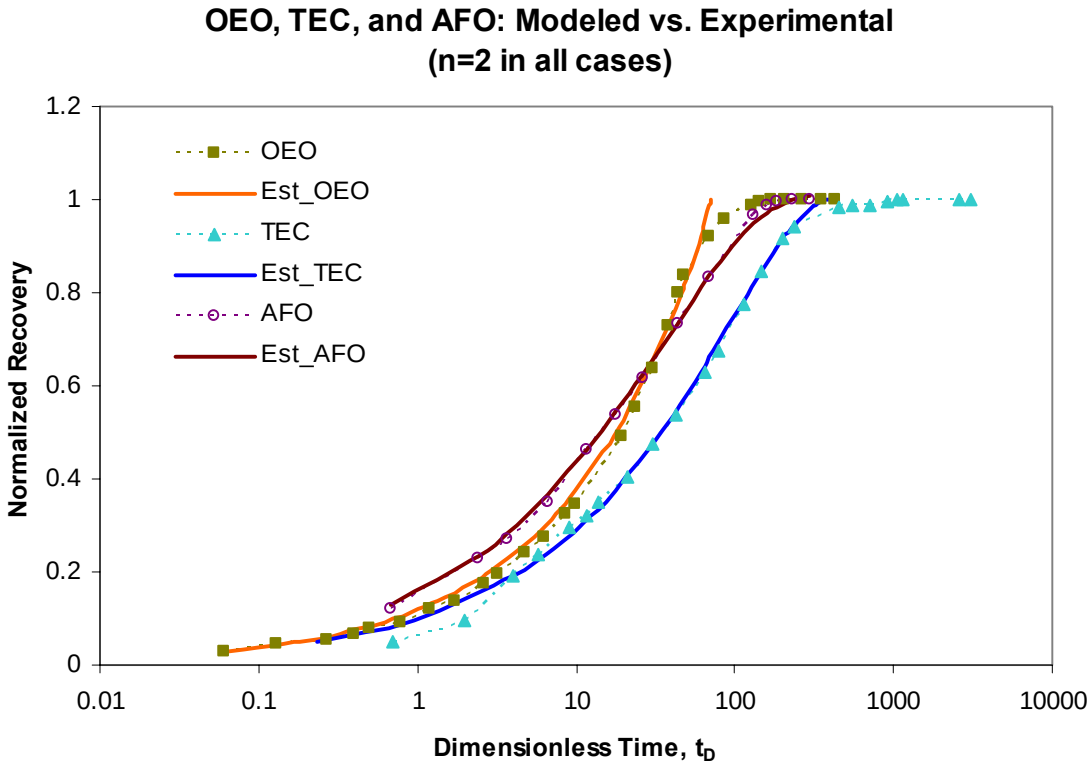

Figure 2.3. Comparison between the modeled recoveries (solid curves) and the experimental data (dashed lines with dots).

Task 3. Novel observations on fluid pressures during imbibition and the mechanism of non-wetting phase production at the imbibition face.

(Yu Li, Douglas Ruth, Geoffrey Mason and Norman Morrow - in press with *Journal of Petroleum Science & Engineering*)

Abstract

Four water/oil and four oil/air linear counter-current spontaneous imbibition experiments were performed on Berea sandstone cores with permeabilities ranging from 0.065 to 1.094 μm^2. The cores were initially 100% saturated with non-wetting phase and all faces except one end were sealed. The experiments showed a clear frontal displacement mechanism. Capillary pressure was the driving force of the imbibition process. As well as viscous drag in both phases between the imbibition front and the open face, there is a significant opposing capillary back pressure associated with production of non-wetting phase at the open face. The location of the imbibition front, the overall changes in core saturation, and the pressure in the nonwetting phase in the dead end space ahead of the imbibition front, were monitored during the course of imbibition. The dead end pressure was essentially constant after a short start-up period. The distance advanced by the imbibition front was proportional to the square root of time. Based on the assumption that the properties of Berea sandstone of different permeabilities can be scaled, the experimental data were matched by numerical simulation to predict the saturation and

pressure profiles, the saturation and capillary pressure at the imbibition front, and the capillary back pressure at the open face. The ratio of the capillary back pressure to the estimated capillary pressure at the imbibition front ranged from approximately 1/3 to 2/5, for oil displacing air, to approximately 1/9 to 1/4, for water displacing oil.

1. Introduction

The process of displacement of a nonwetting phase (NWP) from a porous medium by spontaneous imbibition of a wetting phase (WP) is often counter current (Morrow and Mason, 2001). In core analysis studies, spontaneous imbibition measurements are usually made on cylindrical cores with all faces open to imbibition. However, the use of cylindrical cores with only one end face open simplifies the analysis of the process because it forces the displacement to be linear with equal and opposite volumetric flows of WP and NWP at all distances from the open face. A similarity solution for one-dimensional COUCSI with a semi-infinite boundary has been reported (Li *et al.*, 2003)

During counter current spontaneous imbibition (COUCSI) at very strongly wetted (VSW) conditions, displaced NWP is produced as bubbles at the open face (Li *et al.* 2003). The pressure associated with these bubbles, which we will term the capillary back pressure, P_{cb}, opposes production of NWP and can be significant. P_{cb} is proportional to the interfacial tension (the term interfacial tension is applied to both oil/water and air/oil) and depends inversely on the size of the large pore throats at the surface and the size of pores connected with them in the open face region, through which the NWP exits the core.

One way to reduce the outlet NWP pressure is to allow NWP to vent from the otherwise sealed end of the core thus making the process co-current. Wang (1999) showed that this increased the rate of recovery of air by imbibition of oil by about an order of magnitude. However, when the flow is co-current, the mechanism of imbibition is distinctly different from COUCSI.

In the present study of COUCSI, results were obtained for displacement of mineral oil by water, and of air by the same mineral oil, for three distinct types of Berea sandstone. These fluid pairs give very strongly wetted conditions with about 800 fold difference in viscosity ratios of the nonwetting to wetting phases. The pressure at the dead end, P_{end}, the location of the imbibition front, and production versus time were recorded. The information obtained by experiment was matched by numerical simulation in order to estimate the saturation and pressure profiles, the capillary pressure, $P_{c\,f}$, at the front, and the capillary back pressure at the open core face, P_{cb}.

2. Experiments

Eight Berea sandstone core samples, 3.8 *cm* in diameter and about 7 *cm* in length, were selected from three distinct types of Berea sandstone. Permeability ranged from 0.065 μm^2 to 1.094 μm^2 and porosity from 17% to 22%. The cylindrical surface and one end-face of each core were sealed with transparent epoxy resin. One end of a Nylon tube (inner diameter of 1.5 *mm* and outer diameter of 3 *mm*) was embedded a short distance into the core at the otherwise sealed end. The other end of the tube was connected to a pressure transducer. The tube and the connected transducer space were filled with oil.

Table 1 Core and fluid properties and measured characteristics of imbibition tests.

COUCSI	OIL / WATER				AIR / OIL			
μ_{nw}/μ_w	0.0038 *Pa.s*/0.00102 *Pa.s*				0.000018 *Pa.s*/0.0038 *Pa.s*			
σ	48.85*mN/m*				25.87*mN/m*			
CORE	H8O	H2O	M3O	L8O	H8A	H4A	M3A	L5A
d (cm)	3.796	3.794	3.792	3.797	3.789	3.789	3.793	3.8
L (cm)	6.864	6.18	7.493	6	7.12	7.523	7.365	6.806
K (μm^2)	1.094	1.048	0.681	0.065	1.054	0.973	0.503	0.07
Φ	0.221	0.22	0.208	0.171	0.219	0.217	0.202	0.172
t_{FAB} (hr)	2.5	2.1	4.7	14.9	7.1	7.9	13.9	66.7
t_{ep} (hr)	8.3	6.3	15	41.7	19.4	20.8	36.1	152
S_{w0}	0.5	0.5	0.52	0.43	0.5	0.5	0.52	0.53
P_{end}(*kPa*)	3.140	3.120	4.830	9.080	1.950	2.240	2.700	4.600

Four water/oil and four oil/air imbibition tests were performed (Table 1). For each fluid pair, duplicate tests were run on the highest permeability sandstone and single tests on the intermediate and low permeability rock. All experiments were conducted at ambient conditions, 21^oC and atmospheric pressure (79 *kPa,* 2300 *m* elevation). Soltrol 220®, of 0.0038 *Pa.s* viscosity, was used as the oil phase. Polar impurities were removed from the refined oil by flow through silica gel and alumina. In the water/oil experiments the aqueous phase was 10,000 *ppm* NaCl brine of 0.00102 *Pa.s* viscosity. Interfacial tensions were 48.9*mN/m* for the water/oil phase and 25.9*mN/m* for oil/air. The viscosity of air was 0.000018 *Pa.s*. In each imbibition experiment, volumetric production, imbibition front position, and NWP dead end pressure were measured simultaneously by techniques described below.

2.1. Water/oil imbibition

In the water/oil experiments, the core was positioned with the open face up. The recovery was determined from the volume of produced oil collected in an inverted closed funnel above the core (Fig.1). A series of electrodes were embedded in the core. The distance of frontal advance was detected from the onset of electrical conductivity when the brine front contacted a particular electrode.

2.2. Oil/air imbibition

In the oil/air experiments, the core was immersed in oil contained in a beaker with the open face down (Fig. 2). The beaker was set on a balance with the pressure sensing tube fixed to a stand. The recovery was determined from the incremental loss in weight resulting from imbibition of oil into the core. The ratio of the outside radius of the nylon tube connected to the transducer to the inside radius of the beaker and decrease in the oil level in the beaker were both so small that the influence of buoyancy on recovery could be neglected. However, for measurements that lasted for more than about one day, a small correction was made for loss of oil by evaporation. In these tests, the distance advanced by the oil was obtained by direct observation of the invading front through the transparent resin coating.

2.3. Capillary pressure at the displacement front

In order to estimate the capillary pressure at the imbibition front, preliminary studies were run on the highest permeability sandstone butted to a section of low permeability sandstone which

served as a semi permeable membrane set at the end face. Further details are given with the results.

3. Results and Discussion

3.1. Effect of gravity

The effect of gravitational forces acting over the core length is generally very small compared to capillary forces. Imbibition tests performed with the open end of the core facing either upward or downward showed very little difference in recovery behavior.

3.2. Mode of nonwetting phase production.

It was observed that the mode of NWP production was very different for the two fluid pairs. For imbibition of water, oil is produced almost instantaneously after immersion in brine. The oil appears as numerous small bubbles which tend to coalesce at the open face. For oil/air imbibition, there is no immediate production of air. When air bubbles do appear, they come from only one or two points on the open face.

3.3. Water/oil imbibition

Results presented for Core H80 in Fig 3 are typical of the four data sets obtained for water/oil imbibition. During the frontal flow period, the volume of water imbibed, Q_w, the distance advanced by the imbibition front, x_f, and the end pressure, P_{end} , were recorded. P_{end} , rose quickly for the first 60 seconds. It then remained constant at about 3.140 *kPa* until the front reached the end of the core (after 2.5 *hours*). The ratio of Q_w/V_ϕ to x_f/L_c (the average saturation behind the front) was 0.42 until the imbibition front reached the end of the core. This behavior is consistent with the existence of a self-similar displacement. Both the fractional pore space filled (Q_w/V_ϕ) and the fractional distance imbibed (x_f/L_c) were proportional to the square root of time (Fig.3).

After the front reached the end of the core, the rate of oil recovery decayed away from the square root of time relationship. The pressure measured at the closed end (P_{end}) decreased and eventually dropped to zero about 9 *hours* after the start of imbibition, possibly because of gradual loss of connectivity between the nonwetting phase in the core and that in the transducer. The final recovery was 50%.

Qualitatively comparable results were obtained for all four Berea sandstones with permeability ranging from 0.065 to 1.048 μm^2 (see Table 1). All end pressures eventually dropped to zero after the front reached the end of the core.

3.4. Oil/air imbibition

Example results for oil/air imbibition are presented in Fig. 4 (Core H8A). After the start of imbibition, P_{end} rose to a peak value of 2.118 *kPa* at 150 seconds and then dropped to 1.980 *kPa*. The initial build up in pressure corresponded to compression of the air initially contained in the core. No air was produced until about 3% pore volume had been invaded for the high permeability cores. After the drop in pressure that followed the very short initial compression stage, P_{end} remained constant whilst the imbibition front traversed the core. In contrast to water/oil, the pressure decreased only slightly after the front reached the closed end. This may be because the air in the tube connected to the transducer is connected to pockets of trapped air. Pressure is maintained because, unlike an essentially incompressible liquid phase, the trapped air

can undergo changes in volume with only small change in pressure. Apart from the early time behavior, the overall increase in oil saturation and the distance of invasion were, as for water/oil imbibition, proportional to the square root of time during the frontal flow period. When the front reached the closed end of the core 7 *hours* after the start of imbibition, the NWP recovery, given by Q_w/V_ϕ, was 42%.

After the frontal flow period, the rate of recovery decayed and had almost ceased after 22 *hours* by which time the recovery had risen to 50%. After the front had reached the end of the core, the end pressure dropped by about 1% (about 0.020 *kPa*) even though no air was being produced.

Qualitatively comparable oil/air results were obtained for all four Berea sandstones with permeability ranging from 0.070 to 0.973 μm^2 (see Table 1). During the post contact period, the decrease in P_{end} tended to be slightly more for the less permeable cores. However, even for the least permeable core, L5A (0.070 μm^2), P_{end} had decreased only by 2% after 86 *hours*.

3.5 Estimation of capillary pressure at the imbibition front, P_{cf}

For the highest permeability Berea, an estimate of the frontal capillary pressures, P_{cf}, during COUCSI was made. The principle of the method is that if the frontal capillary pressure, P_{cf}, is lower than the capillary back pressure, P_{cb}, COUCSI will stop and the transducer will indicate a pressure which is assumed to be equal to the frontal capillary pressure. This was achieved by butting a slice of low permeability sandstone at the open face of a high permeability core. COUCSI initially occurred in the low permeability slice. Movement of the imbibition front eventually stopped in the high permeability core because the capillary pressure at the front was less than P_{cb} for the low permeability sandstone end piece. Estimates of P_{cf} in cores with permeability of about 1.05 μm^2 for both water/oil and oil/air cases were obtained from the increase in end pressure. Details of core properties and results are given in Table 2. The estimated frontal interfacial curvatures (P_c/σ) were the same (0.254 μm^{-1}) for the two cases. The agreement of the curvatures, is consistent with the assumption that very strongly wetted conditions pertained for both water/oil and oil/air imbibition.

Table 2. Capillary pressures at the imbibition front.

COUCSI	OIL/WATER	AIR/OIL
μ_{nw}/μ_w	0.0038 *Pa.s*/0.00102 *Pa.s*3.7255	0.000018 *Pa.s*/0.0038 *Pa.s*
σ	48.85*mN/m*	25.87*mN/m*
CORE	H6O	H5A
d(cm)	3.795	3.79
L(cm)	6.967	8.04
K(μm^2)	1.067	1.042
ϕ	0.222	0.221
P_{cf}(*kPa*)	12.359	6.600
$P_{cf}/\sigma\ \mu m^{-1}$	0.253	0.255

3.6. Simulation

Differential equations for the imbibition behavior in terms of permeability, relative permeability, and capillary pressure were solved numerically. Details of the simulation are provided in Appendix A. A set of k_{rw}, k_{rnw} and P_c curves were found that were consistent with

that of water/oil and oil/air COUCSI performance in the Berea sandstone with a permeability of 1.050 μm^2. It was assumed that the relative permeabilities and the interfacial curvature (P_c/σ) versus saturation relationships were correlated. Solutions were repeated to find the equation parameters that best simulated the experimental results (see Appendix B). The simulation variables of the curves for the 8 cores are shown in Table 3.

Table 3 Parameters of relative permeability and capillary pressure functions

COUCSI	OIL/WATER				AIR/OIL			
CORE	H8O	H2O	M3O	L8O	H8A	H4A	M3A	L5A
S_{wi}	0	0	0	0	0	0	0	0
S_{w0}	0.525	0.54	0.56	0.44	0.505	0.49	0.515	0.53
S_{wf}	0.29	0.25	0.3	0.32	0.29	0.285	0.26	0.345
k_{rw} at S_{w0}	0.6	0.6	0.6	0.6	0.75	0.75	0.75	0.75
k_{rnw} at S_{w0}	10^{-10}	10^{-10}	10^{-10}	10^{-10}	10^{-10}	10^{-10}	10^{-10}	10^{-10}
N_{nw}	2.6	2.6	2.6	2.6	2.6	2.6	2.6	2.6
k_{rnw} at S_{wf}	10^{-10}	10^{-10}	10^{-10}	10^{-10}	10^{-10}	10^{-10}	10^{-10}	10^{-10}
k_{rw} at S_{wf}	0.04	0.04	0.04	0.04	0.0582	0.0582	0.0582	0.0582
N_w	3	3	3	3	3	3	3	3
P_c at S_{wf} (kPa)	12.359	12.000	14.000	23.200	6.500	6.650	7.590	10.260
P_c at S_{w0} (kPa)	1.300	1.100	2.800	5.730	1.940	2.200	2.660	4.400
N_{pc}	1.75	1.75	1.75	1.75	1.75	1.75	1.75	1.75

Experimental and simulated results are presented in Fig. 5 for water/oil (Core H8O) and in Fig. 6 for oil/air (Core H8A). The initial period during which the air was compressed is not simulated because, in the present analysis, the fluids are assumed to be incompressible.

3.6.1 Saturation profiles

The simulation showed the conditions under which the frontal wetting phase saturations are finite. The measured WP saturations of both water/oil and oil/air imbibition when the front arrives at the dead end boundary were between 0.38 and 0.46 for the 8 samples. The final wetting phase saturations for both water/oil and oil/air imbibition were between 0.43 and 0.53 for all tested samples. The development of the simulated saturation profiles as the front travels through the core is illustrated in Fig. 7. The simulated profiles for water/oil are more curved at both the imbibition front and at the open face than for oil/air. This reflects the lower mean transmissibility at the front and at the exit end of the profile when oil is the nonwetting phase. The frontal WP saturations for both oil/air and water/oil imbibition were between 0.25 and 0.345 for the simulations for all tested samples. Because of the similarity solution, the profiles in the frontal flow period can be collapsed into a single curve by normalization with respect to distance advanced. The saturations in the post contact period rise globally and eventually reach the saturation at the outlet, S_{w0}.

It is noted that, even though the viscosity of air is lower than water and the oil is 3.8 *cp* in both water/oil and oil/air imbibition, the frontal period flow rate in the water/oil case is about three times faster than in the oil/air case for the same recovery. For example, from Figs. 5 and 6 and Table 1, t_{FAB} for water/oil is 2.5 *hours* versus 7 *hours*. for oil/air. An important contributing factor to this difference is that the interfacial tension of water/oil is almost twice that for oil/air. Also the viscosity of the WP in the oil/air case is 3.8 times the viscosity of the WP in the water/oil case. Because relative permeability for the WP in Berea sandstone is much lower than relative permeability for the NWP over a large part of the saturation range, WP viscosity also

contributes to lower flow rate of WP (oil) in the oil/air case. From the two phase flow analysis presented in Appendix A, it is shown that the rate depends on the integral of the mobility

3.6.2 Pressure profiles

As imbibition progresses, the pressure profiles stretch over an increasing distance from the core inlet as shown in Fig. 8 for water/oil and in Fig. 9 for oil/air. The value of capillary back pressure, P_{cb}, was determined from the difference between $P_{end,}$ measured during the frontal flow period, and the pressure drop in the NWP that drives the viscous flow. For imbibition of brine against 0.0038 *Pa.s* oil, the value of P_{cb} was 1.3 *kPa* in the 1.094 μm^2 Berea sandstone core. The measured P_{end} during the frontal flow period was 3.140 *kPa*. For the oil/air results, from the enlarged simulated distribution of the NWP pressure shown in Fig. 9, it can be seen that the behavior of P_{nw} in the oil/air case is comparable to that in the water/oil case; however, P_{end} is only 0.038 *kPa* higher than P_{cb}. This difference can be neglected for most practical purposes.

The overall character of the pressure behavior is consistent with expectations based on the similarity solution. The solution infers that for the advance of any particular saturation, S_w, along the core, the difference between its associated capillary pressure and the back capillary pressure ($P_c(S_w) - P_{cb}$) is constant until the front contacts the closed end of the core.

3.6.3 COUCSI displacement curvatures

Through simulation it was found that the experimental COUCSI behavior in both water/oil and oil/air cases could be matched closely by typical relative permeability and capillary pressure curves (Appendix B). Simulations performed for water/oil COUCSI in core H8O and for oil/air COUCSI in H8A (Figs. 5 and 6) are of special interest because this was the high permeability sandstone (K=1.05 μm^2) for which P_{cf} had been estimated by experiment (see Table 2). If the relative permeabilities, scaled for differences in end points, are assumed to be identical for all permeabilities and the capillary pressures scale by the Leverett (1939) function, then the pair of P_{cf} and P_{cb} for any core can be found by running the simulations until the three experimental curves prior to FAB are matched. This stage of the simulation provides the average saturation from the open face to the imbibition front. Simulation of the changes in saturation profile along the core requires that the post contact production also be matched.

The simulated values of P_{cf} and P_{cb} in water/oil and oil/air cases determined for the different permeability Berea sandstones are listed in Table 2. The P_{cb} in the oil/air cases is almost equal to P_{end} in the frontal flow period because resistance to flow of the very low viscosity NWP (air) is very small. For water/oil imbibition, P_{cb} is significantly lower than P_{end} in the frontal flow period because of the viscous resistance to flow of the NWP liquid.

Comparison of water/oil and oil/air capillary displacement mechanisms can be made in terms of effective radii given respectively by capillary pressure and permeability. Porous media can be characterized by the radius of an equivalent parallel bundle of equal tubes model (the Leverett microscopic pore radius), $r_L = \sqrt{8K/\phi}$. Pore radii corresponding to capillary pressure at the core face or the front (P_{cb} or P_{cf}) are given by $2\sigma/P_c$. Plots of the interface radius of curvature versus the Leverett radius are presented in Fig. 10. Both radii increase together as expected. Interfacial curvatures at the displacement front, P_{cf}/σ, for a given core are the same for both water/oil and oil/air imbibition (see Fig. 10).

The radii at the open face, r_b, (associated with the capillary back pressure, P_{bp}), are much lower for production of oil (water/oil imbibition) than for production of air (oil/air imbibition). This is probably due to the differences in conditions at the onset of production. For imbibition of

water against oil, oil is produced almost instantaneously after immersion in brine. For imbibition of oil against air, because of the compression period, production of air bubbles is delayed. As oil invades the core, oil/air interfaces drive into the core building up the air pressure until the compressed air counterflows through a series of pore throats and vents at the open face. The selectivity of gaining the path by which gas is produced explains why gas bubbles are produced from only one or two locations on the open face. Furthermore the exit pores are not likely to be the largest pores at the core face. In contrast, oil bubbles appear almost instantaneously at many points on the open face. The oil bubbles come from throats and pores of larger than average size in the vicinity of the open face.

The scaled interfacial curvature, P_{cb}/σ, associated with back pressure at the open face in the oil/air case range from about 2/5 down to 1/3 of the interface curvature at the front, C_f. For water/oil COUCSI the ratio of C_b ranges from about 1/4 down to 1/9 of C_f. Thus the contribution to the relative reduction in rate of flow of the NWP because of the capillary back pressure at the open face for oil/air imbibition is about 2.4 to 3 times that for water/oil imbibition.

4. Conclusions

1. A period of frontal flow has been identified for linear COUCSI during which the distance advanced by the front is proportional to the square root of time. This result is consistent with a similarity solution for the frontal advance period.

2. The pressure of the nonwetting phase in the dead end space ahead of the imbibition front is constant from a short time after the onset of imbibition until the front arrives at the core boundary.

3. The capillary back pressure associated with production of NWP at the open face of the sample, is essentially constant during the frontal flow period. The production mechanism at the open face is basically a drainage process.

4. If the capillary pressure in the core is higher than the capillary back pressure, imbibition will occur. The rate of counter-current imbibition is proportional to the interfacial tension and depends on the integral of the mobility along the invaded portion of the core.

5. The capillary pressure and wetting phase effective permeability at residual nonwetting phase saturation can be determined from measurements of the location of the imbibition front versus time, recovery versus time, the dead-end non-wetting-phase pressure, and the absolute permeabilities to brine and oil. Typical relative permeabilities and imbibition capillary pressure curves can be tuned to match the capillary pressure at the front and the back pressure associated with production of the nonwetting phase.

6. From simulations that assume fixed relative permeabilities and scaled imbibition capillary pressure, the capillary back pressure in the oil/air case is about 2/5 down to 1/3 and in the water/oil case about 1/4 down to 1/9 of the capillary pressure at the imbibition front in Berea sandstone with permeabilities ranging from 0.065 to 1.1 μm^2.

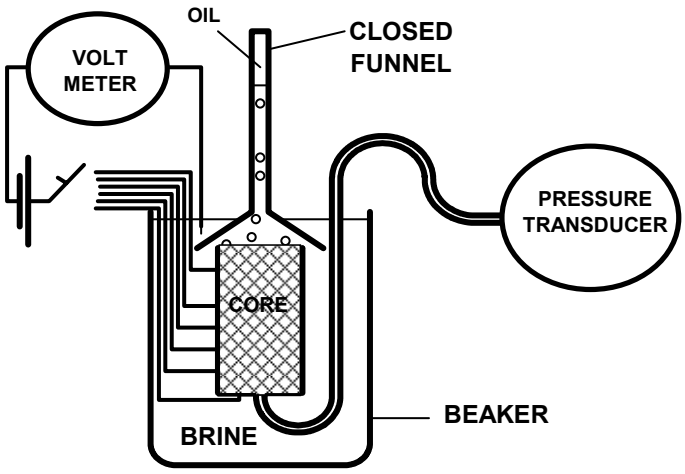

Fig.1. Apparatus for simultaneous measurements of production, location of the front, and dead end pressure during water/oil spontaneous imbibition.

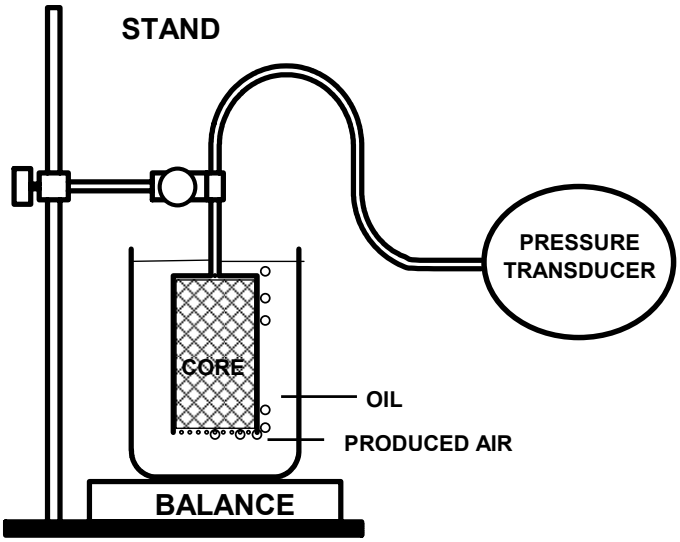

Fig. 2 Apparatus for simultaneous measurements of production, location of the front, and dead end pressure during oil/air spontaneous imbibition.

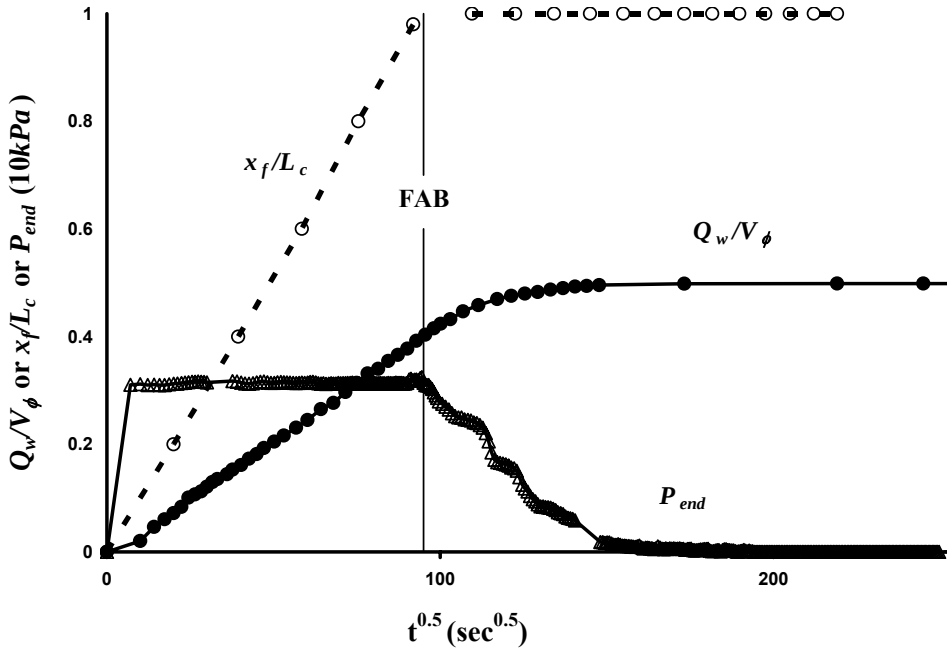

Fig. 3 Typical experimental results for water displacing oil versus square root of time (Core H8O). Q_w/V_ϕ is the fractional saturation of total pore space filled by the invading wetting phase. x_f/L_c is the fraction of the bulk volume of the core (proportional to fraction of pore volume and also the fractional distance through which the front has advanced as determined by electrical contact. P_{end} is the pressure measured at the dead end. FAB (front at boundary) indicates the time when the front arrives at the dead-end. Apart from very early time, the distance advanced by the front and the production prior to FAB are proportional to the square root of time.

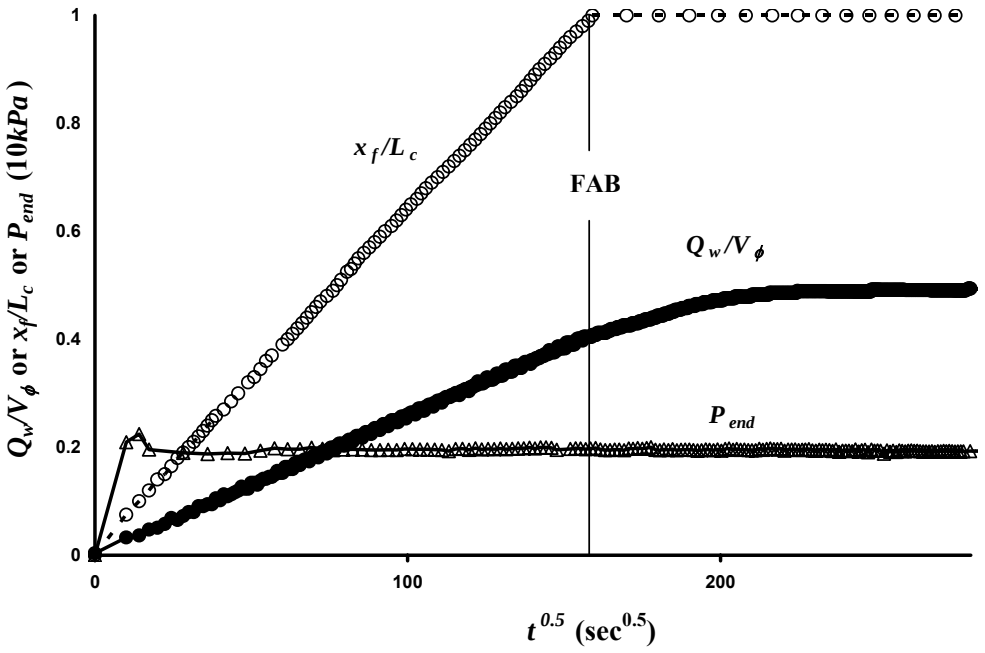

Fig. 4 Typical experimental results for imbibition of oil against air versus square root of time (Core H8A). Apart from very early time, the distance advanced (determined visually) and the production prior to FAB are proportional to the square root of time.

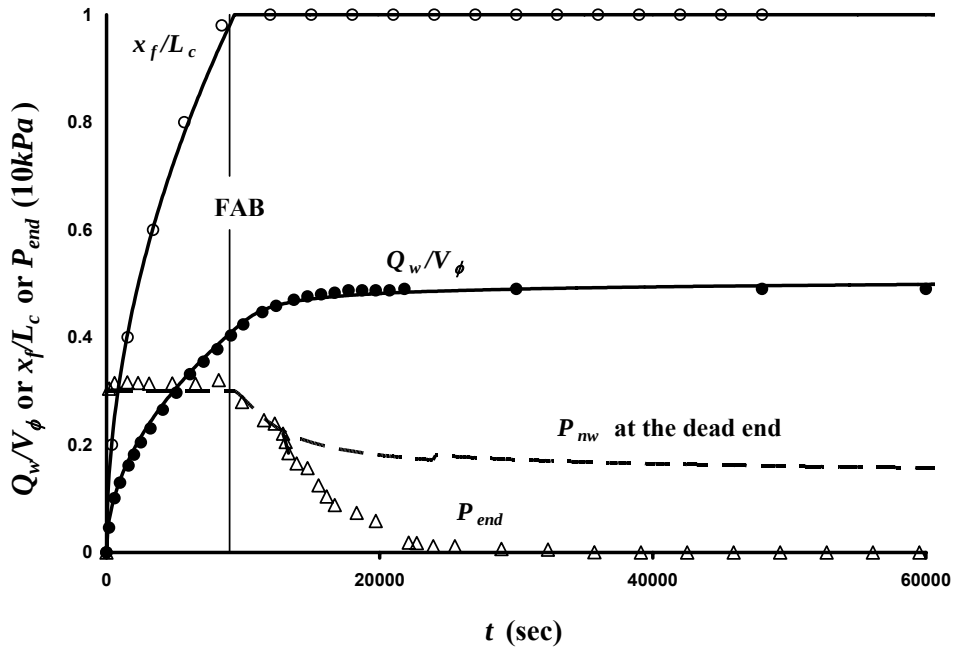

Fig.5: Comparison of experimental and simulated results for imbibition of brine against oil (Core H8O). The points (reduced in number from the results presented in Fig.3) are the experimental data; the lines are from simulations.

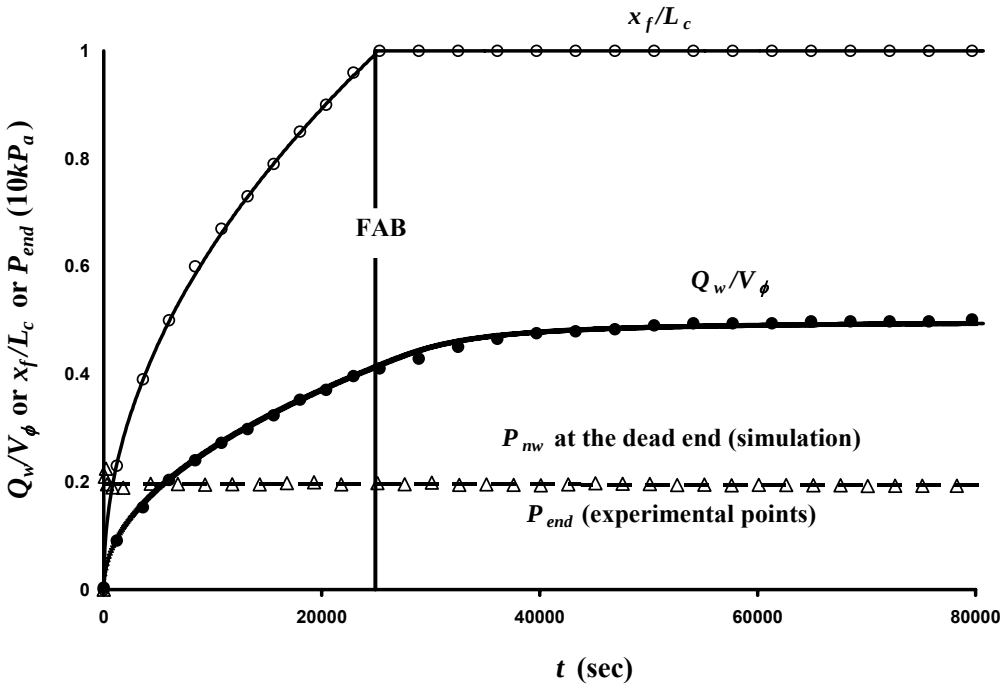

Fig.6. Comparison of experimental and simulated results for imbibition of oil against air (Core H8A). The points (reduced in number from the results presented in Fig.4) are the experimental data; the lines are from simulation.

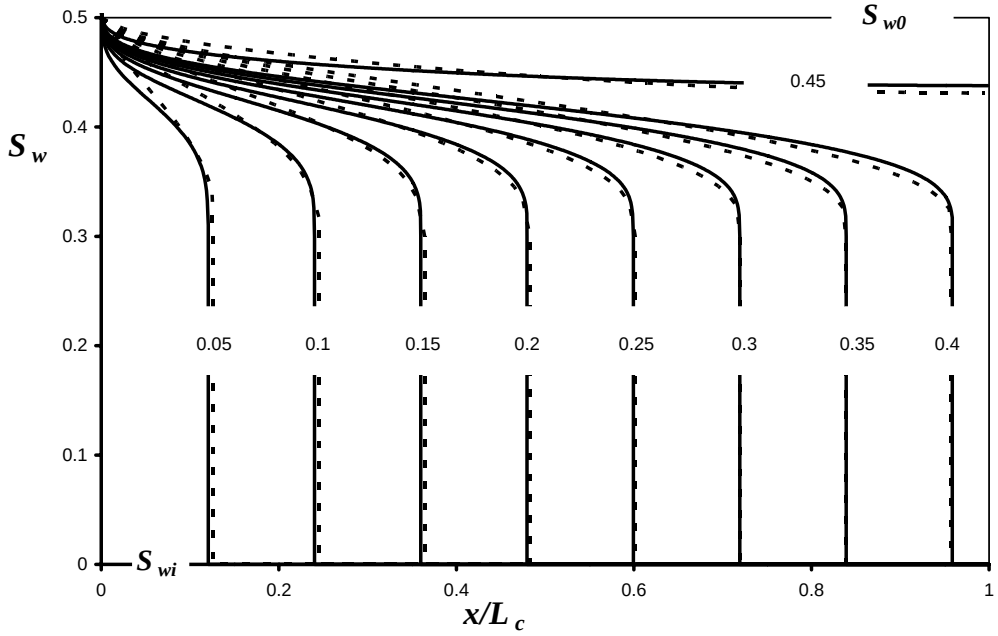

Fig.7 Simulated saturation profiles during water/oil COUCSI for Core H8O (solid lines) and oil/air COUCSI for core H8A (dashed lines). The intervals of the recovery, Q_w/V_ϕ are 0.05.

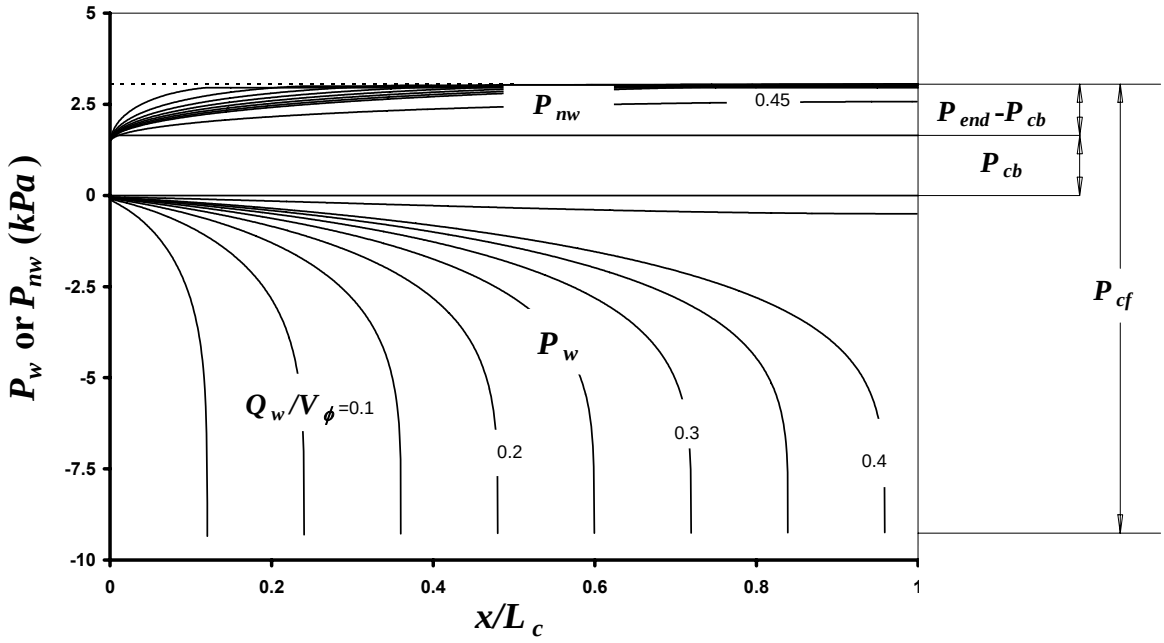

Fig.8 Pressures profiles of WP and NWP during water/oil COUCSI in Core H8O determined by simulation. The maximum difference between P_{nw} and P_w is equal to the capillary pressure, P_{cf}, at the front (the value is 12.359 *kPa*).

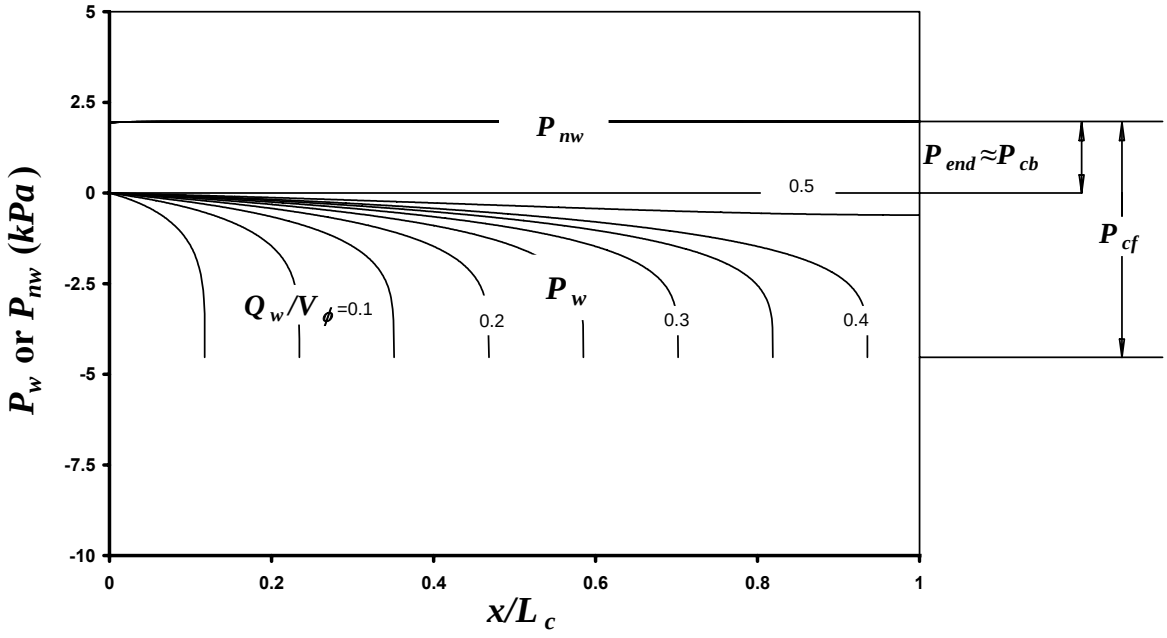

Fig.9 Pressures profiles in WP and NWP during oil/air COUCSI in Core H8A determined by simulation. The maximum difference between P_{nw} and P_w is equal to the capillary pressure at the front, P_{cf}, (the value is 6.500 *kPa*). For oil/air, the difference between the end pressure, P_{end}, and back capillary pressure, P_{cb}, is hard to distinguish at the scale of the diagram.

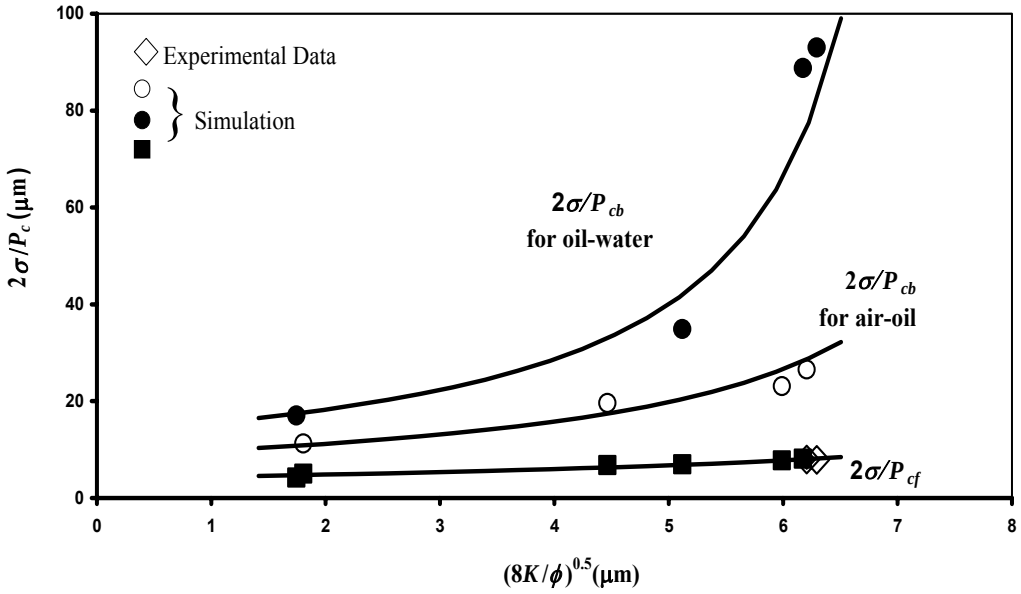

Fig. 10 Relationships between meniscus radii at the front and at the open face compared with the Leverett radius. Solid circles represent the water/oil data ($\sigma_{o\text{-}w}$ = 48.85 *mN/m*) and open circles the oil/air data ($\sigma_{a\text{-}o}$ = 25.87 *mN/m*).

Appendix A

Mathematical model

The basic equations used for deducing the similarity solutions have been given in the simulation method described in Ruth et al [2000].

$$\frac{\partial}{\partial x}\left[\bar{\lambda}\frac{\partial P_c}{\partial x}\right]=\phi\frac{\partial S_w}{\partial t} \qquad \text{A1}$$

where S_w is saturation of wetting phase, P_c is capillary pressure and average mobility, $\bar{\lambda}$, is a function of saturation only and is defined as

$$\bar{\lambda}=\frac{Kk_{rw}k_{rnw}}{\mu_w k_{rnw}+\mu_{nw}k_{rw}} \qquad \text{A2}$$

where K is absolute permeability to air, k_{rw} is relative permeability of wetting phase, k_{rnw} is relative permeability of non-wetting phase and μ_{nw} and μ_w are viscosities of the non-wetting phase and wetting phase respectively.

Note that this equation is not a pair of simultaneous parabolic partial differential equations in unknown pressure in the WP and NW as is usually obtained. Instead it is only one parabolic partial differential equation in known capillary pressure, P_c. A finite difference equation can be derived immediately (Eq. A1).

$$\Delta S_{w(i)}=\frac{1}{V_\phi}[Tr_{(i-1+1/2)}(P_{c(i)}-P_{c(i-1)})-Tr_{(i+1/2)}(P_{c(i+1)}-P_{c(i)})]\Delta t \qquad \text{A3}$$

where i is the ordinal number of the grids, and $Tr_{(i+1/2)}=\frac{A}{2\Delta x}(\bar{\lambda}_{(i)}+\bar{\lambda}_{(i+1)})$ is the mean transmissibility from midpoint weighting. This approximation is of second-order, which helps to produce fast convergence of results (Fig.A1). The more common upsteam weighting is a first-order approximation. Using this weighting, no convergence could be obtained for the water/oil case. Even using a fast personal computer, a single simulation was not found even after many days. The midpoint weighting is used in both water/oil and oil/air simulations, even through the correct simulation results for oil/air cases can be obtained by using upstream weighting. Why upsteam weighting can not produce results in some COUCSI simulations in a timely manner needs to be further explored.

The starting condition for COUCSI is

$$S_w=S_{wi} \qquad \text{A4}$$

for the partial differential equation (Eq.A1), where S_{wi} is the original WP saturation.
in the finite difference equation (Eq.A3)

$$S_{w(i)}=S_{wi(i)} \qquad \text{A5}$$

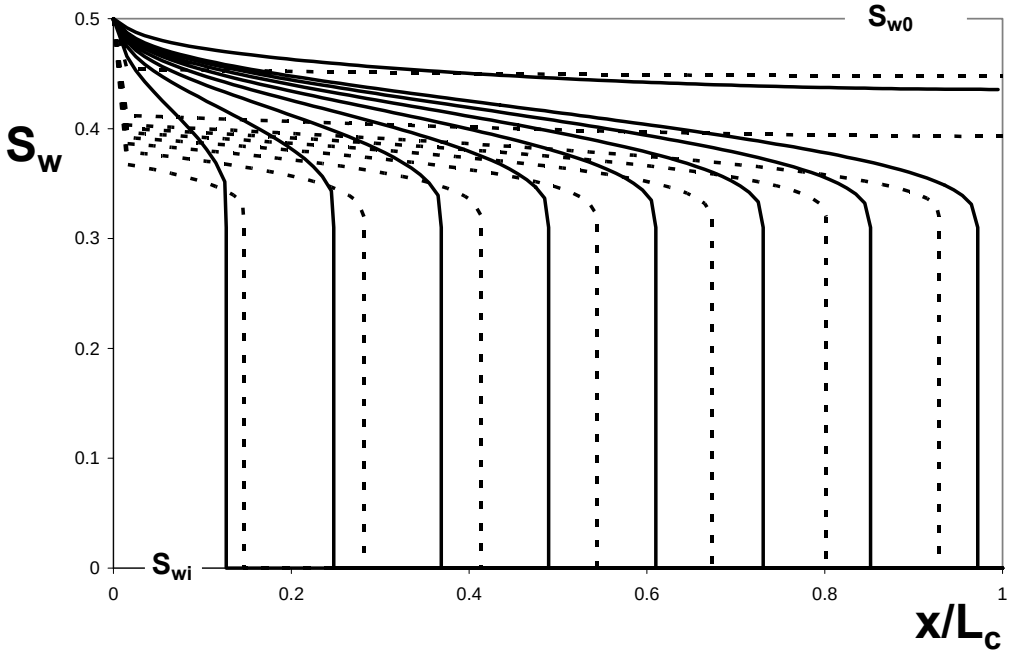

Fig.A1 Comparison of the profiles calculated from the programs based on midpoint weighting (solid lines) and upsteam weighting (broken lines) The results were generated for Δx=100, Δt=0.05. The intervals of recovery, Q_w/V_ϕ, are 0.05.

With the boundary condition for the general COUCSI partial differential equation (Eq.A1) as:

$$P_w = 0 \quad at \quad x = 0 \tag{A6}$$

Also

$$q_w = q_{nw} = 0 \quad at \quad x = L_C \tag{A7}$$

where P_w is the pressure in wetting phase, x is the distance from the open face, L_c is the core length, q_w is the flow rate of wetting phase and q_{nw} is the flow rate of non-wetting phase.

If the number of grid blocks for the core is *N-2* and if Grid *1* is for the *WP* reservoir and Grid *N* is for the grid with a mirror image of the last core grid, Grid *N-1*, the corresponding boundary condition for the above general finite difference equation can be written as

$$S_{w(1)} = S_{w0} \qquad at \quad i = 1 \tag{A8}$$

and

$$S_{w(n)} = S_{w\ (n-1)} \qquad at \quad i = N \tag{A9}$$

where S_{nw0} is the final recovery for COUCSI in the simulation.

Since every parameter or variable is known, the finite difference equation (Eq.A3) is an explicit function, by which the saturation increment for each grid can be calculated for each time step. The numerical simulation will produce a saturation profile varying with time. q_w, q_{nw}, P_w

and P_{nw} need not be calculated directly in the simulation. They can be readily obtained from the saturation profiles in the output file.

To obtain the saturation profile without distortion ('in conditional stability' as described in Aziz, 1979) the time step, Δt, must be less than a limit for a certain division x/L_c. From this study, if x/L_c is fixed and Δt is under the time step limit, the resultant profile will be the same no matter what Δt is used. As is already known (Richtmyer and Morton, 1967), there exists a constant $(x/L_c)\Delta t$, the upper limit for which is the so called 'condition of stability' in the simulation of a given Buckley-Leverett flow. However for our program, it was found that there existed a constant $(x/L_c)^2\Delta t$ for the upper limit (Fig. A2) in COUCSI. Therefore, to obtain a COUCSI result with a high degree of convergence, much more calculation time is required.

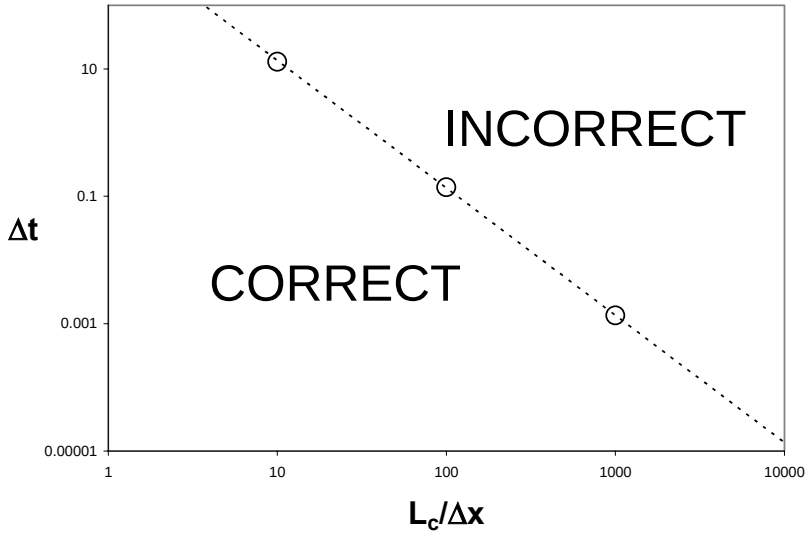

Fig. A2 Condition for the results without distortion in H8O simulation. Points represent the tested critical points. The broken line represents the division between 'correct' and 'incorrect' results for any chosen grid. Correct results do not depend on the size of the time step. 'Incorrect' results vary with the size of the time step.

Appendix B

Construction of P_c/σ and k_{rw}/K_{we} and k_{rnw}/K_{nwe} functions

For the measured relative permeability curves of Berea sandstone [Fulcher, 1985], the relative permeabilities were modeled by,

$$k_{rnw} / K_{nwe} = (k_{rnw0} - k_{rnwf}) \left(\frac{S_{wo} - S_w}{S_{wo} - S_{wf}} \right)^{N_{nw}} + k_{rnwf} \qquad \text{B1}$$

and

$$k_{rw} / K_{we} = (k_{rwf} - k_{rw0}) \left(\frac{S_{wf} - S_w}{S_{w0} - S_{wf}} \right)^{N_w} + k_{rw0} \qquad \text{B2}$$

where K_{we} and K_{nwe} are the effective permeabilities for the WP and the NWP respectively, S_{wf} is the S_w at the front, k_{rwf} is the relative permeability at the front, and k_{rw0} is the relative permeability at the open face.

K_w (brine) is 0.55 times K_g (gas) (Chatzis and Morrow, 1984). The permeability to oil, K_o was 0.8 times K for air (K_{air}) (Fig.B1). The relative permeability for brine, K_w at the residual oil saturation (S_{or}), $K_w(S_{or})$ is 0.0458. In simulation we adopted 0.04 as the value of the brine relative permeability at the open face and 0.0727 for oil.

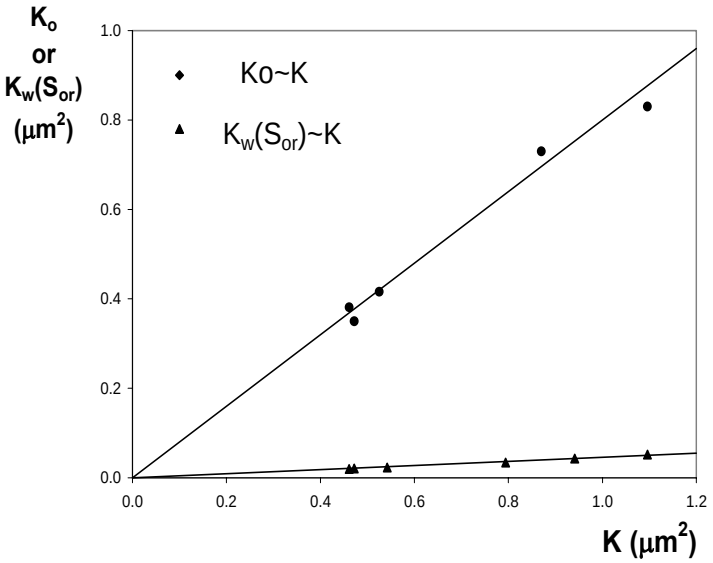

Fig. B1 K_o versus K (gas permeability) and $K_w(S_{or})$ versus K

The imbibition capillary pressure curve for Berea sandstone was assumed to be parabolic in form.

$$P_c = \left(P_{cf} - P_{c0}\right) \left(\frac{S_{wo} - S_w}{S_{wo} - S_{wf}} \right)^{N_{pc}} + P_{c0} \qquad \text{B3}$$

The variables of the curves used for each core are listed in Table 2. Results for Core H8A are plotted in Fig. B2.

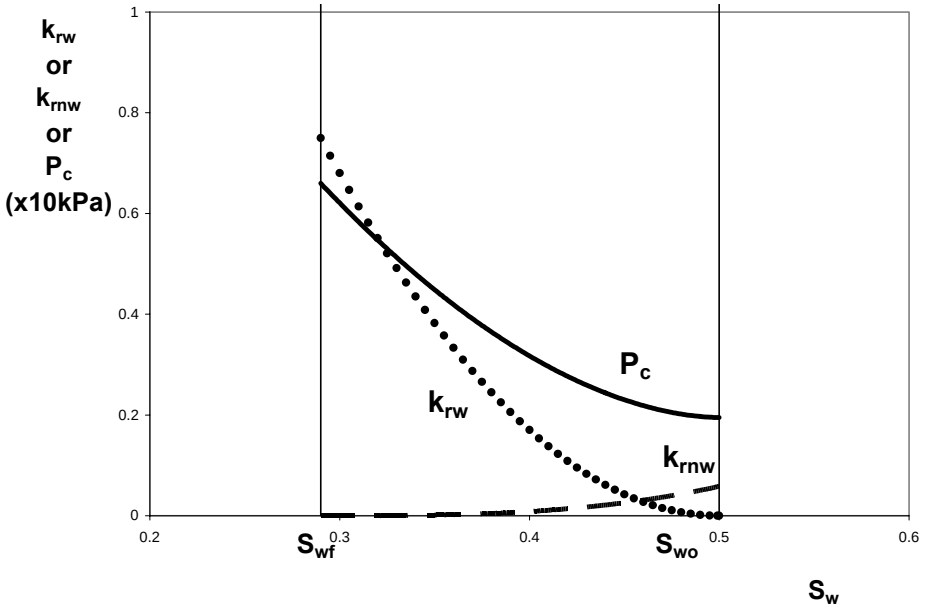

Fig. B2 Relative permeabilities and capillary pressure for Core H8A

Even with constraint on the possible sets of k_{rw}, k_{rnw} and P_c curve shapes, simulations could be performed which provided a close match with the three measured parameters of a COUCSI experiment. Furthermore, a single set of k_{rw}, k_{rnw} and P_c curves can be obtained for both water/oil and oil/air COUCSI experiments with duplicate core samples. A quick search for the appropriate set of k_{rw}, k_{rnw} and P_c curves was performed using the following steps.

a. Fix S_{w0} at the experiment value, fix k_{rw} at S_{w0} as 10^{-10} (using 10^{-10} instead of zero to avoid occurrence of a zero-divide), fix k_{rnw}/K_e at S_{wf} at an arbitrary value, say 0.8 and k_{rw}/K_e at S_{w0} as $0.04/K_e$. Fix N_{nw} at an arbitrary value, say 2 (In the oil/air case the resistance to flow of the NWP is very small). Find appropriate N_{pc} and N_w and S_{wf} values to match the oil/air experiments. (The simulated final saturation can be lower).
b. Increase the simulation S_{w0} to match the final recovery (This procedure will adjust k_{rnw} at the experimental S_{w0} to be finite.).
c. Change N_w and P_{cb} so that the simulation curves match the water/oil performances (P_{nw} at the dead end during the post contact period can be different from P_{end} after WP has arrived at the dead end.)
d. With N_{nw}, N_w and N_{pck} fixed, change P_{cf} and P_{cb} (neither is directly measured) to match the results of the six other experiments of this study.
e. If the P_{cf} points scatter on the P_{cf}~K plot, change k_{rnw} at the S_{wf} (k_{rnw} has been roughly estimated before) to obtain a smoother distribution.

If the post contact performance still has the same positive or negative errors within the comparable stages, use of a multiple-term formula instead of parabolic expressions should be considered. (However, such errors were not found in the present study).

Task 4. *Network/numerical model and new imbibition data.*

(Herbert Fischer and Norman Morrow - in press with *Journal of Petroleum Science & Engineering*)

Abstract

Oil production by spontaneous imbibition can be the key mechanism for oil recovery from naturally fractured reservoirs. Laboratory results of oil recovery through spontaneous imbibition are commonly scaled-up to forecast oil recovery at the reservoir scale. Numerous questions arise with respect to the theory of spontaneous imbibition and valid scaling of laboratory imbibition data.

Use of glycerol as a viscosifying agent for aqueous solutions has many advantages and applications. A systematic study has been made of the physical and interfacial properties of glycerol/water and glycerol/brine (synthetic sea water) solutions. The solutions were used to investigate oil recovery by spontaneous imbibition at very strongly water-wet conditions for aqueous phase viscosities ranging from 1-1650 cP.

Results for aqueous/oleic liquid pairs with matched viscosities were correlated satisfactorily by the Mattax and Kyte scaling group. Data were also obtained for a wide range of unmatched viscosities. Three data sets for unmatched viscosity were obtained with oil viscosity fixed at 4, 22, or 43 cP and aqueous phase viscosity varied from 1 to 1650 cP. Use of the geometric mean viscosity (Ma et al., 1997) in the definition of dimensionless time gave satisfactory correlation of data for brine/oil viscosity ratios of up to about 4. A slight trend of increase in dimensionless time with viscosity ratio within the correlated data became accentuated with increase in viscosity ratio above about four. Residual oil saturation attained by spontaneous imbibition showed an overall small decrease with increase in viscosity of the aqueous phase.

1. Introduction

Oil production from naturally fractured reservoirs often depends on spontaneous imbibition of brine into oil bearing matrix blocks. The rate and extent of recovery depends on both rock and fluid properties and rock/fluid interactions (Zhou et al., 2000; Xie et al., 2000). Oil recovery is often estimated by scaling laboratory imbibition measurements on core plugs to oil production on a reservoir scale. Mattax and Kyte (1962) introduced a scaling group based on the theoretical analysis of Rapoport and Leas (1953) and Rapoport (1954). Six necessary conditions were identified for the scaling group to be applicable, one being that viscosity ratios are identical. Experimental investigation of imbibition for unmatched viscosities with over two orders of magnitude variation in oil phase viscosity showed that results were closely correlated by the geometric mean viscosity of the oleic and aqueous phases (Ma et al., 1997). In the present work, aqueous phase viscosity was varied over three orders of magnitude through use of glycerol as a viscosifying agent. Extensive spontaneous imbibition data sets are reported for both matched and unmatched viscosities.

2. Experimental

2.1. Materials

2.1.1. Liquids

Aqueous Phase. In this study, glycerol ($CH_2OHCHOHCH_2OH$), supplied at 99.5% purity by EMD Chemicals, Inc., was utilized to viscosify the wetting phase. In previous studies, glycerol was used to viscosify the aqueous phase for the purpose of adjusting the oil/aqueous phase viscosity ratio (Leverett et al., 1941; Rapoport and Leas, 1953; Kyte and Rapoport, 1958). None of the reports give detailed information on the physical properties of aqueous glycerol solutions.

Glycerol is a trihydric aliphatic alcohol of great industrial importance (Monick, 1968). It is an odor- and colorless liquid with a molecular weight of 92.09. The density of the supplied glycerol is 1.261 g/cm^3 at 20ºC. One of the pronounced physical properties of glycerol is its viscosity. For glycerol as supplied, the viscosity is 1650 cP at 20ºC and is highly sensitive to temperature. Whereas the viscosity decreases with temperature and the addition of water, electrolytes cause an increase of the viscosity of anhydrous glycerol as well as its aqueous solutions. The refractive index of glycerol at 20ºC is 1.4740. Glycerol boils at 290°C at atmospheric pressure but boiling is accompanied by decomposition. The freezing point of glycerol is about 18°C. In the anhydrous state, glycerol is a highly hygroscopic material. Glycerol is soluble in water in all proportions and insoluble in hydrocarbons. The surface tension is 63.4 dyn/cm at 20ºC, less than the surface tension of water, but higher than the surface tension of most organic liquids. Considerable attention has been given to molecular modeling of the nature of hydrogen bonding in glycerol (Root et al.1997).

In the present work synthetic seawater (Table 1) rather than distilled water was used in preparation of glycerol/brine solutions in order to avoid possible problematic aqueous phase/rock interactions associated with ionic strength. Mixtures of seawater and glycerol were prepared based on constituent weight percent. Ionic strength was not adjusted for the addition of glycerol and so decreased with decrease in water content. Before use in imbibition experiments, the aqueous phase was evacuated for 3 hours to minimize the possibility of the evolution of gas during the imbibition process. Specific aqueous phase properties were measured directly before a spontaneous imbibition test.

Oleic Phase. The oil phase was composed of Soltrol 220® (hereafter described as low viscosity oil, LVO) of 3.9 cP viscosity and 173 cP white mineral oil (hereafter described as high viscosity oil, HVO) (Table 2). Polar contaminants were removed from the mineral oils by contacting the oil with alumina and silica gel either in packed columns (LVO) or by suspension followed by filtration (HVO). Mixtures of the two oils were used to prepare oils of intermediate viscosity. Each mixture was evacuated for about 3 hours to remove any dissolved gas prior to measurement of the physical properties of a specific mixture.

2.1.2. Sandstone

Cylindrical Berea sandstone cores with a nominal diameter, d, of 3.81 cm and a nominal length, l, of 6.35 cm were cut from three different Berea sandstone blocks. The cores were washed, dried at ambient temperature for one day and then oven dried at 105°C for two days. Subsequently, nitrogen gas permeability, k_g, was measured in a Hassler-type core holder at a confining pressure of 300 psi. The permeability to nitrogen ranged from 59 to 85 md. Core porosity was calculated from the increase in mass that resulted from saturation of a core sample with oil. The rock porosity varied from about 16 to 18%. Core properties are provided with the individual data sets. The characteristic length, L_c, for each core for all faces open to imbibition is given by (Zhang et al., 1996)

$$L_c = \frac{ld}{2\sqrt{d^2 + 2l^2}} \tag{1}$$

All cores were cut to nominally the same size and so had essentially the same characteristic length of about 1.24 cm.

2.2 Procedure

2.2.1. Liquid Properties

The density of the liquid mixtures was measured by Paar Density Meter DMA 48 at 20°C. The liquid viscosities were measured with Cannon viscometers. The surface tension of the aqueous phase was measured by the dynamic Wilhelmy plate method (Krüss Processor Tensiometer K12) using a platinum plate. The same equipment was used to determine contact angles on quartz plates. Interfacial tension was obtained with a Krüss Drop Volume Tensiometer DVT-10. Viscosity, surface and interfacial tension, and contact angle were measured at ambient temperature (very close to 20ºC).

2.2.2. Spontaneous Imbibition

In all experiments, the initial water saturation was 0, a condition which has been adopted as a convenient reference starting condition in previous studies (Mattax and Kyte, 1962; Zhang et al., 1996; Ma et al., 1999). The boundary condition for each core was all faces open.

Oil recovery versus time was measured in standard glass imbibition cells at ambient temperature. Results are reported as four experimental data sets. The first set was for matched fluid viscosities ranging from 4 to 172 cP. Three data sets were obtained for unmatched viscosity with each set distinguished by the choice of oil phase viscosity, the values being 4, 22, and 43 cP. Imbibition results for matched viscosity were correlated by the scaling group proposed by Mattax and Kyte,

$$t_{D,MK} = t\sqrt{\frac{k}{\phi}}\frac{\sigma}{\mu_w}\frac{1}{L^2} \tag{2}$$

Results for the unmatched viscosity were correlated by the modified Ma et al. scaling group

$$t_D = t\sqrt{\frac{k}{\phi}}\frac{\sigma}{\mu_g}\frac{1}{L_c^2}$$

(3)

where $\mu_g = \sqrt{\mu_w \mu_o}$ is the geometric mean viscosity.

3. RESULTS & DISCUSSION

3.1. Properties of Brine/Glycerol Solutions

Density. Measured densities of glycerol/synthetic seawater along with reported densities (CRC Handbook, 1976-7) for distilled water/glycerol mixtures are shown in Fig. 1. For both distilled water and brine there is no significant volume change of mixing with glycerol. The aqueous phase density increases linearly with increase in glycerol concentration from 1.0238 g/cm^3 for seawater to 1.2616 g/cm^3 for glycerol.

For aqueous phase prepared with seawater, the density can be fitted by

$$\rho_{ap} = 0.0024 C_{gl} + 1.024 \tag{4}$$

For distilled water the aqueous phase density is closely approximated by

$$\rho_{ap} = 0.0027 C_{gl} + 0.995 \tag{5}$$

Viscosity. The viscosities of glycerol/brine mixtures and literature values for glycerol/distilled water are shown in Fig. 2 as a semilog plot. The viscosity of glycerol (described as > 99.5% purity) at ambient temperature is 1647 cP. However, addition of a small volume of water causes enormous reduction in aqueous phase viscosity. For example addition of 3 wt % water halves the viscosity of glycerol. At 18 wt % water, the mixture viscosity is about 100 cP.

The measured viscosity data for glycerol/brine lay on a smooth curve that was matched almost precisely by a modified expression for the viscosity of dispersions of spherical particles (van de Ven, 1989). The glycerol concentration in the mixture, C_{gl}, is expressed as a weight fraction.

$$\mu_{ap} = \mu_w \left[\frac{1 - C_{gl}/1.9}{1 - 1.451(C_{gl}/1.9)} \right]^{10.53} \tag{6}$$

Detailed discussion of the choice of parameters and their physical significance is beyond the scope of this paper. Literature results for distilled glycerol/water are also closely fitted by equation (7)

$$\mu_{ap} = \mu_w \left[\frac{1 - C_{gl}/1.9}{1 - 1.537(C_{gl}/1.9)} \right]^{8.85} \tag{7}$$

The viscosity for pure glycerol is specified as 1759.6 cP (CRC Handbook, 1976-7). In this study a viscosity of 1646.6 cP was measured for the as-supplied glycerol. Because of the extreme sensitivity of viscosity to very low water content, these differences have little effect on the overall match provided by equations (6) and (7).

Surface Tension. Decrease in surface tension of the aqueous phase with increase in glycerol concentration is very close to linear (Fig. 3). This indicates that there is no preferential adsorption of either water or glycerol at the interface. The results were closely fitted by

$$\sigma_{ap/air} = 72.81 - 0.09 C_{gl} \qquad (8)$$

Interfacial tension (IFT). The values for brine/HVO and brine/LVO interfacial tension are shown in Fig. 4. IFT decreases close-to-linearly with increase of the glycerol concentration for both oils. The IFTs for pure seawater and HVO were 51.3 dynes/cm and 29.4 dynes/cm for glycerol and HVO. All data were closely fitted by

$$\sigma_{ap/HVO} = 51.29 - 0.218 C_{gl} \qquad (9)$$

For pure seawater/LVO the IFT was 50.4 dynes/cm and 27.6 dynes/cm for LVO against glycerol. The IFT data show very little scatter. Values for mixtures were closely fitted by

$$\sigma_{ap/LVO} = 49.48 - 0.218 C_{gl} \qquad (10)$$

Contact angle. Contact angles, from force-distance measurements on quartz plates, were zero (see Figs. 3, 4) for glycerol/sea water mixtures against n-decane or air. Perfect wetting was confirmed by the mirror-like appearance of the plates in reflected light (Menella et al., 1995). A working assumption was therefore made that Berea sandstone was also very strongly water wet for all imbibition tests.

3.2. Spontaneous Imbibition

3.2.1. Matched Viscosities

The scaling equation of Mattax and Kyte was proposed for the special case of matched viscosities. In the present work the equation was tested for a constant viscosity ratio very close to unity for a wide range of matched viscosities. The viscosity ratio, Ψ, is defined by

$$\Psi = \mu_{ap} / \mu_o \qquad (11)$$

Table 3 lists the core and liquid properties used in imbibition tests performed with closely matched oleic and aqueous phase viscosities.

Relationships between oil recovery and imbibition time are presented in Fig. 5. The rate of oil recovery decreases systematically as viscosity increases (Fig. 5a). The Mattax and Kyte scaling group gave close correlation of results over the entire viscosity range (Fig. 5b). Correlated oil recovery curves all had the same shape and there was no distinct trend with respect to absolute values of viscosity. In general, final oil recovery showed slight overall increase with viscosity ratio. However, all data points except one fell within 52% ± 1 (Fig. 5c).

The dependency of the imbibition time for specific fractions of normalized final recovery for the nine matched viscosity experiments is depicted in Fig. 6a. The curves become increasingly close to parallel alignment with increase in recovery. The dimensionless times for a specific recovery fall close to horizontal straight lines that correspond to perfect correlation (Fig. 6b).

3.2.2. Non-matched (NM) Viscosities

Spontaneous imbibition is a complex process. As yet, there is no published theory for correlation of data sets for which the viscosity ratio is a variable; results obtained by simulation have been reported (Ruth et al., 2000). Experimental results for imbibition of water for oil viscosities ranging from about 1 to 160 cP were closely correlated by the geometric mean of the oil and water viscosity (Zhang et al., 1996). In the present work, this empirical correlation has been tested for a wide range of variation in the aqueous phase viscosity for oil viscosities of 4, 22, and 43 cP.

Set NM(4): μ_o= 4 cP. Core and fluid properties are listed in Table 4. The aqueous phase viscosity for these spontaneous imbibition experiments covers the entire range from 1.1 cP for seawater to 1646.6 cP for glycerol.

The imbibition curves for recovery of 4 cP oil for different aqueous phase viscosities are shown in Fig. 7a. The rates of recovery decreased systematically by over 2½ orders of magnitude with increase in aqueous phase viscosity. The data were closely correlated by plots of oil recovery versus dimensionless time, t_D, (see Fig. 7b). However the slopes of the scaled curves decreased slightly with increase in aqueous phase viscosity and also show a small but systematic increase in t_D with increase in aqueous phase viscosity. Final oil recoveries tended to increase with viscosity ratio, apart from a plateau in the viscosity ratio range of 4 to 60 (see Fig.7c).

The trends shown in Fig. 7 may be related to subtle changes in the displacement mechanism. The increase in displacement efficiency with viscosity ratio (Fig. 7c) may be related to the improved mobility ratio or perhaps to the effect of the aqueous phase on the microscopic mechanism of displacement whereby snap-off is retarded by the viscosity of the aqueous phase. In comparable studies of recovery of refined oil by imbibition of brine, final oil recovery was independent of oil viscosity for values ranging from 1 to 160 cP (Zhang et al., 1994).

Log-log plots of imbibition time versus viscosity ratio for specific normalized oil recoveries show close to parallel alignment (Fig. 8a). This kind of plot relates the time needed to recover a certain percentage of the total recoverable oil for a given viscosity ratio. Times for 100% (i.e. final) recovery are not identified because the recovery curves at late time are essentially asymptotic. The variation in t_D versus viscosity ratio, for different levels of recovery,

illustrates the closeness to perfect scaling given by the geometric mean viscosity (Fig. 8b). Overall there is a tendency for t_D to increase with viscosity ratio.

Set NM(22): μ_o= 22 cP. The properties of the cores and liquids utilized to obtain the data set for 22 cP mineral oil are presented in Table 5. Cores cut from the same block of sandstone had permeability and porosity that was consistently of about 67 md and 17% respectively. One core, C5-19, cut from a different Berea sandstone block, had somewhat higher than average permeability and porosity.

Imbibition results are displayed in Fig. 9. For viscosity ratios up to 4, results were closely correlated, with slight, but systematic, increase in dimensionless time with increase in aqueous phase viscosity. For higher viscosities, there was a distinct increase in dimensionless time for imbibition with increase in μ_{ap} and stretching of the curves at later recovery times.

As for the NM(4) set, oil recovery increased from about 50 to 53% with increase in viscosity ratio for viscosity ratios of up to about 4; above 4, the final recoveries were 53% ± ½ (Fig. 9c).

Log-log plots of t versus viscosity ratio for different normalized oil recovery factors give close to parallel relationships (Fig. 10a). The graphs of t_D versus viscosity ratio in Fig. 10b are all close to horizontal up to a viscosity ratio of around 4. For viscosity ratios higher than 4, the dimensionless times for a specific recovery show distinct increase with increase in Ψ.

Set NM(43): μ_o= 43 cP. Table 6 lists the core and fluid properties for the data set obtained for recovery of 43 cP oil. Of the 9 cores, C5-21 and C5-17 were cut from the aforementioned higher permeability Berea sandstone block.

Results for Set NM(43), except for core C5-17 being somewhat out of sequence, showed comparable characteristics to those of data set NM(22) (Fig. 11a). Imbibition curves were closely correlated for the lower μ_{ap} tests (up to 99.9 cP) but as for Set NM(4) and Set NM(22), there was still a slight systematic increase in t_D with μ_{ap} (see Fig. 11b). At higher μ_{ap} the dimensionless times increased as μ_{ap} increased, and as for data set NM(22) became stretched with increase in recovery. As for Sets NM(4) and NM(22), the final oil recovery factor increased slightly with increase in viscosity ratio up to a viscosity ratio of about 4. At higher viscosity ratio, the residual oil was close to constant at 52.5% ± ½ (Fig. 11c).

Plots of time versus viscosity ratio with normalized recovery as parameter are shown in Fig. 12a. Relationships between dimensionless time and viscosity ratio (Fig. 12b) are closely comparable to those given by Set NM(22). Again, the recovery curves show only slight increase in t_D with increase in Ψ up to 4 and marked systematic increase at higher values of viscosity ratio.

3.3. Comparison of all final oil recoveries and imbibition plots

Final oil recovery versus viscosity ratio (Fig. 13a) for all matched and unmatched viscosity data exhibit an overall trend of increase in recovery at lower viscosity ratios. Beyond a viscosity ratio of 4, the final oil recoveries reach a plateau at about 52.5% final oil recovery.

Final recoveries for matched viscosities fit an overall trend when all final recovery data are plotted against aqueous phase viscosity (Fig. 13b).

Inspection of data sets NM(4), NM(22) and NM(43) show that close correlation of imbibition data is obtained if the aqueous phase viscosity is no more than about 4 times greater than the oil viscosity. Plots of recovery versus t_D are shown in Fig. 14 for all three NM sets together with a best fit to the correlated data for matched viscosity.

Averaged imbibition curves for both the matched and unmatched viscosity data up to a viscosity ratio of 4 are presented in Fig. 15. The averaged recovery curves, presented in Fig. 15, show very close agreement for NM(22), NM(43), and the matched viscosity data. The lower viscosity oil exhibits slightly longer dimensionless times for recovery. Overall the recovery curves are close to a correlation established for very strongly water wet Berea 500 (permeability to nitrogen 500 md) at early time and to VSWW Berea 90 (permeability to nitrogen 90 md) at late time. Previous studies have shown variation in the location of the scaled imbibition curves for Berea sandstone of about 90 md permeability (Tong et al., 2001).

Results for the non-matched data sets NM(4), NM(22) and NM(43) obtained for viscosity ratios in the range of 0.25 to 74 are plotted in Fig. 16 as t_D versus viscosity ratio for recoveries of 20%, 50%, 80% and 98% of original oil in place. Overall there is slight increase in t_D for Ψ up to 4. Above 4 there is a more marked overall increase in t_D which is well illustrated by the results for Set NM(22) and Set NM(43) (see Fig. 10b and Fig. 12b respectively).

(a) 3.4. Modification of the scaling equation

The systematic increase in dimensionless time with viscosity ratio for the non-matched viscosity data sets NM(4), NM(22) and NM(43) shows that empirical correlation of these data sets can be improved. The common range of viscosity ratios for all three data sets lies between 0.3 and 38. The curves for fractional recoveries of 50% and higher in Fig. 16 are characterized by near parallel slopes on a log-log scale. Average curves were determined for recoveries of 40, 50, 60, 70, 80, and 90%. The average curves were then normalized with respect to the dimensionless time at a viscosity ratio of 1 for each specific level of oil recovery. (No systematic trends were observed for the matched viscosity data (Fig. 6b)). From the six resulting normalized curves, an average curve was evaluated which represents the overall dependence of the average normalized dimensionless time on the viscosity ratio expressed as the viscosity ratio factor, $f(\Psi)$. The dimensionless time (Ma et al., 1997) is then divided by $f(\Psi)$ to obtain a modified dimensionless time, t_{DM}. The dependence of the viscosity ratio factor on the viscosity ratio over the range of 0.3 to 40 was fitted by two functions, one for the viscosity ratio range of 0.3 to 14 and the other for a viscosity ratio range of 14 to 40:

(b) For $\Psi \leq 14$,

$$f_1(\Psi) = 1.122 \ln \Psi - 0.794 \quad \text{and} \quad (12)$$

$$t_{DM} = t_D / f_1(\Psi) \quad (13)$$

(c) For $14 < \Psi < 40$,

$$f_2(\Psi) = -0.007\Psi^2 + 0.203\Psi + 0.759 \quad \text{and} \quad (14)$$

$$t_{DM} = t_D / f_2(\Psi) \quad (15)$$

The viscosity ratio factors, $f(\Psi)$, given by these two functions, are shown graphically in Fig. 17.

The adjusted results are shown in Fig. 18 as normalized oil recovery versus modified dimensionless time, t_{DM}, for NM(4) (Fig. 18a) for viscosity ratios for up to 25, and NM(22) (Fig. 18b), and NM(43) (Fig. 18c). (For Set NM(22), $f_2(\Psi)$ derived from the experimental data was extrapolated to the viscosity ratio of 74 in order to include all of the Set NM(22) data.) Significant improvement of the correlation was achieved.

Fig. 19 shows the average imbibition curves obtained from the correlation given by the modified scaling equation for both the matched and unmatched viscosity data. The improvement of the correlation is demonstrated by the even closer agreement of all four curves when compared with Fig.15, for which only viscosity ratios of up to 4 were taken into account.

4. Conclusions

- Glycerol serves as a near-ideal aqueous phase viscosifying agent. Density, surface tension and interfacial tension were linearly dependent on concentration. All glycerol/water mixtures exhibited zero contact angle (spreading) against both air and n-decane on quartz surfaces. Increase in viscosity with glycerol concentration was highly non linear. Small consistent shifts in physical properties were observed between glycerol/distilled water and glycerol/sea water mixtures.

- Imbibition data obtained for matched viscosities (the special case of constant viscosity ratio of unity) were correlated satisfactorily by the Mattax and Kyte scaling group. Final oil saturations increased only slightly with increase in matched viscosity.

- Rate of spontaneous imbibition decreased and oil recovery increased slightly with increase in aqueous phase viscosity.

- Imbibition results for viscosity ratios of less than 4 were closely correlated by the Ma et al. scaling group with only very small but systematic dependence of dimensionless time on viscosity ratio. However, final oil recovery for unmatched liquid viscosities increased slightly with increase in aqueous phase/oil viscosity ratio up to about 4. Increase in dimensionless time for imbibition with viscosity ratio was observed for viscosity ratios greater than 4 but final oil recoveries were close to constant.

- Improved correlation of imbibition data was obtained by compensating the geometric mean of the viscosities for an overall systematic increase in dimensionless time for recovery.

Table 1
Synthetic Seawater
Composition and Properties

ρ_w= 1.0238 (g/cm^3), μ_w= 1.1 (cP)		
NaCl	28.0000	(g/L)
KCl	0.9350	(g/L)
$MgCl_2$	5.3625	(g/L)
$CaCl_2$	1.1900	(g/L)
NaN_3	0.1000	(g/L)
TDS	35.5875	(g/L)

Table 2
Mineral Oil Properties

	LVO	HVO
Density ρ, (g/cm^3)	0.782	0.872
Viscosity μ, (cP)	3.9	173.0

Table 3
Rock and Fluid Properties, Matched Viscosities

Core #	L_c (cm)	k_g (md)	Φ (%)	σ_{ow} (dyn/cm)	ρ_{ap} (g/cm^3)	ρ_o (g/cm^3)	μ_{ap} (cP)	μ_o (cP)	μ_g (cP)
C1-20	1.239	71.2	17.4	40.2	1.119	0.782	4.3	4.0	4.1
C1-24	1.240	59.7	17.4	36.8	1.170	0.817	13.6	13.6	13.6
C1-21	1.238	72.2	17.5	34.4	1.185	0.828	20.9	20.9	20.9
C1-19	1.237	69.9	17.5	33.3	1.204	0.843	43.9	44.1	44.0
C1-23	1.244	66.5	17.7	32.0	1.213	0.851	59.3	59.3	59.2
C1-22	1.236	69.7	17.9	31.8	1.220	0.858	80.2	80.1	80.1
C3-30	1.238	63.1	17.1	30.5	1.226	0.863	99.7	99.1	99.4
C5-4	1.230	69.6	17.4	30.1	1.231	0.869	140.0	141.7	140.8
C3-34	1.242	75.8	17.7	30.3	1.235	0.873	171.2	173.0	172.1

Table 4
Rock and Aqueous Phase Properties
NM(4): μ_o= 4 (cP), ρ_o= 0.782 (g/cm^3)

Core #	L_C (cm)	k_g (md)	Φ (%)	σ_{ow} (dyn/cm)	ρ_{ap} (g/cm^3)	μ_{ap} (cP)
C3-1	1.247	63.5	16.9	48.9	1.026	1.1
C1-1	1.242	62.3	16.9	39.8	1.121	4.4
C3-9	1.242	70.5	16.9	37.6	1.152	8.7
C1-2	1.230	64.5	16.9	35.3	1.172	15.2
C3-6	1.241	66.7	17.0	34.4	1.186	21.8
C3-8	1.241	62.7	17.0	32.9	1.200	39.5
C3-7	1.237	64.5	16.9	32.1	1.211	59.4
C1-3	1.242	62.7	16.8	31.2	1.222	99.8
C1-16	1.237	69.9	17.3	30.6	1.243	185.0
C1-20	1.239	71.2	16.8	28.3	1.255	826.9
C1-25	1.238	71.5	17.4	27.7	1.262	1646.6

Table 5
Rock and Aqueous Phase Properties
NM(22): μ_o= 22 (cP), ρ_o= 0.828 (g/cm^3)

Core #	L_c (cm)	k_g (md)	Φ (%)	σ_{ow} (dyn/cm)	ρ_{ap} (g/cm^3)	μ_{ap} (cP)
C1-7	1.238	65.1	17.0	52.4	1.024	1.1
C1-9	1.242	65.4	17.0	41.2	1.121	4.4
C1-10	1.240	68.8	16.8	37.3	1.152	8.7
C1-8	1.239	69.7	17.1	35.9	1.172	15.2
C1-6	1.241	65.5	17.0	34.5	1.185	22.0
C1-4	1.238	66.1	16.9	33.1	1.201	39.6
C1-5	1.239	68.0	16.9	32.5	1.222	96.6
C1-22	1.236	69.7	16.0	30.8	1.237	228.4
C5-19	1.227	85.7	17.9	29.5	1.249	522.7
C1-26	1.219	67.8	17.4	28.6	1.261	1646.6

Table 6
Rock and Aqueous Phase Properties
NM(43): μ_o= 43 (cP), ρ_o= 0.843 (g/cm^3)

Core #	L_c (cm)	k_g (md)	Φ (%)	σ_{ow} (dyn/cm)	ρ_{ap} (g/cm^3)	μ_{ap} (cP)
C1-11	1.237	68.7	17.1	53.1	1.024	1.1
C1-12	1.242	62.5	17.2	41.7	1.121	4.4
C1-13	1.238	55.6	16.7	36.4	1.172	15.2
C1-15	1.241	70.4	17.2	34.6	1.197	35.4
C1-14	1.240	70.0	17.2	32.4	1.220	96.6
C5-21	1.234	82.0	18.2	31.9	1.222	99.9
C1-19	1.237	69.9	16.8	31.1	1.237	228.4
C5-17	1.236	77.2	18.0	29.6	1.249	522.7
C1-18	1.236	67.4	16.2	28.5	1.262	1646.6

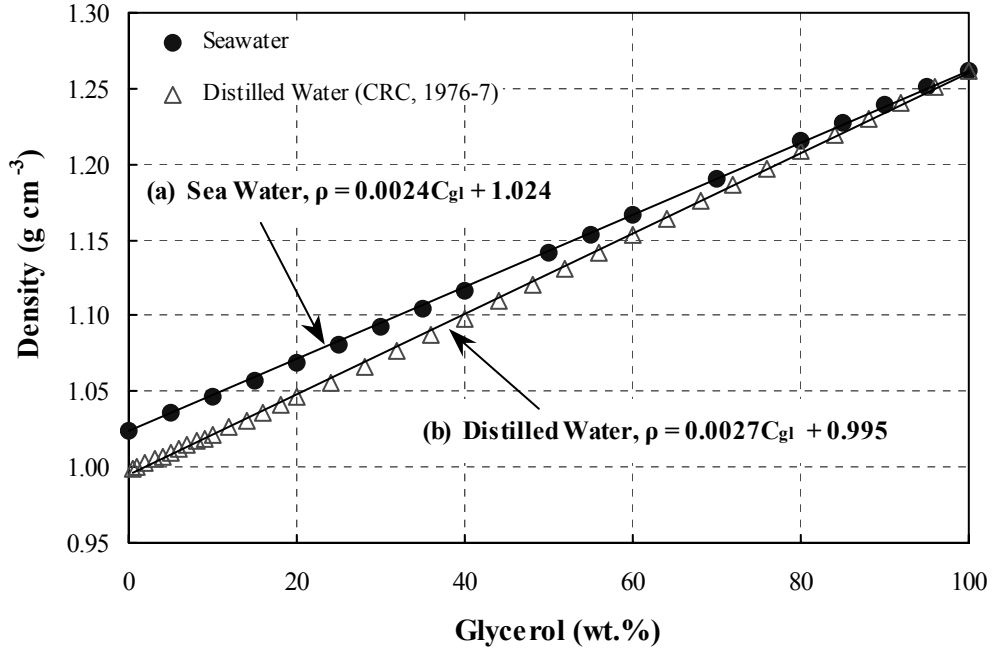

Fig. 1. Aqueous phase density of (a) glycerol/sea water and (b) glycerol/distilled water.

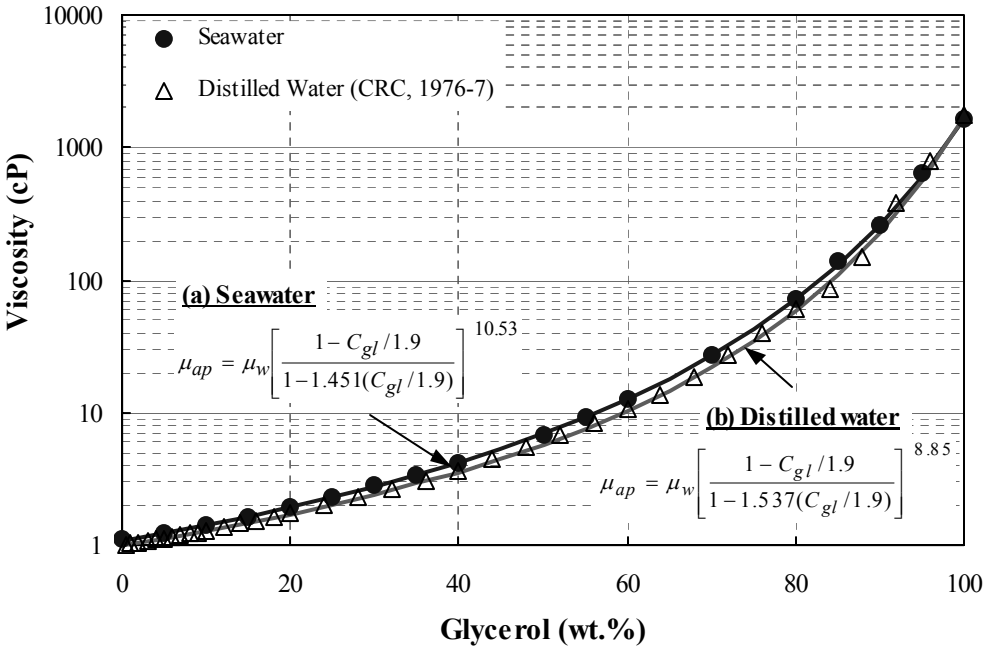

Fig. 2. Aqueous phase viscosity of (a) glycerol/brine and (b) glycerol/distilled water.

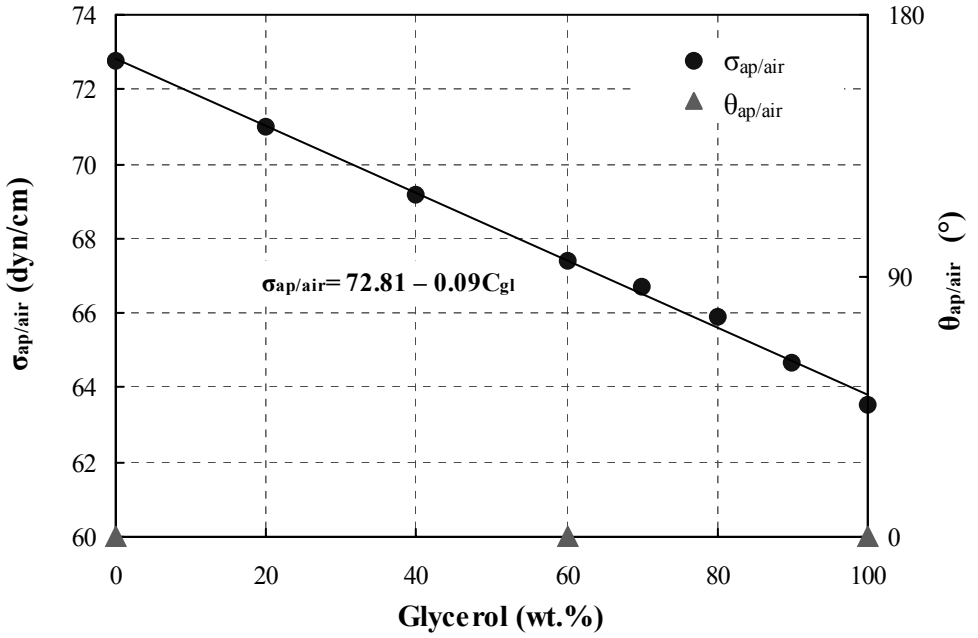

Fig. 3. Aqueous phase surface tensions and contact angles of glycerol/brine against air.

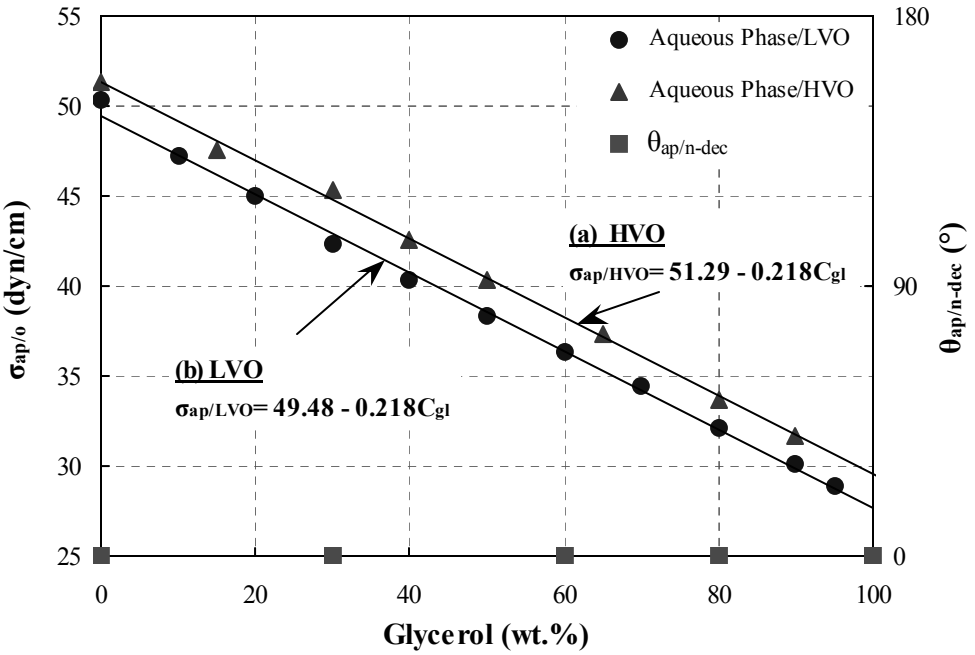

Fig. 4. Contact angle against quartz (aqueous phase/decane) and interfacial tensions of aqueous phase against: (a) high viscosity oil, μ (HVO) = 173 cP and (b) low viscosity oil, μ (LVO) = 4 cP.

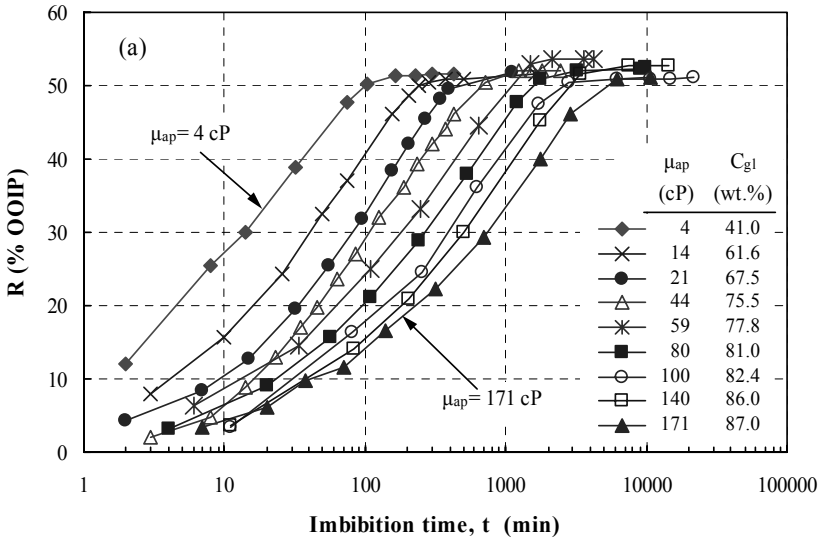

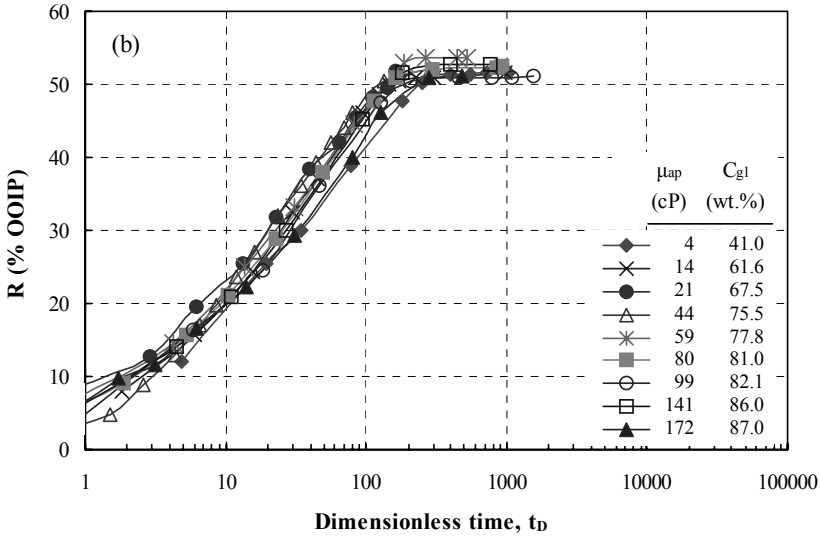

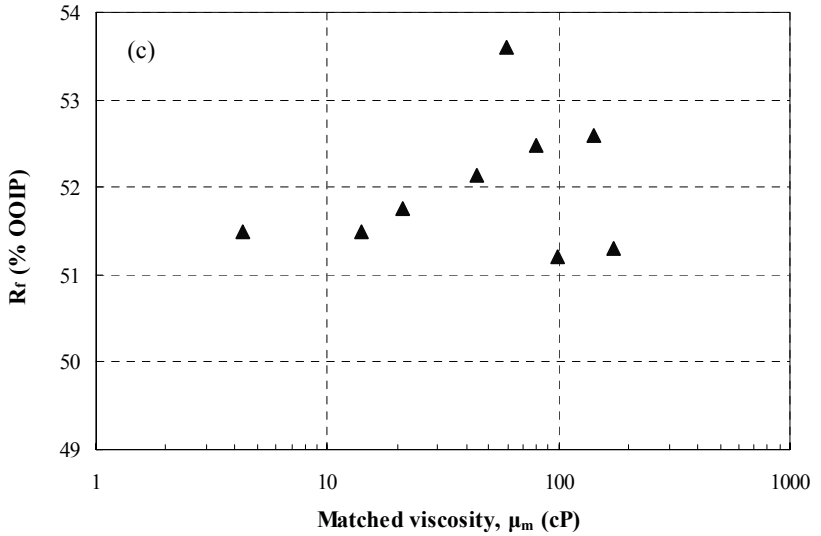

Fig. 5 Recovery of oil by spontaneous imbibition for matched phase viscosity versus (a) time and (b) dimensionless time; (c) final oil recovery, R_f, versus viscosity

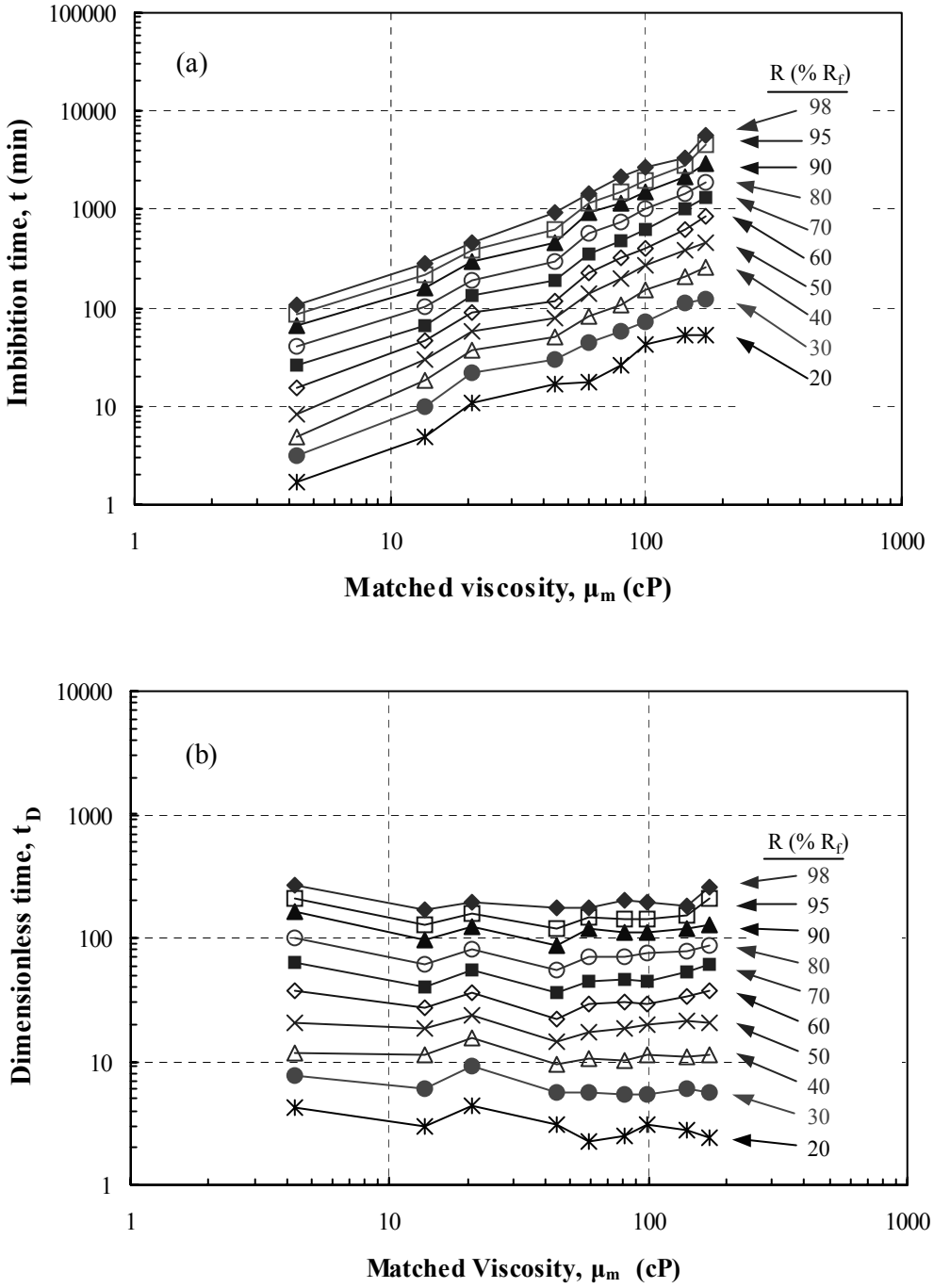

Fig. 6. Imbibition time (a) and scaled time (b) versus matched viscosity for fractional recoveries, *R*, ranging from 20% to 98% (interpolated values for individual cores).

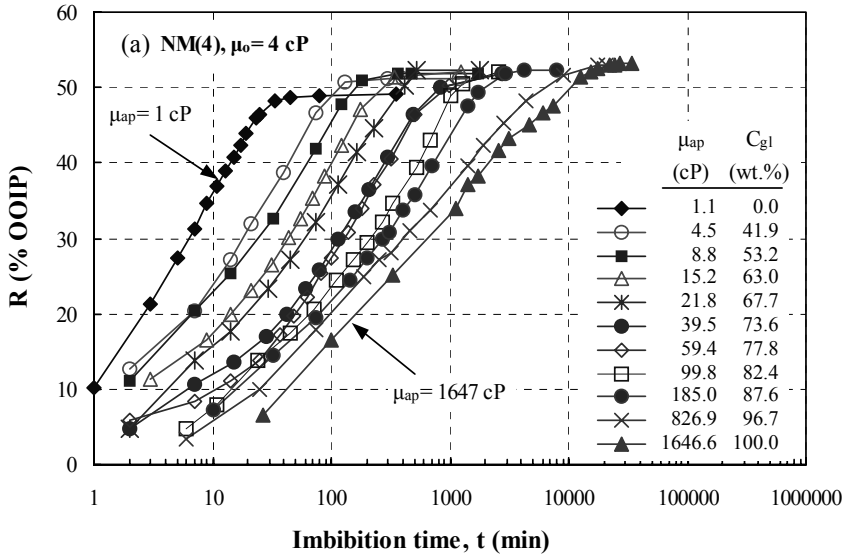

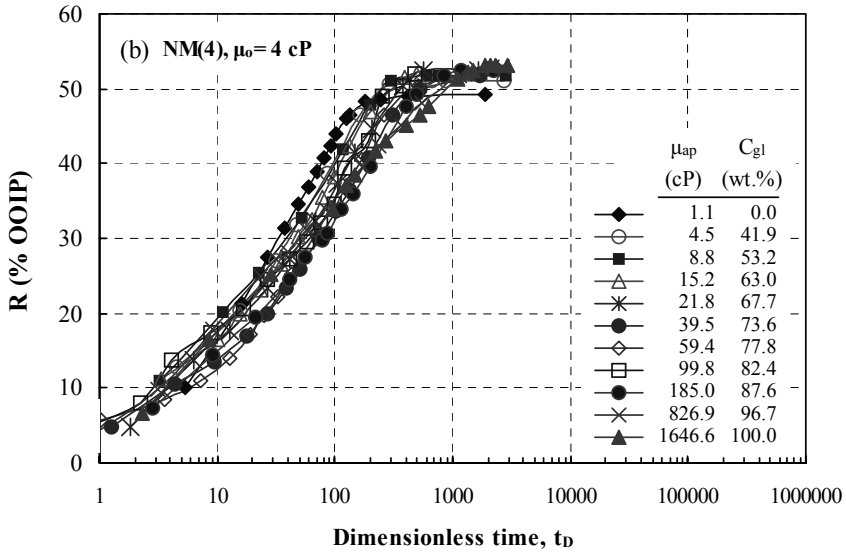

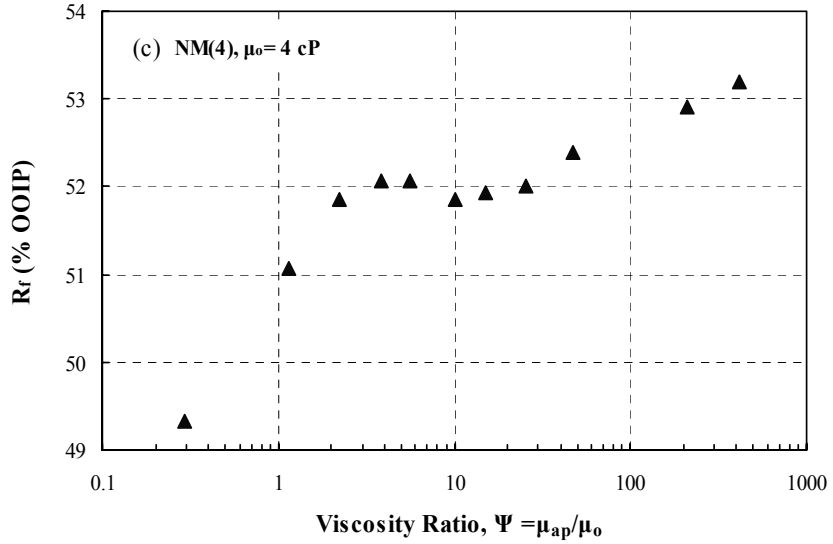

Fig. 7. Recovery of 4 cP oil by spontaneous imbibition for variation in aqueous phase viscosity versus (a) time and (b) dimensionless time; (c) final oil recovery, *Rf*, versus viscosity ratio.

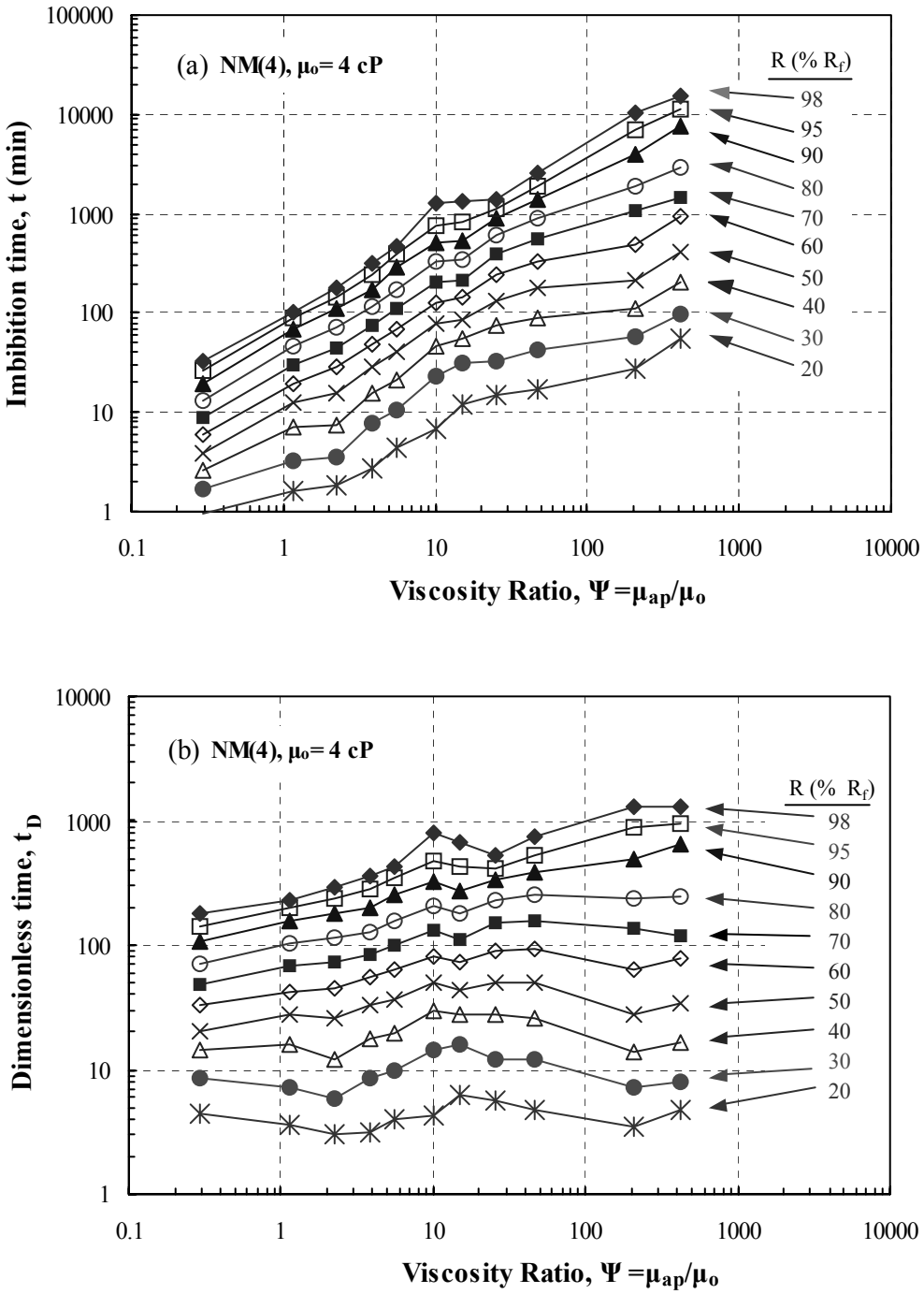

Fig. 8. Imbibition time (a) and dimensionless time (b) versus viscosity ratio (μ_o = 4 cP) for fractional recoveries, *R*, ranging from 20% to 98% (interpolated values for individual cores).

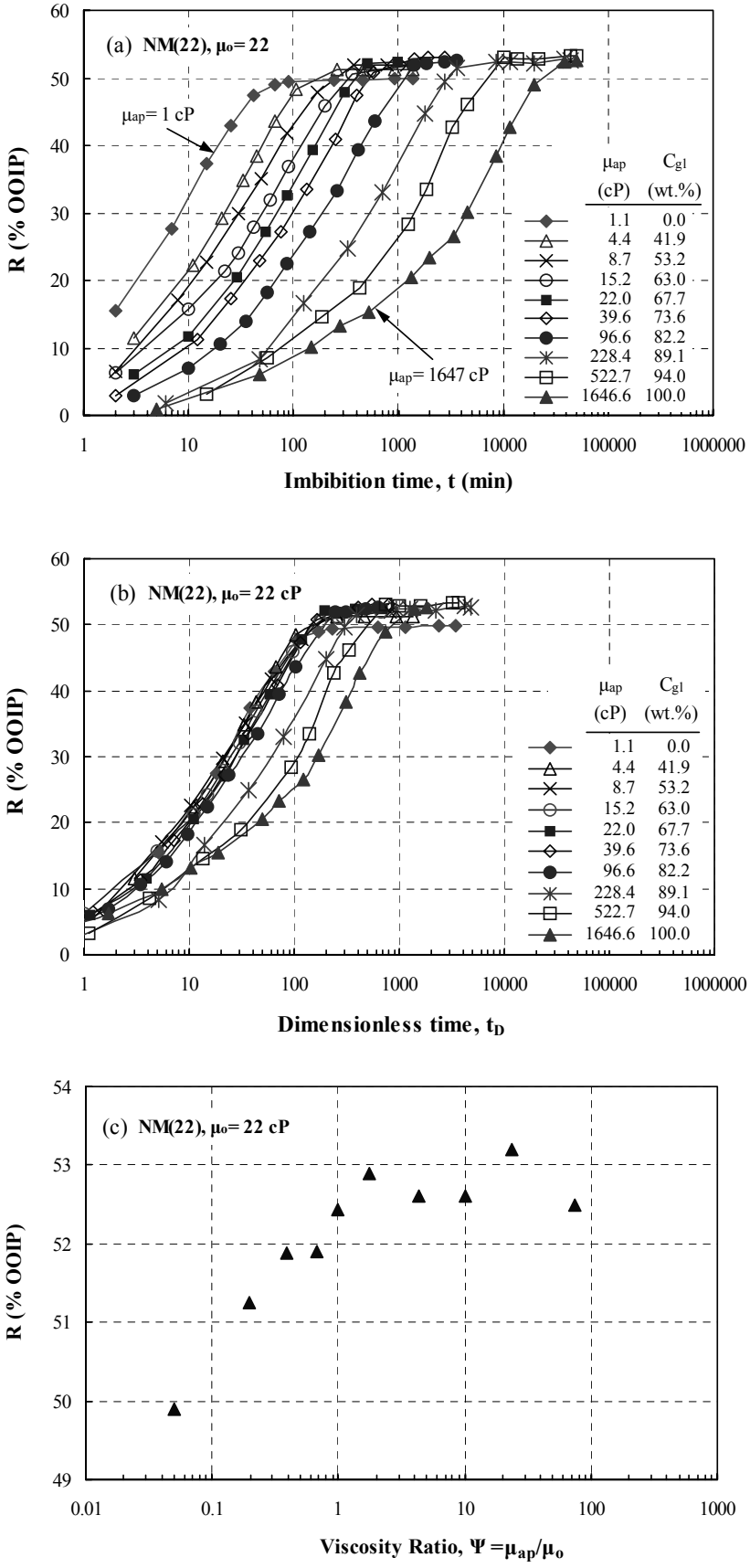

Fig. 9. Recovery of 22 cP oil by spontaneous imbibition for variation in aqueous phase viscosity versus (a) time (b) dimensionless time; (c) final oil recovery, *Rf*, versus viscosity ratio.

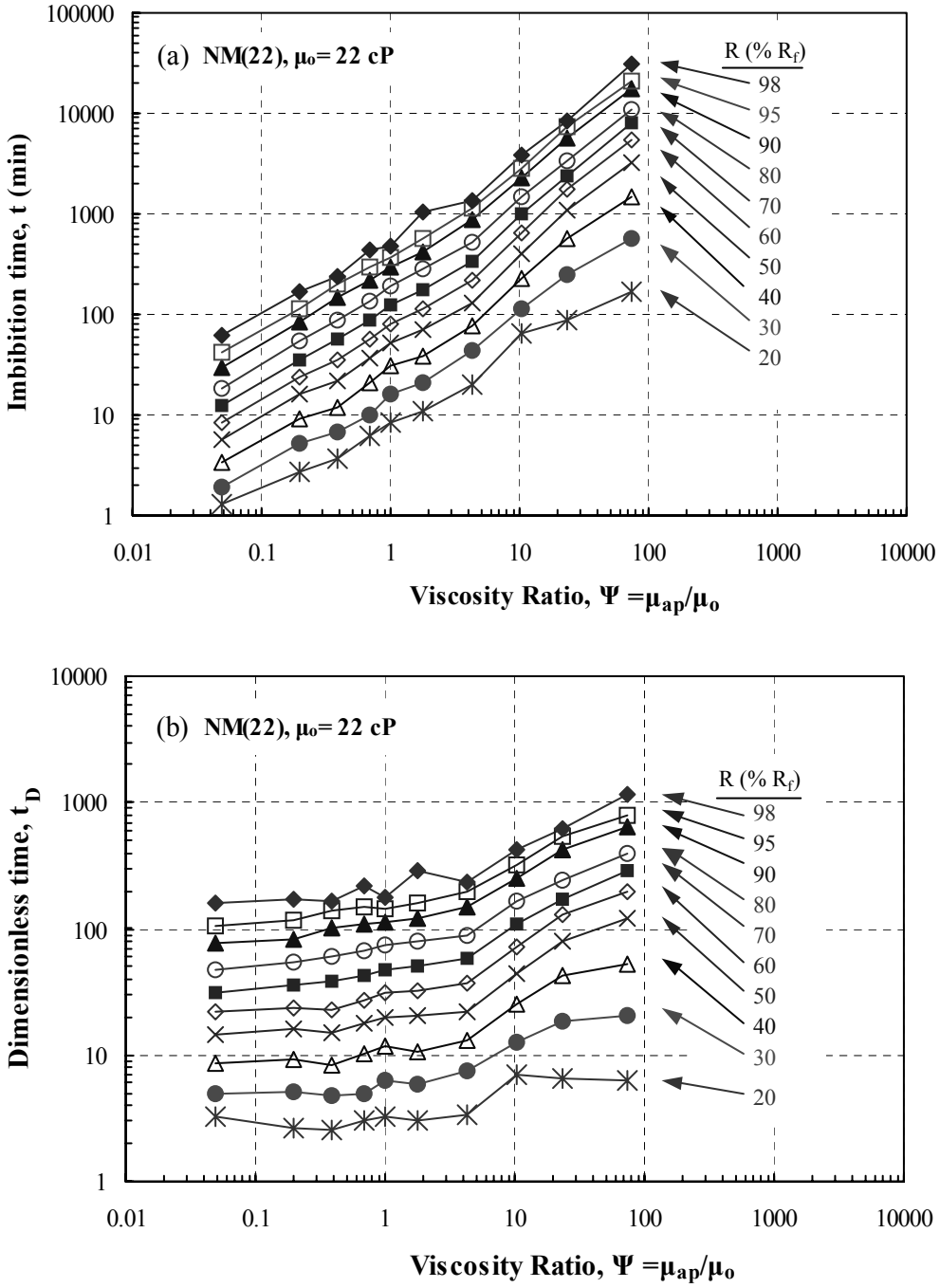

Fig. 10. Imbibition time (a) and dimensionless time (b) versus viscosity ratio (μ_o = 22 cP) for fractional recoveries, *R*, ranging from 20% to 98% (interpolated values for individual cores).

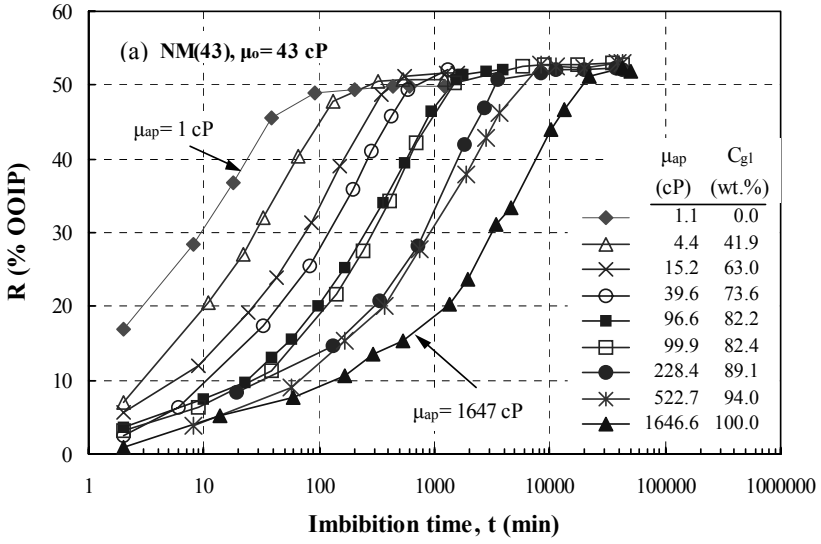

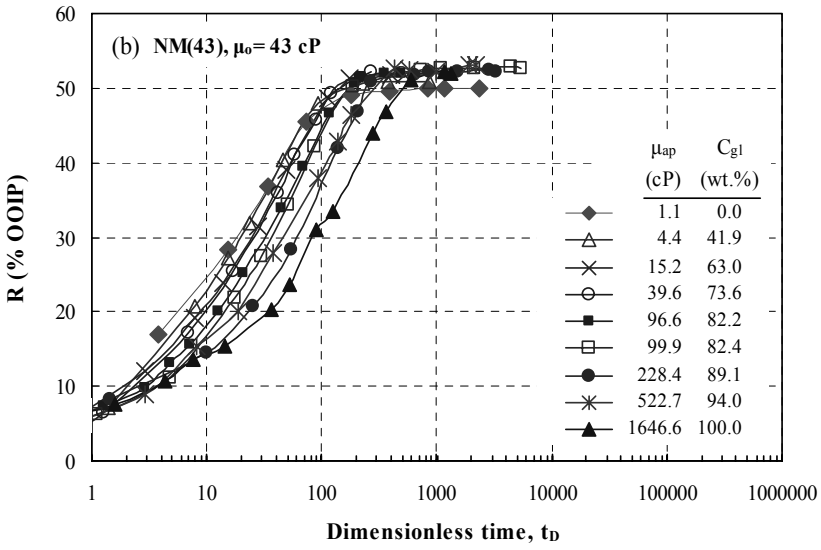

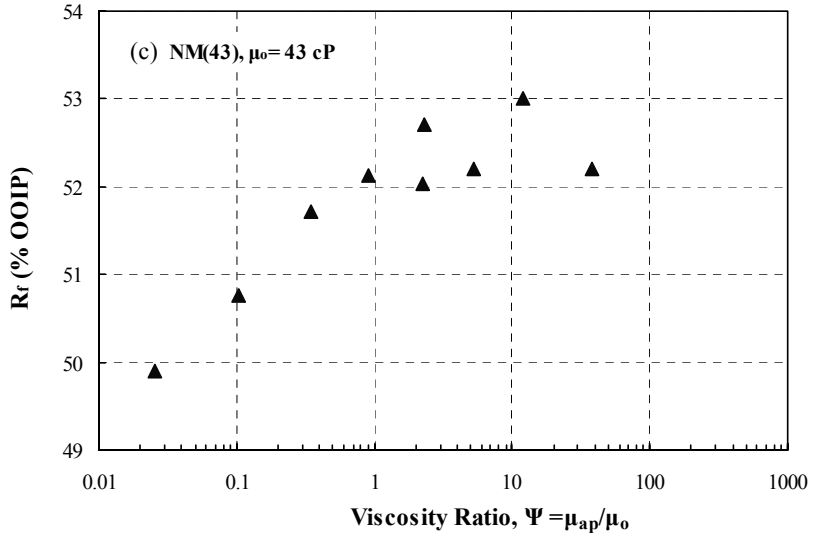

Fig. 11. Recovery of 43 cP oil by spontaneous imbibition for variation in aqueous phase viscosity versus (a) time and (b) dimensionless time; (c) final oil recovery, *Rf*, versus viscosity ratio.

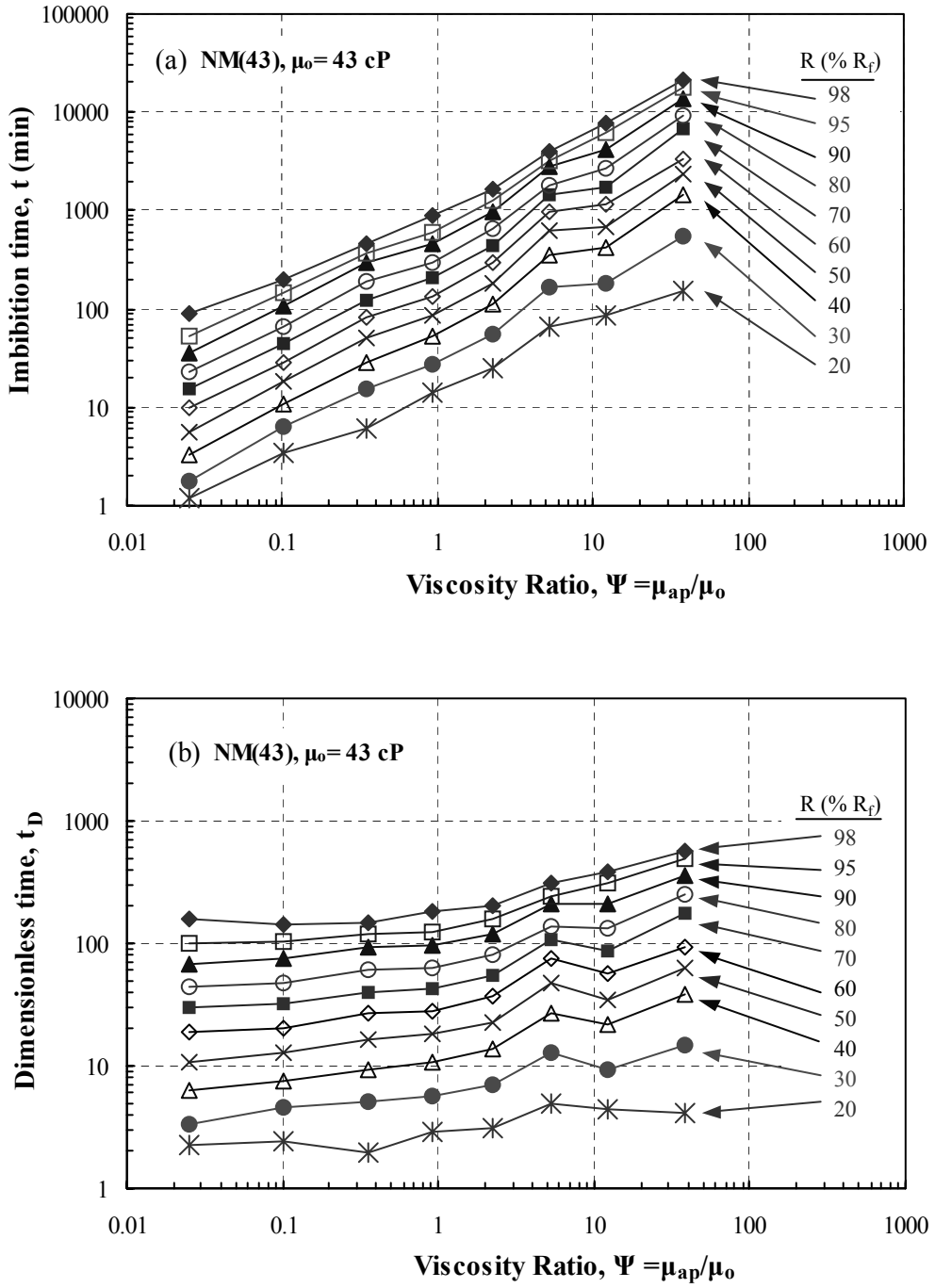

Fig.12. Imbibition time (a) and dimensionless time (b) versus viscosity ratio (μ_o= 43 cP) for fractional recoveries, *R*, ranging from 20% to 98% (interpolated values for individual cores).

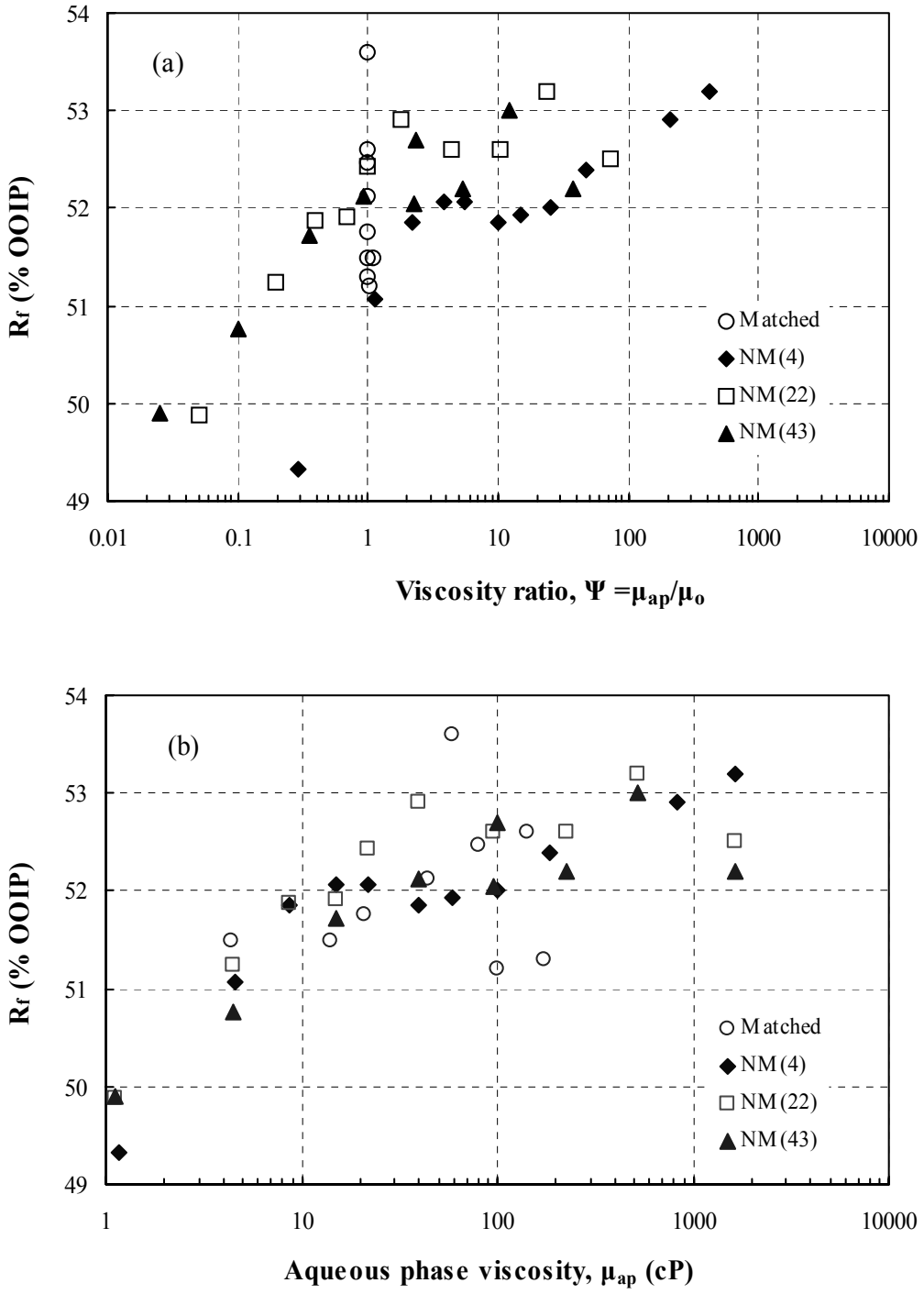

Fig. 13. Final oil recovery for all data sets versus (a) viscosity ratio and (b) aqueous phase viscosity.

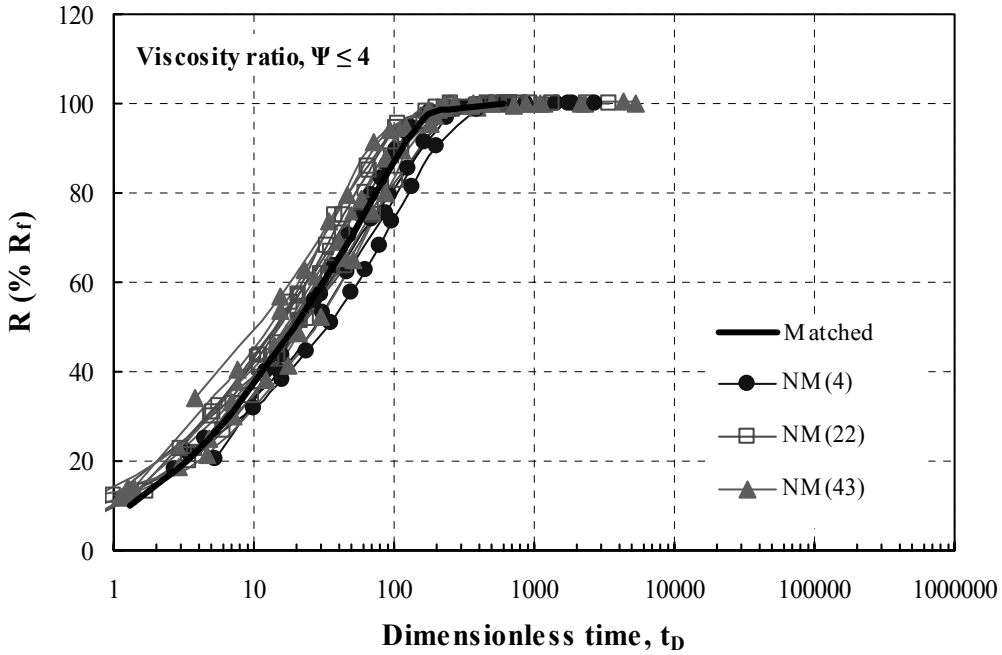

Fig. 14. Normalized recovery of matched viscosity oil, 4 cP, 22 cP and 43 cP oil by spontaneous imbibition for viscosity ratios ≤ 4 versus dimensionless time.

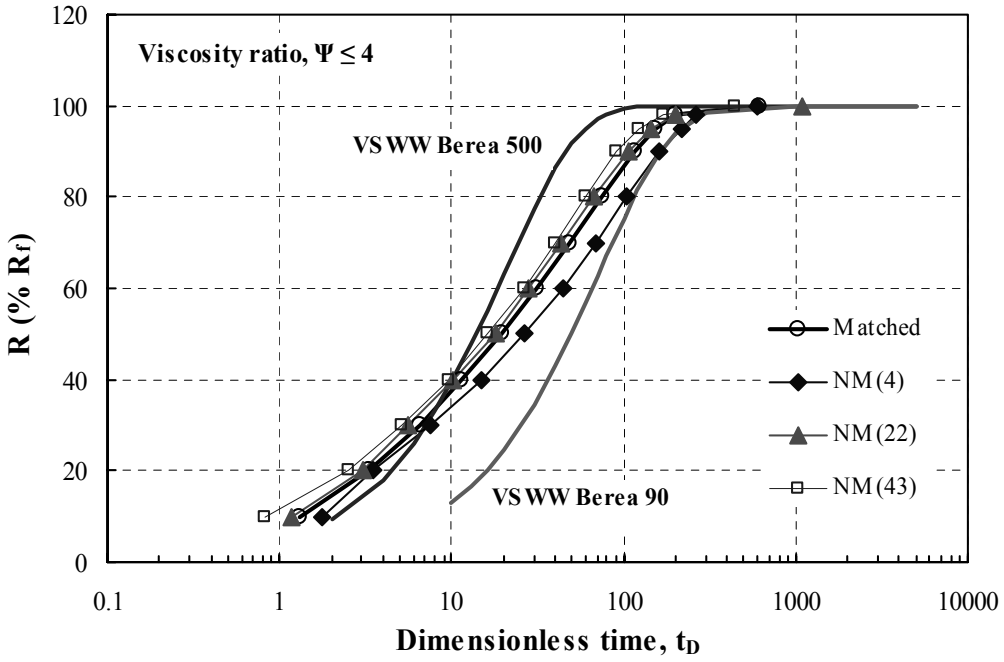

Fig. 15. Normalized recovery of averaged imbibition curves with viscosity ratios ≤ 4 versus dimensionless time.

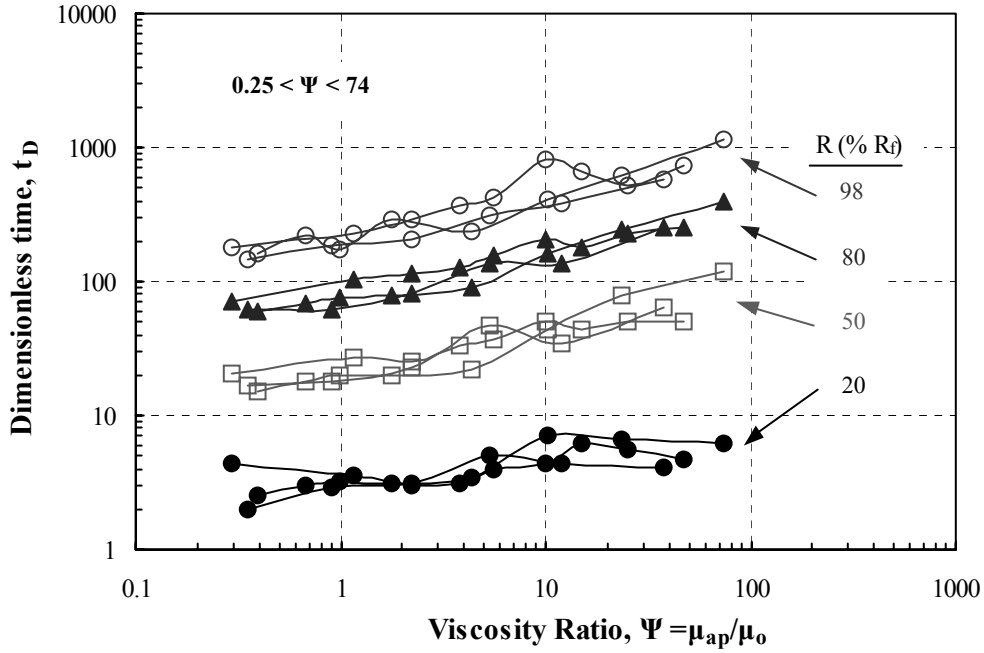

Fig.16. Relationship between dimensionless time and viscosity ratio for 20%, 50%, 80% and 98% of recoverable oil for viscosity ratios from 0.25 to 74 from data sets NM(4), NM(22) and NM(43).

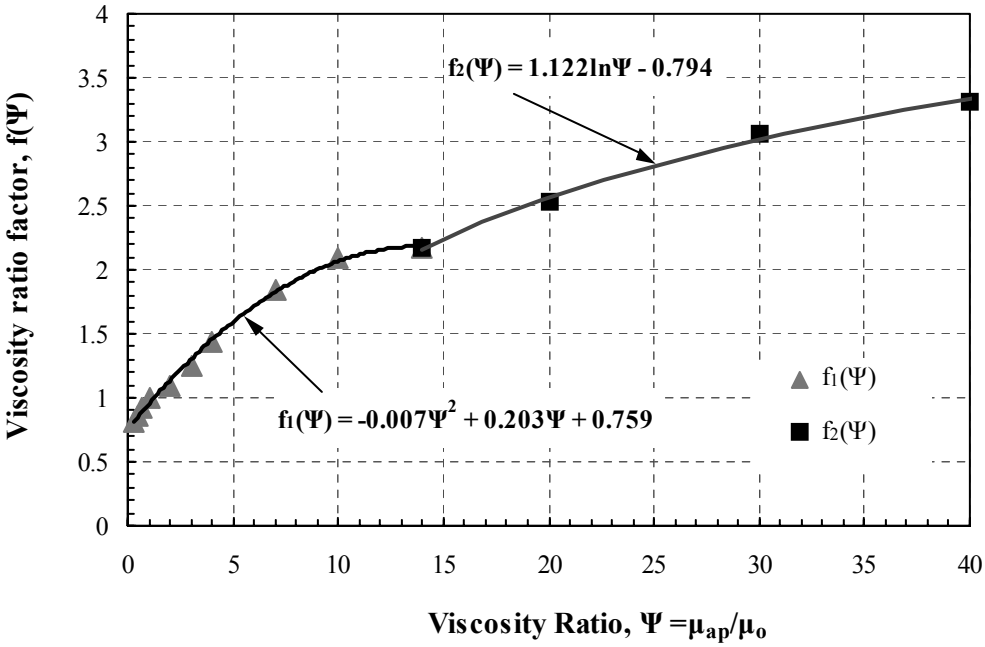

Fig.17. Viscosity ratio factor, *f(Ψ)*, as a function of viscosity ratio.

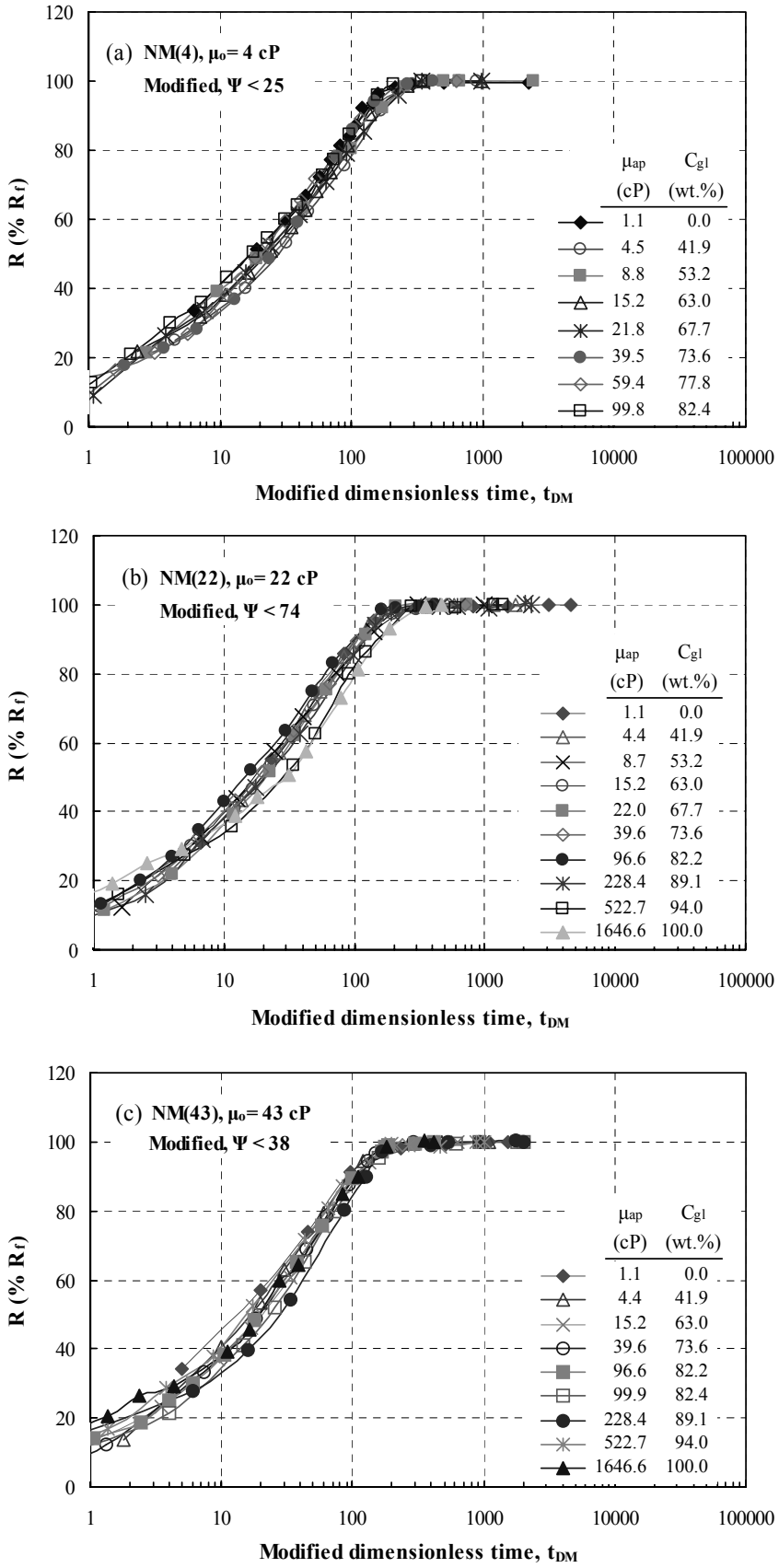

Fig. 18. Normalized recovery for (a) 4 cP oil, (b) 22 cP oil and (c) 43 cP oil versus modified dimensionless time, t_{DM}, for variation in aqueous phase viscosity.

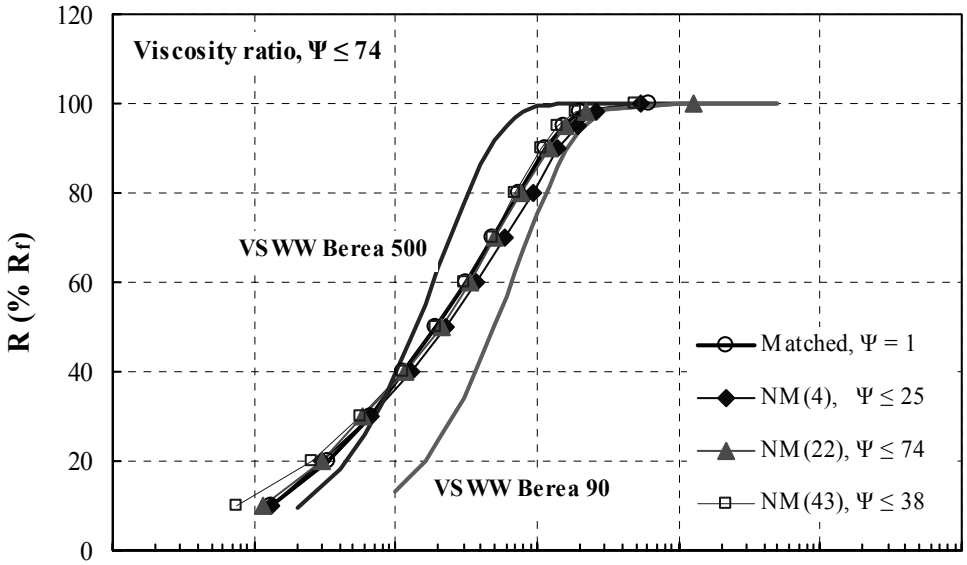

Fig. 19. Normalized recovery versus modified dimensionless time, t_{DM}.

Task 5. Comparison with similarity solutions.

(Douglas Ruth, Yu Li, Geoffrey Mason and Norman Morrow – in press, *Transport in Porous Media*)

ABSTRACT

An approximate analytical solution is provided for one-dimensional, counter-current, spontaneous imbibition of a wetting phase (water) into a semi-infinite porous media. The solution is based on the assumptions that a similarity solution exists for the displacement process. This assumption, in turn, rests on the assumption that the set of relative permeability and capillary pressures curves are unique functions of saturation and do not depend on the nature of the displacement. It further rests on the assumption that the saturation at the imbibition face does not vary with time. It is demonstrated that the solution is in agreement with results obtained from experiments and also numerical analyses of these experiments. The experiments utilize cylindrical samples with the radial surface and one end-face sealed and with imbibition proceeding from the open end-face. The stage of experiment that is modeled by the present solution is the period before the imbibition front contacts the sealed end-face. An important finding of the present analysis is that the pressure upstream of the advancing invasion front is a constant. A second, improved solution is also presented, this solution is an iterative, series solution of a integral-differential equation. It converges to a stable solution in very few terms.

1. INTRODUCTION

The displacement process in porous media is a notoriously non-linear and complex problem; therefore, it is no surprise that only a few cases have been found to have exact analytical solutions. The Buckley-Leverett (1942) solution predicts the forced displacement of one fluid by another provided that capillary pressure is zero. This is a restrictive condition for

most real displacement problems. Another solution was developed by Yortsos and Fokas (1983). Although this solution allows for the existence of capillary pressure, the shapes for the capillary pressure and relative permeability functions are constrained. This solution is very useful as a test case for other analytical methods because it is the only analytical solution available that includes all of the important mechanisms. However, it is not applicable for general displacement problems with arbitrary relative permeability and capillary pressure curves.

There are a number of approximate analytical solutions in the literature for two-phase flow; we consider below those solutions that can be applied to countercurrent, spontaneous imbibition. Chen (1988) obtained analytical solutions for countercurrent spontaneous imbibition that were asymptotic in nature. His paper contains a review of previous work by Chinese and Russian authors. Being asymptotic, these solutions do not cover the entire mobile saturation range. McWhorter and Sunada (1990) presented an integral solution for counter-current spontaneous imbibition that is similar to the solution in the present paper. In the present paper, a method is proposed to obtain approximate analytical solutions to the integrals. The recent work of Kashchiev and Firoozabadi (2003) provides analytical solutions for countercurrent imbibition but these solutions depend on capturing the dependence of the capillary pressure and relative permeabilities on saturation by means of a specific functional form; as a result, the equations are approximations to the equations that apply to the original problem.

There is a large literature, dating back until at least Rapoport (1955) and Handy (1960) that show that under certain conditions the process of counter-current spontaneous imbibition results in saturation profiles that are self-similar(see Morrow and Mason (2001) for a recent review). Self-similarity implies that the process of counter-current spontaneous imbibition scales with the square-root of time. The conditions of self-similarity and square-root of time scaling have been assumed in the work of Chen (1988) and McWhorter and Sunada (1990) and most previous analytical work. Li *et al* (2003) explored this behaviour both experimentally and mathematically; results from their work are used to validate the solution presented in the present paper.

There is an alternate approach to the analysis of counter-current, spontaneous imbibition that does not admit a similarity solution and the resulting square-root of time scaling. This approach is founded on the assumption that relative permeability curves are not unique functions of saturation but depend on the nature of the process. Essentially, the assumption that steady-state and non-steady-state processes can be predicted by a single set of relative permeability curves is claimed to be invalid, that is, non-equilibrium processes have different curves than equilibrium processes. This work has largely been pursued by Barenblatt and his co-workers. Early work only available in Russian is reviewed in Barenblatt, Entov, and Ryzhik (1990); the model is further pursued in the work by Barenblatt and Gil'man (1987) and Silin and Patzek (2004). The process they propose is to use the same curves but to transform the actual saturation into an effective saturation using particular mapping processes. This work has been successful in modeling some experimental results, particularly at early times during the process. This suggests that there may be conditions under which similarity exists and others where it does not. The present work is valid where experimental results demonstrate that square-root of time scaling exists.

The solution developed in the present paper is general in nature, allowing for any shape of capillary pressure and relative permeability functions. The solution is valid even if the saturation of the wetting phase at the front differs from the initial wetting phase saturation. Although the solution is not closed-form, it requires only straightforward, numerical integrations of well defined functions to achieve numerical results. The solution is verified by comparing production and pressure histories directly with experimental results, and by comparing saturation profiles with a numerical analysis of a set of experimental data. The simulator used is essentially the same as that described previously by Ruth *et al* (2003). Subsequent to the submission of the original version of the present paper, a preliminary version of the theory presented below was used to explore the influence of viscosity on spontaneous counter-current imbibition (Ruth *et al.* 2004).

2. EXPERIMENTAL

The counter-current, spontaneous imbibition of a wetting phase against a non-wetting phase in a homogeneous porous medium is considered for the case in which the fluids are incompressible and immiscible, and the process is modeled by relative permeability and capillary pressure curves that are unique function of the local saturation. The motion is originated by preferential wettability and sustained by the capillary pressure gradient that results from the saturation gradient. Gravity effects are neglected. A mathematical model for this process is developed for the case of linear flow along the axis of a columnar sample of infinite length with the columnar surface sealed. Hence, for a finite length sample, the solution is valid until the wetting phase front reaches the downstream end of the sample. A final assumption is that the saturation at the imbibition face remains constant.

2.1 The Solution for the Saturation Profile

The basic equations governing counter-current, spontaneous imbibition flow are the generalized Darcy law

$$q_w = -\frac{K k_{rw} A}{\mu_w} \frac{\partial P_w}{\partial x} \qquad 2.1\text{-}1$$

and

$$q_{nw} = -\frac{K k_{rnw} A}{\mu_{nw}} \frac{\partial P_{nw}}{\partial x} \qquad 2.1\text{-}2$$

the capillary pressure definition

$$P_c = P_{nw} - P_w \qquad 2.1\text{-}3$$

the continuity of flow

$$q_w = -q_{nw} \qquad 2.1\text{-}4$$

and the conservation of mass equations

$$\phi A \frac{\partial S_w}{\partial t} + \frac{\partial q_w}{\partial x} = 0 \qquad 2.1\text{-}5$$

and

$$\phi A \frac{\partial S_{nw}}{\partial t} + \frac{\partial q_{nw}}{\partial x} = 0 \qquad 2.1\text{-}6$$

Combining equations 2.1-1 through 2.1-4 results in

$$q_w = \frac{K k_{rw} k_{rnw} A}{\mu_w k_{rnw} + \mu_{nw} k_{rw}} \frac{\partial P_c}{\partial x} \qquad 2.1\text{-}7$$

or in terms of saturation

$$q_w = \frac{K k_{rw} k_{rnw} A}{\mu_w k_{rnw} + \mu_{nw} k_{rw}} \frac{\partial P_c}{\partial S_w} \frac{\partial S_w}{\partial x} \qquad 2.1\text{-}8$$

Defining the variable (here termed the "mobility variable")

$$M_w = \frac{K k_{rw} k_{rnw}}{\mu_w k_{rnw} + \mu_{nw} k_{rw}} \frac{\partial P_c}{\partial S_w} \qquad 2.1\text{-}9$$

then

$$q_w = M_w A \frac{\partial S_w}{\partial x} \qquad 2.1\text{-}10$$

This equation may be recast as

$$\partial x = \frac{M_w A}{q_w} \partial S_w \qquad 2.1\text{-}11$$

which may be integrated to yield

$$x_{S_w} = \int_{S_{wo}}^{S_w} \frac{M_w A}{q_w} \partial S_w \qquad 2.1\text{-}12$$

This equation is equivalent to the expression derived by McWhorter and Sunada (1990). Here x_{S_w} is the location of a saturation point as a function of time. The integral can be evaluated if we can determine a function for the flow rate in terms of saturation and time.

Eq. 2.1-5 can be rewritten in terms of the classic "frontal advance theory." At a fixed time, the derivative of the flow rate with position is given by

$$\left(\frac{\partial q_w}{\partial x}\right)_t = \left(\frac{\partial q_w}{\partial S_w}\right)_t \left(\frac{\partial S_w}{\partial x}\right)_t \qquad 2.1\text{-}13$$

S_w is a function of both x and t. It follows that

$$dS_w = \left(\frac{\partial S_w}{\partial x}\right)_t dx + \left(\frac{\partial S_w}{\partial t}\right)_x dt \qquad 2.1\text{-}14$$

Consider the case where we wish to follow the movement of the location of a point with a given saturation. The locus of such a point is defined by setting the total differential of saturation equal to zero in Eq.2.1-14. After rearranging we obtain

$$\left(\frac{\partial S_w}{\partial t}\right)_x = -\left(\frac{\partial S_w}{\partial x}\right)_t \left(\frac{\partial x}{\partial t}\right)_{S_w} \qquad 2.1\text{-}15$$

Substituting Eqs. 2.1-13 and 2.1-15 into Eq. 2.1-5 and factoring out the common term

$$\left(\frac{\partial x}{\partial t}\right)_{S_w} = \frac{1}{\phi A}\left(\frac{\partial q_w}{\partial S_w}\right)_t \qquad 2.1\text{-}16$$

If the solution is self-similar, then the saturation profile must simply stretch along the x-direction with time. For such a stretching, the necessary condition is that

$$\left(\frac{\partial x}{\partial t}\right)_{S_w} = a(t) F\left(S_{wo} - S_w\right) \qquad 2.1\text{-}17$$

where $a(t)$ is a function of time, $F\left(S_{wo} - S_w\right)$ is a function only of saturation, and S_{wo} is the saturation at the open face. In the present paper, S_{wo} will be assumed as constant throughout the displacement. If this saturation is not constant, then the similarity condition does not hold. As a first approximation, the function of saturation will be approximated by the expression:

$$F\left(S_{wo} - S_w\right) = \left(S_{wo} - S_w\right) \qquad 2.1\text{-}18$$

Combining Eqs. 2.1-16 through 2.1-18, and integrating

$$q_w = -a(t)\,\phi A \frac{\left(S_{wo} - S_w\right)^2}{2} + C \qquad 2.1\text{-}19$$

where C is a constant of integration.

Imbibition experiments can be run with any initial water saturation, S_{wi}, of almost any value between 0 and 1. Because flow is sustained by saturation gradients, the initial, constant saturation in the sample cannot result in any flow, despite the fact that the two phases may be mobile. It follows that the constant in Eq. 2.1-19 can be recovered by setting the flow rate at S_{wi} to zero. Therefore

$$C = a(t)\,\phi\, A\,\frac{(S_{wo} - S_{wi})^2}{2} \qquad 2.1\text{-}20$$

and

$$q_w = -a(t)\,\phi\, A\left(\frac{(S_{wo} - S_w)^2 - (S_{wo} - S_{wi})^2}{2}\right) \qquad 2.1\text{-}21$$

Equation 2.1-5 may be written as

$$\phi A\frac{\partial S_w}{\partial t} + \frac{\partial q_w}{\partial S_w}\frac{\partial S_w}{\partial x} = 0 \qquad 2.1\text{-}22$$

or by means of Eq. 2.1-21

$$\frac{\partial S_w}{\partial t} + a(t)(S_{wo} - S_w)\frac{\partial S_w}{\partial x} = 0 \qquad 2.1\text{-}23$$

The self similar variable for this equation is of the form

$$\eta = \frac{x}{\sqrt{t}} \qquad 2.1\text{-}24$$

It follows that

$$\frac{\partial}{\partial x} = \frac{\partial \eta}{\partial x}\frac{\partial}{\partial \eta} = \frac{1}{\sqrt{t}}\frac{\partial}{\partial \eta} \qquad 2.1\text{-}25$$

and

$$\frac{\partial}{\partial t} = \frac{\partial \eta}{\partial t}\frac{\partial}{\partial \eta} = -\frac{1}{2}\frac{\eta}{t}\frac{\partial}{\partial \eta} \qquad 2.1\text{-}26$$

Equation 2.1-23 then becomes

$$-\frac{1}{2}\frac{\eta}{t}\frac{dS_w}{d\eta}+a(t)\ \left[(S_{wo}-S_w)\right]\frac{1}{\sqrt{t}}\frac{\partial S_w}{\partial \eta}=0 \qquad 2.1\text{-}27$$

This equation suggests that for similarity to hold,

$$a(t)=\frac{a_c}{\sqrt{t}} \qquad 2.1\text{-}28$$

and

$$a_c(S_{wo}-S_w)=\frac{\eta}{2} \qquad 2.1\text{-}29$$

which is a relatively simple relationship between saturation and the similarity variable.

The solution in Eq. 2.1-29 bears much similarity with the well known approximate method proposed by Goodman (1964) and used extensively in the analysis of transient heat transfer problems. In these problems, an approximate temperature profile is assumed and parameters in this equation are found in such a way that they satisfy global (that is, integral) conditions. By analogy, we could have started with Eq. 2.1-29 and proceeded in reverse. The present solution also has similarities to that developed in Barenblatt *et al* (1990). In their case, they approximated a slightly different form of the equation but arrived at a form that has many similarities to Eq. 2.1-21. Their approximation was to assume that (in the present notation)

$$\int_0^{S_w} M_w\, dS_w = C_1 + C_2(S_{wo}-S_w)^n \qquad 2.1\text{-}30$$

where C_1 and C_2 are constants. As such, their solution bears similarity to the approach taken by Kashchiev and Firoozabadi (2003). Another difference is that they assumed that the saturation at the inlet face was the value that leads to the condition $P_c=0$.

The present method provides more flexibility in deriving a saturation profile. By assuming a simple relation for the stretching parameter, and not the saturation profile, it is possible to derive an alternate function for the profile of the saturation. Combining Eqs. 2.1-10, 2.1-21, 2.1-25, and 2.1-28

$$-\phi\ \ a_c\left(\frac{(S_{wo}-S_w)^2-(S_{wo}-S_{wi})^2}{2}\right)=M_w\frac{\partial S_w}{\partial \eta} \qquad 2.1\text{-}31$$

Integrating this equation gives a second equation relating saturation and the similarity variable

$$\frac{1}{\phi}\int_{S_{wo}}^{S_w}\frac{2M_w}{a_c\left((S_{wo}-S_w)^2-(S_{wo}-S_{wi})^2\right)}dS_w=-\eta_{S_w} \qquad 2.1\text{-}32$$

where the condition

$$\eta_{S_{wo}} = 0 \qquad \text{2.1-33}$$

has been applied. In opposition to Equation 2.1-29, Equation 2.1-32 accounts for the complexities introduced by the mobility variable M_w. The present solution therefore shares a basic principle with the Goodman solution, but applies it to a different variable.

The mean saturation is given by

$$\overline{S}_w = \frac{1}{\eta_f}\int_0^{\eta_f} S_w d\eta \qquad \text{2.1-34}$$

Using Equation 2.1-31 to change the integration variable and Equation 2.1-32 to calculate the value of the similarity variable at the front

$$\overline{S}_w = \frac{\displaystyle\int_{S_{wo}}^{S_{wf}} \frac{M_w S_w}{\left((S_{wo}-S_w)^2-(S_{wo}-S_{wi})^2\right)} dS_w}{\displaystyle\int_{S_{wo}}^{S_{wf}} \frac{M_w}{\left((S_{wo}-S_w)^2-(S_{wo}-S_{wi})^2\right)} dS_w} \qquad \text{2.1-35}$$

This equation do not constitute a complete solution because the values of S_{wo} and S_{wf} must be provided independently. However, if the values of these parameters are known, then this equation has great utility in predicting the performance of the imbibition process.

2.2 The Solution for the Time Dependence

Because the profile is only stretched along the *x*-axis with time, the average saturation between the open face and x_f must remain constant and the amount of wetting phase that penetrates the sample is given by

$$Q_w = \phi\, A\, x_f(t)\left(\overline{S}_w - S_{wi}\right) \qquad \text{2.2-1}$$

where S_{wi} is the initial wetting phase saturation and $x_f(t)$ is the location of the front. The total wetting phase imbibed is also given by the equation

$$Q_w = \int_0^t (q_w)_o \, dt \qquad \text{2.2-2}$$

where $(q_w)_o$ is the flow at the open face. From Eq.2.1-21, this flow rate is given by

$$(q_w)_o = a(t)\,\phi\,A\,\frac{(S_{wo}-S_{wi})^2}{2} \qquad 2.2\text{-}3$$

It follows that

$$a_c\,\frac{(S_{wo}-S_{wi})^2}{2}\int_0^t \frac{dt}{\sqrt{t}} \;=\; x_f(t)\left(\overline{S}_w - S_{wi}\right) \qquad 2.2\text{-}4$$

or

$$x_f(t) = \frac{a_c\sqrt{t}\,(S_{wo}-S_{wi})^2}{\left(\overline{S}_w - S_{wi}\right)} \qquad 2.2\text{-}5$$

Combining Equations 2.1-24 and 2.1-32 evaluated at the front

$$x_f(t) = -\frac{\sqrt{t}}{\phi}\int_{S_{wo}}^{S_{wf}} \frac{2M_w}{a_c\left((S_{wo}-S_w)^2-(S_{wo}-S_{wi})^2\right)}\,dS_w \qquad 2.2\text{-}6$$

Equating the last two equations and rearranging

$$a_c = \sqrt{-\frac{2}{\phi}\,\frac{\left(\overline{S}_w - S_{wi}\right)}{(S_{wo}-S_{wi})^2}\int_{S_{wo}}^{S_{wf}} \frac{M_w}{\left((S_{wo}-S_w)^2-(S_{wo}-S_{wi})^2\right)}\,dS_w} \qquad 2.2\text{-}7$$

2.3 The Pressure Distributions

Rewriting Eqs. 2.1-1 as

$$\frac{\partial P_w}{\partial x} = -q_w\,\frac{\mu_w}{K k_{rw} A} \qquad 2.3\text{-}1$$

and using Eq. 2.1-10

$$\frac{\partial P_w}{\partial x} = -\frac{\mu_w\,M_w}{K k_{rw}}\quad\frac{\partial S_w}{\partial x} \qquad 2.3\text{-}2$$

This equation may be integrated from the open face of the sample to any S_w section to obtain the pressure in the wetting phase at that S_w section

$$P_w - P_{wo} = -\frac{\mu_w}{K}\int_{S_{wo}}^{S_w}\frac{M_w}{k_{rw}}\,dS_w \qquad 2.3\text{-}3$$

where P_{wo} is the pressure in the wetting phase at the open face. This pressure will always be zero. The pressure in the non-wetting phase at this S_w section is

$$P_{nwf} = P_{wf} + P_c \qquad 2.3\text{-}4$$

Eq. 2.3-3 provides a very interesting result. Because the integral is constant with time, depending only on the saturation profile shape, the pressure at the front is also constant! It must be noted that this is an exact result and does not depend on the approximation represented by Eq. 2.1-18. It does however rely on the assumptions that enable similarity to exist.

2.4 An Improved Solution

An improved solution for the saturation profile may be obtained as follows. Combining equations 2.1-22, and 2.1-24 through 2.1-26 results in

$$-\phi A \frac{1}{2}\frac{\eta}{t}\frac{dS_w}{d\eta} + \frac{\partial q_w}{\partial S_w}\frac{1}{\sqrt{t}}\frac{\partial S_w}{\partial \eta} = 0 \qquad 2.4\text{-}1$$

The flow rate scales as

$$q_w = \frac{q_s}{\sqrt{t}} \qquad 2.4\text{-}2$$

Therefore

$$-\phi A \frac{\eta}{2}\frac{dS_w}{d\eta} + \frac{\partial q_s}{\partial S_w}\frac{\partial S_w}{\partial \eta} = 0 \qquad 2.4\text{-}3$$

or

$$-\phi A \frac{\eta}{2}\frac{dS_w}{d\eta} + \frac{\partial q_s}{\partial \eta} = 0 \qquad 2.4\text{-}4$$

Combining Eqs. 2.1-10, 2.1-25 and 2.4-2

$$q_s = M_w A \frac{\partial S_w}{\partial \eta} \qquad 2.4\text{-}5$$

Eq. 2.4-4 may therefore be written as

$$-\phi \frac{\eta}{2}\frac{dS_w}{d\eta} + \frac{\partial}{\partial \eta}\left(M_w \frac{\partial S_w}{\partial \eta} \right) = 0 \qquad 2.4\text{-}6$$

Let

$$\Lambda = \frac{\eta}{\eta_f} \qquad 2.4\text{-}7$$

Then

$$-\phi \frac{\eta_f^2}{2} \Lambda \frac{dS_w}{d\Lambda} + \frac{\partial}{\partial \Lambda}\left(M_w \frac{\partial S_w}{\partial \Lambda} \right) = 0 \qquad 2.4\text{-}8$$

By the product rule

$$-\phi \frac{\eta_f^2}{2}\left(\frac{d\Lambda S_w}{d\Lambda} - S_w \right) + \frac{\partial}{\partial \Lambda}\left(M_w \frac{\partial S_w}{\partial \Lambda} \right) = 0 \qquad 2.4\text{-}9$$

Integrating between $\Lambda = 0$ and any arbitrary value

$$\phi \frac{\eta_f^2}{2}\left(\int_0^{\Lambda} S_w d\Lambda - \Lambda S_w \right) + M_w \frac{\partial S_w}{\partial \Lambda} - \left(M_w \frac{\partial S_w}{\partial \Lambda} \right)_{\Lambda=0} = 0 \qquad 2.4\text{-}10$$

The saturation may now be expanded in a series (this stage represents a generalization of Goodman's solution method)

$$S_w = \sum_{i=0} a_i \Lambda^i \qquad 2.4\text{-}11$$

to obtain

$$\phi \frac{\eta_f^2}{2}\left(\sum_{i=0} \frac{a_i}{i+1} \Lambda^{i+1} - \sum_{i=0} a_i \Lambda^{i+1} \right) + M_w \sum_{i=1} i a_i \Lambda^{i-1} - M_{w0}\, a_1 = 0 \qquad 2.4\text{-}12$$

or

$$\sum_{i=1} a_i \left(M_w i \Lambda^{i-1} - M_{w0}\, \delta_{1i} - \phi \frac{\eta_f^2}{2} \frac{i}{i+1} \Lambda^{i+1} \right) = 0 \qquad 2.4\text{-}13$$

This equation may be solved by the least squares method to obtain the coefficients of the series. The value of the mobility variable can be evaluated using the saturation solutions given by Eq. 2.1-32 as a first approximation to obtain values of saturation that correspond to values of Λ. The value of η_f can be found from the limiting value of the integral in Eq. 2.1-32. The boundary conditions for the series can be found from the two equations

$$S_{wo} = a_0 \qquad \text{2.4-14}$$

and

$$S_{wf} = \sum_i a_i \qquad \text{2.4-15}$$

The solution can then be refined by successive approximations using the previous series to obtain new values for the series constants. However, new values of η_f must be obtained for each refinement. These new values can be obtained as follows.

The mean saturation may be calculated by inserting the series solution into the integral

$$\overline{S}_w = \int_0^1 S_w d\Lambda \qquad \text{2.4-16}$$

to obtain

$$\overline{S}_w = \sum_i \frac{a_i}{i+1} \qquad \text{2.4-17}$$

Using this equation and Eq. 2.1-24, Eq. 2.2-1 may be written as

$$Q_w = \phi\, A\, \eta_f \sqrt{t} \left(\sum_i \frac{a_i}{i+1} - S_{wi} \right) \qquad \text{2.4-18}$$

Using Eq. 2.1-10, 2.4-7 and 2.1-25, Eq. 2.2-2 may be written as

$$Q_w = \frac{M_{w0} A}{\eta_f} \left(\frac{\partial S_w}{\partial \Lambda} \right)_0 \int_0^t \frac{1}{\sqrt{t}}\, dt \qquad \text{2.4-19}$$

and

$$Q_w = \frac{2 a_1 M_{w0} A}{\eta_f} \sqrt{t} \qquad \text{2.4-20}$$

Equating 2.4-18 and 2.4-20, and solving for η_f

$$\eta_f = \sqrt{\frac{2a_1 M_{w0}}{\phi\left(\sum_i \frac{a_i}{i+1} - S_{wi}\right)}} \qquad 2.4\text{-}21$$

This equation has an unforeseen consequence. Because it depends directly on M_{w0}, it is obvious that M_{w0} cannot be equal to zero or the similarity variable at the front would be identically zero and imbibition would not proceed. Therefore, the saturation of the non-wetting phase at the entrance cannot be at the residual value.

3. Results and Discussion

The approximate analytical solutions were studied by comparison with experimental results and a numerical analysis of those results. The numerical work used an explicit, two-phase simulator. The simulator was used to history match the experiments, thereby obtaining a set of relative permeability and capillary pressure curves that allowed prediction of the experimental data. These curves were then used in the similarity solution. The simulator was also used to predict saturation profiles that could be directly compared with those predicted by the similarity solution.

The curves used are of the form

$$k_{rnw} = k_{roe}\left(\frac{1 - S_w - S_{rnw}}{1 - S_{rnw} - S_{rw}}\right)^{n_{nw}} \qquad 3\text{-}1$$

$$k_{rw} = k_{rwe}\left(\frac{S_w - S_{rw}}{1 - S_{rnw} - S_{rw}}\right)^{n_w} \qquad 3\text{-}2$$

and

$$P_c = P_{cp}\left[1 - \frac{P_{cp} - P_{ct}}{P_{cp}}\left(\frac{S_w - S_{rw}}{1 - S_{rnw} - S_{rw}}\right)^{n_P}\right] \qquad 3\text{-}3$$

Here S_w is the wetting phase saturation. S_{wr} is the residual saturation of wetting phase and S_{rnw} is the residual saturation of the non-wetting phase. The endpoint relative permeabilities are denoted by k_{rnwe} and k_{rwe} while n_{nw} and n_w are exponents that control the shapes of the curves. The final counter-current, spontaneous imbibition saturation, which corresponds to the saturation at the open face, S_{wo}, is always lower than the final co-current spontaneous imbibition saturation or the final forced imbibition saturation, (1-S_{or}) [see Li *et al*, 2003]. S_{nwr} is the residual non-wetting phase saturation, the saturation when the remaining oil is discontinuous in the porous media, and should never correspond to 1-S_{wo} because mobility of the non-wetting phase at the face is required for this phase to be produced. For the capillary pressure (P_c) curve during counter-current, spontaneous imbibition, P_{ct} is the capillary pressure when S_w is at its maximum value 1-S_{rnw} and P_{cp} is the capillary pressure when S_w is at its minimum value S_{rw}.

The data used to test the analytical model is based on one of the cases published by Li, *et al* (2004) (Sample H8O). The experimental data included both production and pressure data. In order to model this data, a history matching process, based on a numerical simulation, was used. This resulted in the values given in Table 1. The numerical model was then used to calculate saturation profiles that could be directly compared with the similarity solutions.

***(i) Table 1:** The test parameters considered in the present study.*

Variable	Value	Units	Variable	Value	Units
ϕ	0.221	-	K	1.094	mD
L	6.864	cm	D	3.796	cm
μ_{nw}	3.8	cp	μ_w	1.19	cp
k_{rnwe}	0.6	-	k_{rwe}	0.04	-
n_{nw}	2.6	-	n_w	3.0	-
S_{wo}	0.525	-	P_{cp}	6.5	kpa
P_{ct}	2.55	kpa	n_P	1.75	-

Figure 1 shows the curves for both the relative permeability and capillary pressure. These curves are typical for Berea sandstone.

Figure 2 shows results for the saturation profiles calculated from the numerical model and those calculated using the model derived in Section 2.3, referred to here as the base case. The dots represent the numerical solution while the line is the results from the base case. The solution, although approximately, shows very good agreement except very near the front. Figure 3 shows a similar comparison using the improved solution of Section 2.4, utilizing 3, 6 and 12 terms. (A solution using 9 terms was essentially the same as the 12-term case.) The 12-term case gives very good agreement.

Figure 4 shows a comparison for production versus time, of the experimental results and those for the base case and the 12-term case. Again the base case shows good agreement but the 12-term case shows better agreement.

Figure 5 demonstrates that the pressure ahead of the front is indeed constant. Except for the last point, theory and experiment are in essentially exact agreement. The last point is influenced by the fact that the front is approaching the end of the sample.

4. CONCLUSIONS

The present paper has presented an analytical solution for one-dimensional, linear, counter-current, spontaneous imbibition into a porous sample for the period before the invading phase contacts the end of the sample. The analytical method is valid for arbitrary relative permeability, capillary pressure, and other sample parameters. In order for the solution to be used, the saturation at the open face and the saturation at the front must be specified.

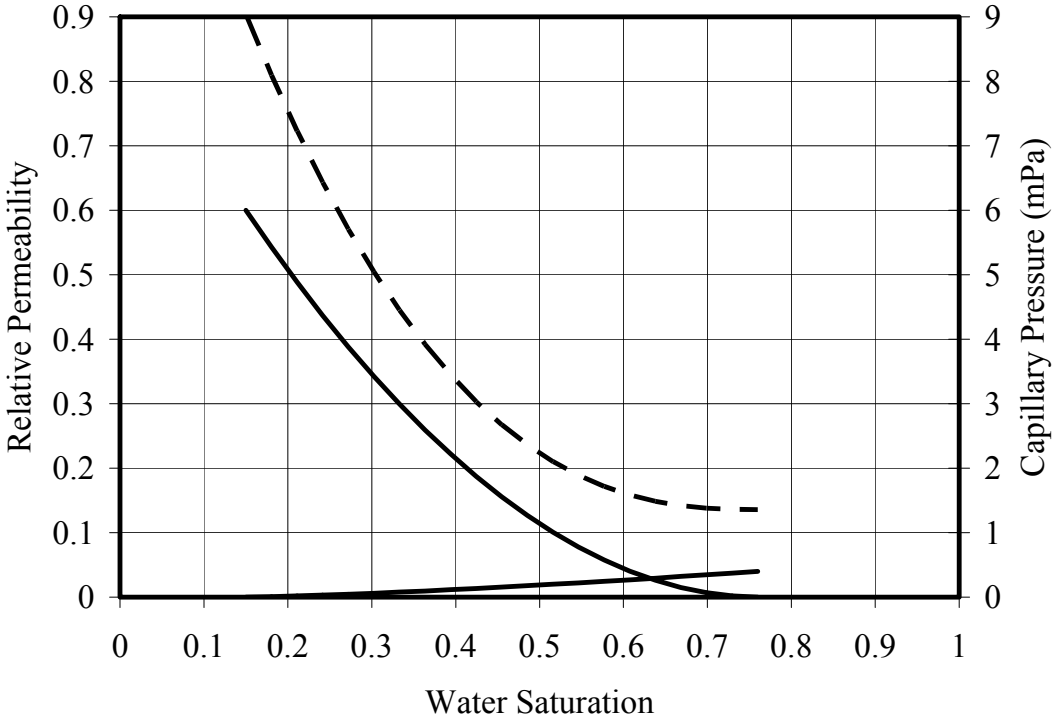

Figure 1 The relative permeability and relative permeability curves. The solid lines are the relative permeability curves and the capillary pressure is shown by the broken line.

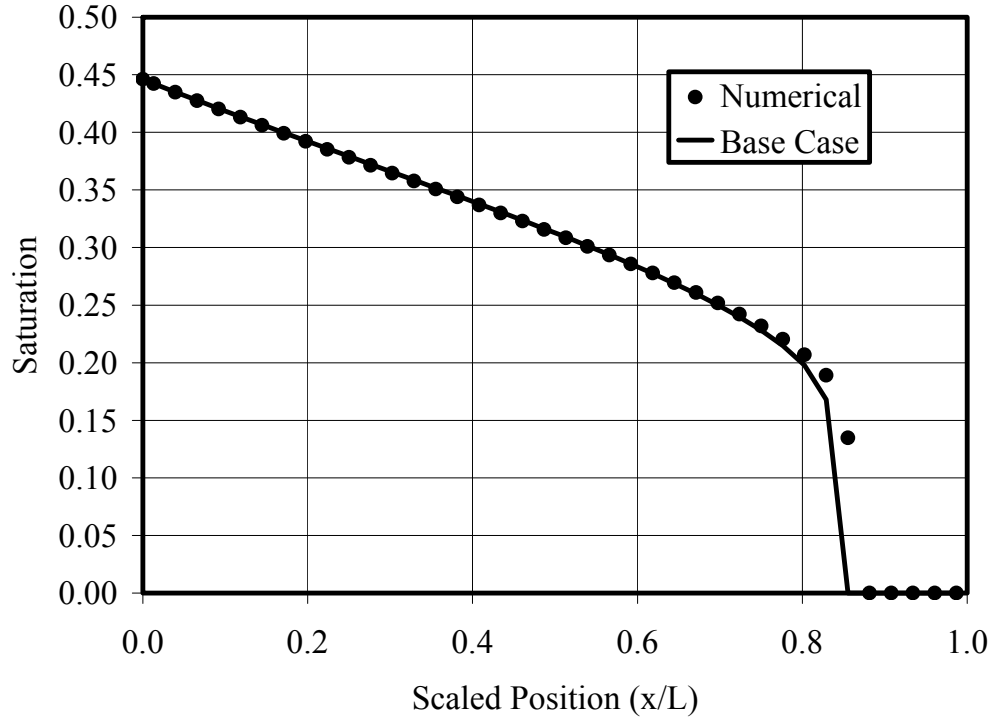

Figure 2 The saturation profile as calculated by the numerical simulation and the base model represented by Eq. 2.1-32.

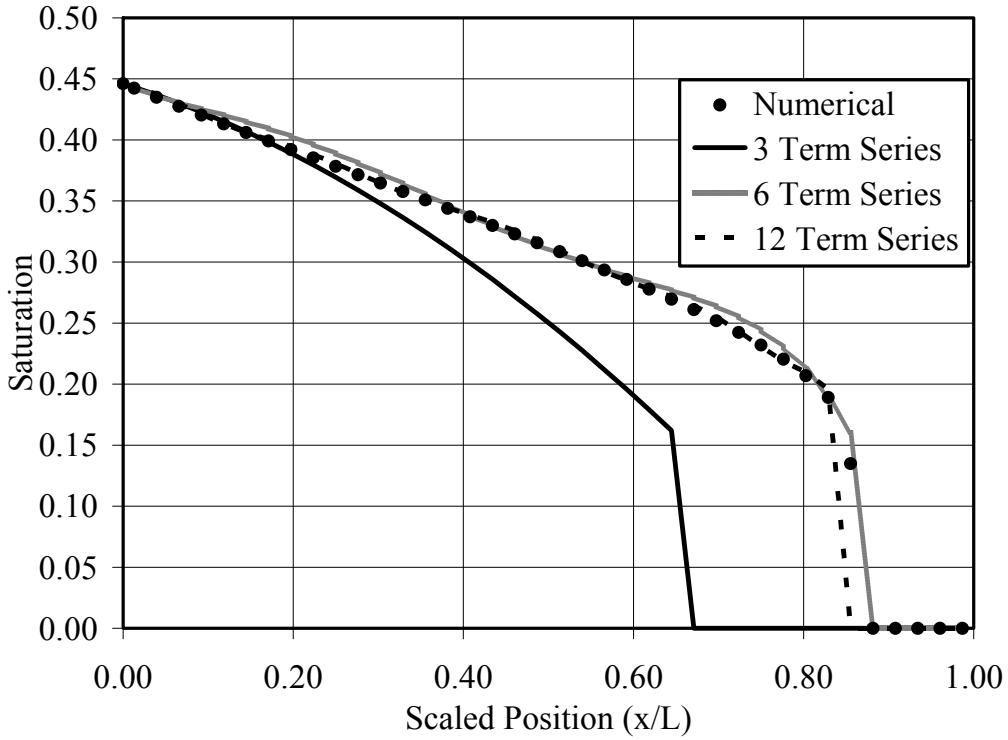

Figure 3 The saturation profile as calculated by the numerical simulator and three series with 3, 6, and 12 terms respectively.

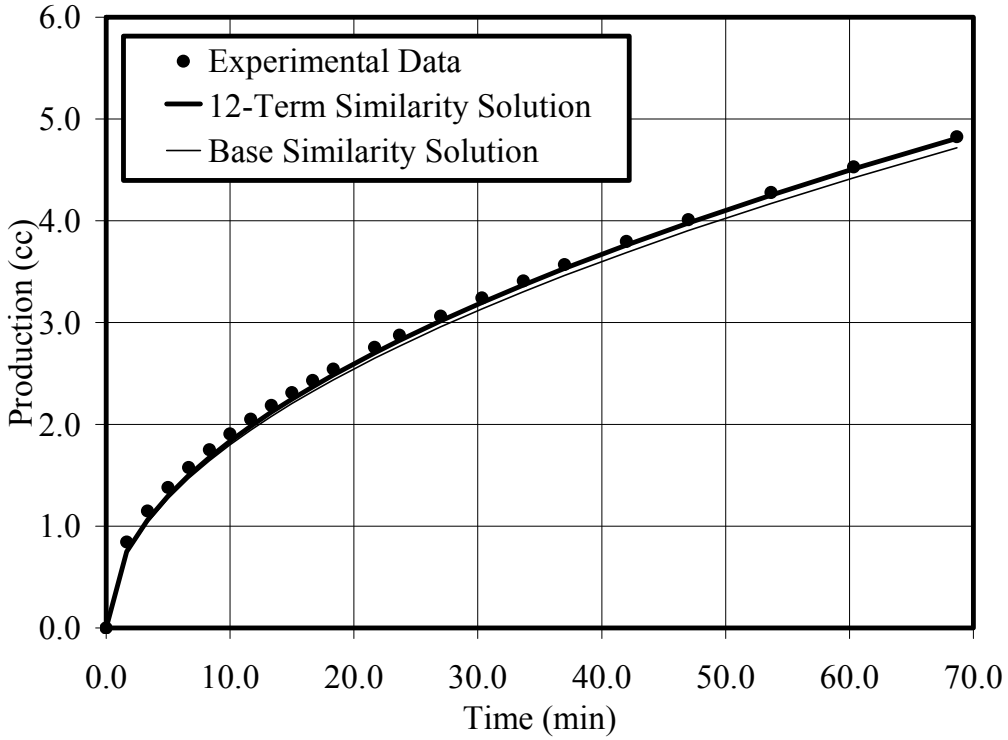

Figure 4 The production versus time as measured experimentally and predicted by the base model and the 12 term series model.

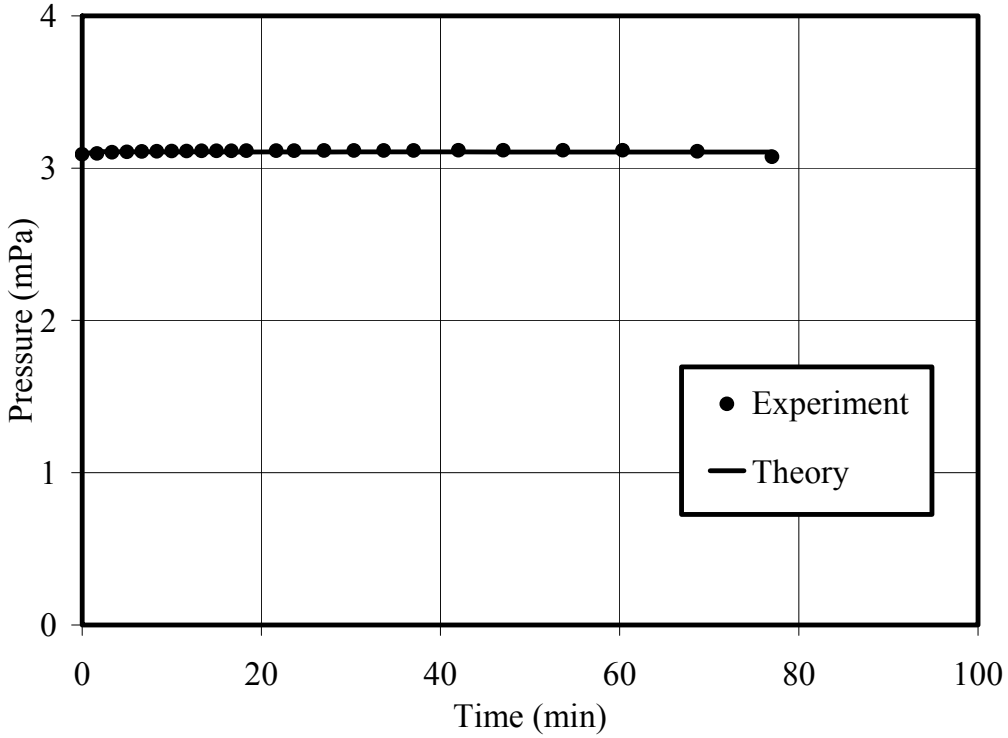

Figure 5 The pressure upstream of the front as measured in the experiment and predicted by the theory.

CONCLUSIONS

1. Consistent relationships have been found between work of displacement from capillary pressure drainage curves and directly measured changes in interfacial areas.

2. Spontaneous imbibition data for different boundary conditions have been correlated by a simple tube model that compensates for radial versus linear flow and for cores will all faces open.

3. (a) A period of frontal flow has been identified for linear COUCSI during which the distance advanced by the front is proportional to the square root of time. This result is consistent with a similarity solution for the frontal advance period.

(b)The capillary back pressure associated with production of NWP at the open face of the sample, is essentially constant during the frontal flow period. The production mechanism at the open face is basically a drainage process.

(c) From simulations that assume fixed relative permeabilities and scaled imbibition capillary pressure, the capillary back pressure in the oil/air case is about 2/5 down to 1/3 and in the water/oil case about 1/4 down to 1/9 of the capillary pressure at the imbibition front in Berea sandstone with permeabilities ranging from 0.065 to 1.1 μm^2.

4. Imbibition results for viscosity ratios of less than 4 were closely correlated by the Ma et al. scaling group with only very small but systematic dependence of dimensionless time on viscosity ratio. However, final oil recovery for unmatched liquid viscosities increased slightly with increase in aqueous phase/oil viscosity ratio up to about 4. Increase in dimensionless time for imbibition with viscosity ratio was observed for viscosity ratios greater than 4 but final oil recoveries were close to constant.

5. The present study has presented an analytical solution for one-dimensional, linear, counter-current, spontaneous imbibition into a porous sample for the period before the invading phase contacts the end of the sample. The analytical method is valid for arbitrary relative permeability, capillary pressure, and other sample parameters. In order for the solution to be used, the saturation at the open face and the saturation at the front must be specified.

REFERENCES

Alpak F.O., Lake L.W. and, Embid S.M., "Validation of a modified Carman – Kozeny equation to model two phase relative permeabilities", SPE (56479) Annual Technical Conference and Exhibition, Houston, TX, 3 – 6th Oct 1999.

Aziz, K.,K., Settari, A., 1979. Petroleum Reservoir Simulation, Applied Science Publishers, London

Baldwin, B.A., Spinler, E.A., 1999. In-situ saturation development during spontaneous imbibition, Proceedings of the International Society of Core Analysts, SCA-9922, pp. 1-11.

Bradford S., Leij F, "Estimating area for multi-fluid soil systems", Journal of Contaminant Hydrology, 27 (1997) 83-105

Barenblatt, G.I., Entov, V.M. and Ryzhik, V.M., Theory of Fluid Flow Through Natural Rocks, Kluwer Academic Publishers, 1990.

Barenblatt, G.I. and Gil'man, A.A., Nonequilibrium Counterflow Capillary Impregnation, *Journal of Engineering Physics (A translation of Inzhenero-fizcheskii Zhurnal)*, **52**, pp. 335-339.

Buckley, S.E. and Leverett, M.C., 1942, Mechanism of displacement in sands, *Trans. AIME,* **146**, pp. 107-116.

Chatzis I, Morrow N R, 1984. Correlation of capillary number relationships for sandstone, Soc. Pet. Eng. J., pp. 555-562.

Chen, Z.-X., 1988, Some invariant solutions to two-phase fluid displacement problems including capillary effects, *SPE Reservoir Engineering,* **3**, pp. 691-700.

CRC Handbook of Chemistry and Physics, 1976-1977, CRC Press, 57th Edition, Cleveland, OH.

Fulcher R. A.,Jr., Ertekin, T., Stahl, C. D., 1985. Effect of capillary number and its constituents on two-phase relative permeability curves, Journal of Petroleum Technology. February, pp. 249-260.

Gladkikh M., Jain V., Bryant S., Sharma M.M., "Experimental and theoretical basis for a wettability-interfacial area-relative permeability relationship", SPE (84544) Annual Technical Conference and Exhibition, Denver, CO, USA, 5-8th October 2003

Goodman, T.R, 1964, Application of Integral Methods to Transient Nonlinear Heat Transfer, *Advances in Heat Transfer*, **1**, pp.51-122.

Handy, L.L., 1960, Determination of Effective Capillary Pressures for Porous Media from Imbibition Data, *Petroleum Transactions of AIME*, (T.P. 8109), **219**, pp.75-80.

Jain V., Bryant S., Sharma M.M., "Influence of wettability and saturation on liquid-liquid interfacial areas", Environ. Sci. Technol. 2003, 37, 584-591

Kashchiev, D. and Firoozabadi, A., 2003, Analytical solutions for 1D countercurrent imbibition in water-wet media, *SPEJ*, **8**, pp.401-408.

Kim H., Rao S.C., Annable M.D., "Determination of effective air-water interfacial area in partially saturated porous media using surfactant adsorption", Water Resources Research, 33 , 2705-2711, Dec 1997

Kyte, J.R., Rapoport, L.A., 1958. Linear behavior and end effects in water-wet porous media. Petroleum Trans. AIME, v.213, pp.423-426.

Leverett, MC: Flow of oil-water mixtures through unconsolidated sands. *Trans. AIME,* 1939, 132:151-169.

Li,Y., Morrow,N.R., Ruth,D.W.,2003. Similarlity solution for linear counter-current spontaneous imbibition, Journal of Petroleum Science and Engineering, 39, pp. 309-326.

Li, Y., Ruth, D., Mason, G., and Morrow, N.R., "Pressures acting in counter-current spontaneous imbibition", Proceedings of the 8th International Symposium on Reservoir Wettability, Houston, TX, May 17-18, 2004.

Ma, S., Zhang, X., Morrow, N.R., 1999. Influence of fluid viscosity on mass transfer between rock matrix and fractures. Journal of Canadian Petroleum Technology, v.38, no.7, pp.25-30.

Ma, S., Morrow, N.R., Zhang, X., 1997. Generalized scaling of spontaneous imbibition data for strongly water-wet systems. Journal of Petroleum Science and Engineering, v.18, pp.165-178.

Mattax, C.C., Kyte, J.R., 1962. Imbibition oil recovery from fractured, water-drive reservoir. SPEJ, June, pp.177-184.

McWhorter, D.B. and Sunada, D.K., 1990, Exact solutions for two-phase flow, *Water Resources Research*, **26**, pp.399-413.

Monick, John A., 1968. Alcohols: their chemistry, properties and manufacture. Reinhold Book Corp., New York.

Morrow, N.R., "Physics and thermodynamics of capillary action in porous media", I&EC 1970

Morrow, N.R., and Mason, G., 2001, Recovery of oil by spontaneous imbibition, *Curr. Opin. Colloid and Interface Sci*., **6**, pp.321-337.

Rapoport, L.A., 1955. Scaling laws for use in design and operation of water-oil flow models. Trans. AIME, v.204, pp.143-150.

Rapoport, L.A., Leas, W.J., 1953. Properties of linear waterfloods. Trans. AIME, v.198, pp139-148.

Richtmyer,R.D., Morton,K.W., 1973. Difference Methods for Initial-Value Problem, 2nd edn., Interscience, Publishers, New York.

Root, L., Berne, B.J., 1997. Effect of pressure on hydrogen bonding in glycerol: a molecular dynamics investigation. J. Chem. Phys 107 (11), pp. 4350-4357.

Ruth, D.W., Mason, G., and Morrow, N.R., 2003, A numerical study of the influence of sample shape on spontaneous imbibition, *Proc. Int. Sym. of SCA*, Pau, France, Paper 2003-55.

Ruth, D.W, Mason, G., Morrow, N. and Li, Y., 2004, The effect of fluid viscosities on counter-current spontaneous imbibition, *Proc. Int. Sym. of SCA*, Abu Dhabai, UAE, Paper 2004-56.

Ruth, D., Morrow, N.R., Li, Y., Buckley, J.S., 2000. A simulation study of spontaneous imbibition, Proceedings of the International Society of Core Analysts Annual Meeting, Abu Dhabi, UAE, Oct.

Silin, D. and Patzek, T., 2004, On Barenblatt's Model of Spontaneous Imbibition, *Transport in Porous Media*, **54**, pp.297-322.

Tong, Z., Xie, X., Morrow, N.R., 2002. Scaling of viscosity ratio for oil recovery by imbibition from mixed-wet rocks. Petrophysics, 43, 4, pp. 332-340.

van de Ven, T. G. M., 1989. Colloidal Hydrodynamics, Academic Press, San Diego, 1989

Wade, L. G., 1987. Organic Chemistry; Englewood Cliffs, N.J., Prentice-Hall.

Wang, R., 1999. Gas recovery from porous media by spontaneous imbibition of liquid, MS Thesis, University of Wyoming.

Wardlaw, N.C., Li, Y., 1988. Fluid topology, pore size and aspect ratio during imbibition, Transport in Porous Media, 3, pp. 17-34.

Wardlaw, N.C., Taylor, R.P., 1976. Mercury capillary pressure curves and the interpretation of pore structure and capillary behavior in reservoir rocks, Bull. Can. PETR. Geol. 24, pp. 225-262.

Xie, X., and Morrow N.R, 2001. Oil recovery by spontaneous imbibition from weakly water-wet rocks. Petrophysics, 42, 4, pp. 313-322

Yortsos, Y. and Fokas, A.S., 1983, An analytical solution for linear waterflood including the effects of capillary pressure, *SPEJ*, **23**, pp.115-124.

Zhang, X., Morrow, N.R., MA, S., 1996. Experimental verification of a modified scaling group for spontaneous imbibition. SPE Reservoir Engineering, Nov., pp.280-285.

Zhou, X., Morrow, N.R., Ma, S., 2000. Interrelationship of wettability, initial water saturation, aging time, and oil recovery by spontaneous imbibition and Waterflooding. SPE Journal, Jun., v.5 (2).